

# Integration of Ground-Penetrating Radar and Gamma-ray Detectors for Non-intrusive Localisation of Buried Radioactive Sources

Ikechukwu Kevin Ukaegbu, BTech, MSc



Submitted for the degree of Doctor of Philosophy at Lancaster

University.

November 2019

In loving memory of my late mother,

Lolo Patience Ukaegbu

# Acknowledgements

Firstly, I would like to acknowledge the providence of God, which was my chief sustenance throughout this PhD programme. I would also like to thank my first academic supervisor, Dr. Kelum Gamage for his confidence in offering me this PhD position. In addition, his technical guidance, insightful comments and prompt feedback were invaluable to the success of this research.

I am grateful to my second academic supervisors, Dr. Michael Aspinall for his guidance and helpful feedback, and Prof. James Taylor for his valuable advice. I am also thankful to my industrial supervisor, Dr. Douglas Offin of the National Nuclear Laboratory for his help and advice. I would also like to thank my departmental PhD reviewers for patiently reviewing my appraisal reports.

I would like to thank all the technical and administrative staff of the Engineering department for their support. I would also like to thank my colleagues, Michal and Anita, and all the members of the Nuclear Research Group in the department.

I sincerely appreciate the constant encouragement from members of both my immediate and extended family.

Finally, I gratefully acknowledge funding from the Engineering and Physical Sci-

ences Research Council (EPSRC) and the Nuclear Decommissioning Authority, UK.

# Abstract

This thesis reports on the integration of ground-penetrating radar (GPR) and gamma-ray detectors to improve the non-intrusive localisation of radioactive wastes buried in porous materials such as soil and concrete.

The research was undertaken in two phases. In the first phase, a new non-intrusive technique for retrieving the depth of a buried radioactive source from two-dimensional raster radiation images was developed. The images were obtained by moving a gamma-ray detector in discrete steps on the surface of the material volume in which the source is buried and measuring the gamma spectrum at each step. The depth of the source was then estimated by fitting the intensity values from the measured spectra to an approximate three-dimensional gamma-ray attenuation model. This procedure was first optimised using Monte Carlo simulations and then validated using experiments. The results showed that this method is able to estimate the depth of a 658 kBq caesium-137 point source buried up to 18 cm in each of sand, soil and gravel.

However, the use of only gamma-ray data to estimate the depth of the sources requires foreknowledge of the density of the embedding material. This is usually

difficult without having recourse to intrusive density estimation methods or historical density values. Therefore, the second phase of the research employed integrated GPR and gamma ray detection to solve this density requirement problem. Firstly, four density models were investigated using a suite of materials and the best model was then used to develop the integration method. Results from numerical simulations showed that the developed integration method can simultaneously retrieve the soil density and the depth and radius of disk-shaped radioactive objects buried up to 20 cm in soil of varying conditions with a relative error of less than 10%. Therefore, the integration method eliminates the need for prior knowledge of the density of the embedding material.

This work represents the first time data from these two systems i.e., GPR and gamma-ray detector, will be integrated for the detection and localisation of radioactive sources. Furthermore, the results from the developed methods confirm that an integrated GPR and gamma-ray detector system is a viable tool for non-intrusive localisation of buried radioactive sources. This will enable improved characterisation of buried radioactive wastes encountered during the decommissioning of nuclear sites and facilities.

# Declaration

I, Ikechukwu Kevin Ukaegbu, hereby certify that this thesis has been written by me and has not been submitted in any previous application for a higher degree. The work presented here was carried out at the University of Lancaster between December 2015 and November 2019.

Date:.....

Signed:.....

I, Dr. Kelum Asanga Akurugoda Gamage, hereby certify that the candidate has fulfilled the conditions of the resolution and regulations appropriate for the degree of Doctor of Philosophy in the University of Lancaster and that the candidate is qualified to submit this thesis in application for that degree.

Date:.....

Signed:.....

# Contents

<b>Acknowledgements</b>	<b>I</b>
<b>Abstract</b>	<b>III</b>
<b>Declaration</b>	<b>V</b>
<b>List of Figures</b>	<b>XVII</b>
<b>List of Tables</b>	<b>XIX</b>
<b>List of Abbreviations</b>	<b>XXI</b>
<b>List of Symbols</b>	<b>XXIV</b>
<b>1 Introduction</b>	<b>1</b>
1.1 Radioactive wastes . . . . .	1
1.2 Sources of buried radioactive wastes . . . . .	2
1.2.1 Radioactive fallout . . . . .	2
1.2.2 Poor disposal methods . . . . .	3
1.2.3 Underground pipelines . . . . .	3

1.2.4	Irradiated building materials . . . . .	4
1.3	Risks and challenges of buried radioactive wastes . . . . .	4
1.3.1	Human exposure to ionising radiation . . . . .	4
1.3.2	Nuclear decommissioning challenges . . . . .	5
1.4	Buried radioactive wastes characterisation methods and limitations . . . . .	6
1.4.1	Gamma logging and core sampling . . . . .	6
1.4.2	Radiation imaging . . . . .	8
1.5	Research objectives and contributions . . . . .	8
1.6	Achievements . . . . .	9
1.6.1	Peer-reviewed journal publications . . . . .	9
1.6.2	Conference publications . . . . .	10
1.7	Chapter outline . . . . .	11
<b>2</b>	<b>Background</b>	<b>14</b>
2.1	Introduction . . . . .	14
2.2	Gamma rays . . . . .	15
2.2.1	Gamma-ray interactions with matter . . . . .	17
2.2.1.1	Gamma ray attenuation in matter . . . . .	19
2.2.2	Detection of gamma rays . . . . .	21
2.2.2.1	Gas-filled detectors . . . . .	22
2.2.2.2	Scintillation detectors . . . . .	23
2.2.2.3	Solid-state detectors . . . . .	24
2.2.3	Gamma-ray spectroscopy . . . . .	25

2.3	Ground-penetrating radar . . . . .	26
2.3.1	GPR Systems . . . . .	28
2.3.2	Electromagnetic theory related to GPR . . . . .	29
2.3.2.1	Propagation of electromagnetic waves . . . . .	30
2.3.2.2	Scattering of electromagnetic waves . . . . .	33
<b>3</b>	<b>Ground-Penetrating Radar as a Contextual Sensor for Multi-Sensor Radiological Characterisation</b>	<b>35</b>
3.1	Abstract . . . . .	35
3.2	Introduction . . . . .	36
3.3	Integration of radiological and contextual sensors . . . . .	39
3.3.1	Passive integration of radiological and contextual sensors . . .	40
3.3.2	Active integration of radiological and contextual sensors . . .	44
3.3.2.1	Low-level fusion of radiological and contextual sensors	46
3.3.2.2	Higher-level fusion of radiological and contextual sensors . . . . .	52
3.4	GPR as a contextual sensor for radiological characterisation of nuclear sites . . . . .	57
3.4.1	Non-destructive investigation of underground pipes . . . . .	59
3.4.2	Non-destructive investigation of concrete structures . . . . .	62
3.5	Combined GPR and radiation imaging for 3D localisation of radioactive contamination in underground pipes . . . . .	64
3.5.1	Methodology . . . . .	64

3.5.1.1 Matched filter synthetic aperture radar imaging . . . 66

3.5.2 Simulation results . . . . . 67

3.6 Conclusion . . . . . 70

3.7 Acknowledgment . . . . . 72

**4 A Novel Method for Remote Depth Estimation of Buried Radioactive Contamination 73**

4.1 Abstract . . . . . 73

4.2 Introduction . . . . . 74

4.3 Materials and methods . . . . . 77

4.3.1 The approximate 3D linear attenuation model . . . . . 77

4.3.2 Monte Carlo modelling and simulation . . . . . 79

4.3.3 Experiment setup . . . . . 82

4.4 Results . . . . . 84

4.4.1 Simulation results for Cs-137 buried in sand . . . . . 84

4.4.1.1 Effects of scan area and grid cell size . . . . . 89

4.4.2 Simulation results for Cs-137 buried in concrete . . . . . 90

4.4.3 Simulation results for Co-60 buried in sand and concrete . . . 91

4.4.4 Experiment results . . . . . 93

4.5 Discussion . . . . . 96

4.6 Conclusion . . . . . 97

4.7 Acknowledgement . . . . . 98

**5 A Model For Remote Depth Estimation of Buried Radioactive Wastes**

<b>Using a CdZnTe Detector</b>	<b>99</b>
5.1 Abstract . . . . .	99
5.2 Introduction . . . . .	100
5.3 Materials and methods . . . . .	102
5.3.1 The approximate three-dimensional linear attenuation model .	102
5.3.2 Experiment . . . . .	103
5.3.3 Spectrum acquisition and pre-processing . . . . .	106
5.3.3.1 Photo-peak fitting . . . . .	110
5.4 Results and discussion . . . . .	111
5.4.1 Results for caesium-137 . . . . .	111
5.4.1.1 Effect of scanning time . . . . .	117
5.4.2 Results for cobalt-60 . . . . .	119
5.5 Conclusion . . . . .	120
5.6 Acknowledgement . . . . .	121
<b>6 Non-intrusive Depth Estimation of Buried Radioactive Wastes Using Ground-Penetrating Radar and a Gamma-Ray Detector</b>	<b>122</b>
6.1 Abstract . . . . .	122
6.2 Introduction . . . . .	123
6.3 Theoretical framework . . . . .	125
6.3.1 Approximate 3D linear attenuation model . . . . .	125
6.3.2 Principles of GPR . . . . .	126
6.3.3 Bulk density estimation using GPR . . . . .	128

- 6.3.3.1 Estimation of the material's permittivity . . . . . 128
- 6.3.3.2 Permittivity mixing formulas . . . . . 129
- 6.4 Materials and methods . . . . . 132
  - 6.4.1 Gamma-ray data acquisition and processing . . . . . 133
  - 6.4.2 GPR data acquisition and processing . . . . . 135
- 6.5 Results . . . . . 138
  - 6.5.1 Bulk density estimation . . . . . 138
  - 6.5.2 Depth estimation of the buried Cs-137 radioisotope . . . . . 139
- 6.6 Discussion . . . . . 142
- 6.7 Conclusion . . . . . 143
- 6.8 Acknowledgement . . . . . 144

**7 Integration of Ground-Penetrating Radar and Gamma-Ray Detectors for Non-intrusive Characterisation of Buried Radioactive Objects 145**

- 7.1 Abstract . . . . . 145
- 7.2 Introduction . . . . . 146
- 7.3 Theoretical framework . . . . . 149
- 7.4 Materials and methods . . . . . 154
  - 7.4.1 Selection and modelling of sensors . . . . . 155
  - 7.4.2 Measurement scenario modelling . . . . . 157
  - 7.4.3 Simulation and data processing . . . . . 159
- 7.5 Results and discussion . . . . . 161

<i>CONTENTS</i>	XII
7.6 Conclusion . . . . .	168
7.7 Acknowledgement . . . . .	169
<b>8 Conclusion</b>	<b>170</b>
8.1 Summary . . . . .	170
8.2 Significance of the research outputs . . . . .	173
8.3 Future Work . . . . .	174
8.3.1 Different source geometries . . . . .	174
8.3.2 Multiple sources within the investigated area . . . . .	175
8.3.3 Estimation of water content . . . . .	175
8.3.4 Design and fabrication of an integrated gamma-ray detector and GPR system . . . . .	176
<b>Appendices</b>	<b>177</b>
<b>Appendix A Bespoke motorised mount</b>	<b>177</b>
<b>Appendix B Data acquisition programme</b>	<b>178</b>
<b>Appendix C Pulse height analysis code</b>	<b>179</b>
<b>Bibliography</b>	<b>185</b>

# List of Figures

1.4.1 An example gamma log . . . . .	7
2.2.1 Compton scattering of an electron by a photon. . . . .	19
2.2.2 Contribution of photoelectric absorption, Compton scattering and pair production to the linear attenuation coefficient of NaI [28] . . . . .	21
2.2.3 Scintillator optically coupled by a light guide to the PMT. . . . .	23
2.2.4 Components and process of gamma-ray spectroscopy. . . . .	26
2.3.1 Operational principles of the GPR technique . . . . .	27
2.3.2 Block diagram showing key components of an impulse GPR system. Adapted from [56] . . . . .	29
2.3.3 Scattering of an EM wave at the interface between two media . . . . .	33
3.3.1 Overlaying of gamma image over visual images . . . . .	40
3.3.2 Projection of gamma images onto LiDAR images . . . . .	43
3.3.3 Fusion of radiation detector and Microsoft Kinect . . . . .	47
3.3.4 Portal-less highway radiation monitoring system . . . . .	49
3.3.5 Motion compensation of images of moving sources . . . . .	50

3.3.6 3D volume fusion of radiation and visual image . . . . .	52
3.3.7 (a) Radiological Multi-sensor Analysis Platform (RadMap) [96]; (b) background radiation distribution classified by location [66]. . . . .	54
3.3.8 Fusion of radiation and electromagnetic induction sensors . . . . .	56
3.4.1 Block diagram of GPR operation showing reflections from different layers and an object underground. Adapted from [56]. . . . .	58
3.4.2 (a) GPR image showing three hyperbolas [111]; (b) formation of diffrac- tion hyperbola; (c) hyperbola curve fitting [112]. . . . .	60
3.4.3 Non-destructive investigation of concrete . . . . .	62
3.5.1 (a) Modelled contaminated environment (dimensions in cm); (b) MC- NPX model with grid of detectors (section x-x); (c) gprMax model (section x-x). . . . .	65
3.5.2 Monostatic linear SAR data collection. . . . .	67
3.5.3 (a) Ground level image of radiation sources; (b) matched filtered GPR image of pipes; (c) 3D localised image of radiation sources. . . . .	69
4.3.1 A point radioactive source buried in a section of a material. . . . .	78
4.3.2 Sketch of the MCNPX simulation model. . . . .	80
4.3.3 (a) Experiment setup; (b) Graduated pipe for adjusting the distance of the source from the front of the sandbox. . . . .	83
4.4.1 Normalised radiation images of Cs-137 buried in sand . . . . .	85
4.4.2 Plots of model for Cs-137 buried in sand . . . . .	88

4.4.3 (a) Real and estimated depths for Cs-137 buried in sand. Index is the position of each depth value in the depth array; (b) Linear fit of real and estimated depth for Cs-137 buried in sand. . . . . 89

4.4.4 (a) Error per depth for different cell sizes for Cs-137 buried in sand; (b) Error per depth for different scan areas for Cs-137 buried in sand. 90

4.4.5 Linear fit of estimated and real depth for Cs-137 buried in concrete . 91

4.4.6 (a) Real and estimated depths for Co-60 buried in sand. Index is the position of each depth value in the depth array; (b) linear fit of real and estimated depth for Co-60 buried in sand. . . . . 92

4.4.7 (a) Error per depth for different cell sizes for Co-60 buried in sand; (b) Error per depth for different scan areas for Co-60 buried in sand . . . 92

4.4.8 Linear fit of estimated and real depth for Co-60 buried in concrete . . 93

4.4.9 Normalised radiation images and corresponding model plot for selected depths from the experiment . . . . . 94

4.4.10(a) Real and estimated depths from experiment. Index is the position of each depth value in the depth array; (b) Linear fit of real and estimated depths from experiments. . . . . 95

5.3.1 Estimated depth from the simulation of the Cs-137 point source buried in sand . . . . . 103

5.3.2 Setup for the experiment. . . . . 104

5.3.3 Pulse height spectrum analysis algorithm . . . . . 107

5.3.4 Cs-137 spectrum from the Pulse Height Analysis (PHA) algorithm after 50,000 counts. . . . .	109
5.3.5 Cs-137 662-keV photopeak fitting using Equation 5.3.4. . . . .	111
5.4.1 Normalised radiation images of Cs-137 buried in sand for selected depths.	112
5.4.2 Graphs of the model for Cs-137 buried in sand for selected depths . .	114
5.4.3 Real and estimated depths for Cs-137 buried in sand . . . . .	116
5.4.4 Estimated depths for three different scanning times . . . . .	118
5.4.5 Real and estimated depths for Co-60 buried in sand . . . . .	120
6.3.1 Radioactive point source $S$ buried in a material volume. . . . .	126
6.3.2 Principles of GPR . . . . .	127
6.4.1 Setup for the gamma ray measurements. . . . .	134
6.4.2 Setup for the GPR reflected pulse measurements. The antenna was placed 15 cm from the surface of the box. . . . .	135
6.4.3 Measured reflected pulses from the air-soil and air-metal interfaces . .	137
6.5.1 Error in the estimated bulk densities of the three materials under in- vestigation. . . . .	139
6.5.2 Normalised raster images of the Cs-137 source buried at a depth of 14 cm for each of the material (top row). Corresponding fit of the attenuation model for each of the depth images (bottom row). . . . .	140
6.5.3 Estimated depths of the buried Cs-137 source for the three materials.	141
7.3.1 Geometry and parameters for estimating the flux (measured by the detector) due to the point source $S_p$ in the soil. . . . .	150

7.3.2 Operation of a GPR system . . . . .	151
7.3.3 Two ways of arranging two detectors to measure the flux from the disk source. . . . .	154
7.4.1 MCNP5 model of the gamma-ray detector . . . . .	156
7.4.2 gprMax model of the 1.5-GHz antenna from GSSI Inc. . . . .	157
7.4.3 Model of the measurement scenario. . . . .	159
7.4.4 GPR signal for metal disk of a radius of 3 cm buried at 24 cm in dry soil	161
7.5.1 Flux ratio (i.e. $F_2/F_1$ ) for sources of radii of 3 cm, 9 cm and 15 cm buried at various depths in dry soil . . . . .	162
A.0.1 CAD of bespoke motorised mount used in data acquisition . . . . .	177
B.0.1 GUI of the custom MATLAB data acquisition programme . . . . .	178

# List of Tables

4.3.1 Densities and elemental composition of the three materials used in the simulation. The information was obtained from [125]. . . . .	81
4.5.1 Average mass attenuation coefficients for different materials at the photo-peak region of Cs-137 and Co-60 calculated from [127]. . . . .	97
5.3.1 Elemental composition from SEM analysis of the sand used in the experiment. . . . .	105
5.4.1 Parameters for the linear fit between the real and estimated depth from experiments and simulation. . . . .	119
6.4.1 Properties of the materials used in the study. . . . .	133
6.4.2 Estimated bulk permittivity for the three materials using Equation (6.3.4). . . . .	137
6.5.1 Linear polynomials fitted to the scatter graph of Figure 6.5.3 . . . . .	142
7.5.1 Simultaneously-estimated depths and soil densities for disk sources of different radii . . . . .	164

7.5.2 Depth and density estimates for a disk source of radius 3 cm buried at  
a depth of 20 cm in three different soil conditions . . . . . 166

7.5.3 Estimated depths, densities and radii values for disk sources of varying  
radii buried in the dry soil . . . . . 168

# List of Abbreviations

<b>ADC</b>	Analogue to Digital Converter
<b>CRIM</b>	Complex Refractive Index Model
<b>CZT</b>	cadmium zinc telluride
<b>DU</b>	Depleted Uranium
<b>EM</b>	Electromagnetic
<b>EMI</b>	Electromagnetic Induction
<b>GPR</b>	Ground-Penetrating Radar
<b>GM</b>	Geiger Muller
<b>HPGe</b>	High Purity Germanium
<b>LiDAR</b>	Light Detection and Ranging
<b>LNA</b>	Low Noise Amplifier
<b>MAF</b>	Moving Average Filter
<b>MCA</b>	Multichannel Analyser
<b>MCNPX</b>	Monte Carlo N-Particle version X
<b>MCNP5</b>	Monte Carlo N-Particle version 5
<b>MSDF</b>	Multi-Sensor Data Fusion

<b>MV</b>	Mean Vote
<b>MWD</b>	Moving Window Deconvolution
<b>PCA</b>	Principal Component Analysis
<b>PHA</b>	Pulse Height Analysis
<b>PMT</b>	Photomultiplier Tube
<b>PSR</b>	Point Spread Response
<b>ROC</b>	Receiver Operator Characteristics
<b>SAR</b>	Synthetic Aperture Radar
<b>SEM</b>	Scanning Electron Microscopy
<b>WMV</b>	Weighted Mean Vote

# List of Symbols

$\gamma$	Gamma ray.
$\beta$	Beta ray.
$\mathcal{E}$	Gamma-ray energy (eV)
$\theta$	Angle (rad)
$c$	Speed of light ( $\text{m s}^{-1}$ )
$v$	Velocity ( $\text{m s}^{-1}$ )
$I$	Gamma-ray intensity ( $\text{count s}^{-1}$ )
$\mu$	Linear attenuation coefficient ( $\text{cm}^{-1}$ )
$\mu_m$	Mass attenuation coefficient ( $\text{cm}^2 \text{g}^{-1}$ )
$\rho_a$	Density of air ( $\text{g cm}^{-3}$ )
$\rho_b$	Bulk density ( $\text{g cm}^{-3}$ )
$\rho_s$	Specific density of solid particles ( $\text{g cm}^{-3}$ )
$E$	Electric field ( $\text{V m}^{-1}$ )
$H$	Magnetic field ( $\text{V m}^{-1}$ )
$\omega$	Angular frequency ( $\text{rad s}^{-1}$ )
$\varrho$	Permeability ( $\text{H m}^{-1}$ )

$\rho_r$	Relative permeability
$\epsilon$	Permittivity (F m <sup>-1</sup> )
$\epsilon_r$	Relative permittivity
$\epsilon_b$	Relative bulk permittivity
$\epsilon_a$	Relative permittivity of air
$\epsilon_s$	Relative permittivity of solid
$\epsilon_w$	Relative permittivity of water
$\sigma$	Conductivity (S m <sup>-1</sup> )
$\sigma_b$	Bulk conductivity (S m <sup>-1</sup> )
$t$	Time (s)
$k$	Wave number (rad m <sup>-1</sup> )
$\mathbf{a}$	Attenuation constant (N m <sup>-1</sup> )
$\mathbf{b}$	Phase constant (rad m <sup>-1</sup> )
$\varsigma$	Standard deviation
$A$	Amplitude
$\eta$	Impedance ( $\Omega$ )
$W_c$	Water content (%)
$\phi$	Porosity
$r$	Radius (cm)
$\varphi$	Polar angle (rad)
$F_p$	Flux due to a point source (particles)
$F_a$	Flux due to a disk source (particles)

$S_p$	Point-source activity (Bq)
$S_a$	Disk-source activity (Bq cm <sup>2</sup> )
$A_r$	Detector angular response
$C_e$	Detector centreline efficiency(cps cm <sup>2</sup> Bq <sup>-1</sup> )
$f$	Frequency (Hz)
$\tau_w$	Water relaxation time (s)
$T$	Temperature (°C)
$Z$	Atomic number
$A$	Atomic weight
$\lambda$	Decay constant
$T_{1/2}$	Half-life (s)

# Chapter 1

## Introduction

### 1.1 Radioactive wastes

The period following the Second World War was characterised by a dramatic increase in nuclear activities both for military and civil applications. In the UK, the first Magnox reactor for the generation of electricity and production of weapon-grade plutonium was opened in 1956 [1]. This was rapidly followed by 25 additional Magnox reactors by 1971, 14 advanced gas-cooled reactors by 1989, 1 pressurised water reactor in 1995 and several supporting nuclear facilities [1]. This high volume of nuclear activities, in addition to lack of well-developed standards, resulted in the generation of large volumes of radioactive wastes.

Radioactive wastes generated from nuclear activities can generally be classified into low-level wastes, intermediate-level wastes and high-level wastes depending on the half-life of the radioisotopes, the activity concentration and the amount of heat generated. In addition, the waste category determines its level of hazard and corre-

sponding regulatory requirements. For example, high-level wastes have the highest risks and consequently the most stringent regulatory requirements.

## 1.2 Sources of buried radioactive wastes

A significant amount of radioactive wastes generated from human activities can inadvertently become buried in the shallow subsurface and other porous materials. The following subsections discuss examples and pathways through which this can occur.

### 1.2.1 Radioactive fallout

Nuclear accidents and weapons testing in the last 74 years have been one of the major sources of radioactive land contamination. One of the earliest of these accidents is the Windscale fire in 1957, which resulted in the release of about 3.4 PBq of radioactivity across England, Wales and parts of Northern Europe [2]. The Chernobyl accident in 1986 remains the worst nuclear accident with the release of an estimated 5,300 PBq of radioactivity into the environment, which is greater than the 340-800 PBq released during the Fukushima accident in 2011 [3]. In addition, about  $2.38 \times 10^6$  PBq of radioactivity were released into the environment as a result of atmospheric weapons testing mostly between 1945 to 1985 [4]. The main radionuclides in these emissions include isotopes of iodine, caesium, strontium, plutonium and uranium. These were released as particulates that were deposited in significant concentration around areas closer to the incident. These particulates eventually permeated into the soil and became buried due to rainfall and erosion.

### 1.2.2 Poor disposal methods

Irradiated fuel fragments buried at depths of mostly less than 50 cm were discovered at the beaches of Dounreay in Northwest Scotland [5, 6]. These were wastes discharged into the ocean from the nearby Dounreay nuclear site, and washed ashore by tides and waves. These grain-sized fragments were generated during milling to remove the aluminium fuel claddings and they contain mainly caesium-137 radioisotope. Furthermore, the fragments were found randomly scattered over an area of about 200,000 m<sup>2</sup> and have activities ranging from 10<sup>3</sup> to 10<sup>8</sup> Bq. Another example of poor radioactive waste disposal in the soil is the reported case of 32 cobalt-60 sources found buried within 32 cm of the ground surface in a Cambodian hospital [7]. These orphan sources are thought to have been supplied by the Soviet Union during the communist era and were used for cancer treatments [7].

### 1.2.3 Underground pipelines

Extensive networks of underground pipelines are used to transport liquid radioactive wastes such as sludge, liquor etc. in nuclear facilities. The main contamination from these pipelines are due to leakage of the liquid waste from the buried pipes and subsequent contamination of the surrounding soil. For example, the UK has approximately 760 km of pipelines on nuclear sites some of which are known to have leaked [8]. In addition, long-term accumulation of highly active particles inside the pipe due to scale build up can lead to significant radiation levels above the ground for pipes buried less than 50 cm below the ground surface [9].

### 1.2.4 Irradiated building materials

Another category of buried radioactive waste are waste entrained in porous building materials such as concrete and bricks. Concrete is the major material used in building nuclear structures such as reactor containments, silos, fuel ponds etc. because it provides good shielding and is inexpensive [10, 11]. These concrete structures become contaminated when irradiated either by the neutron flux produced during fission or by high-level liquid wastes from leaks and spills [10]. Furthermore, this contamination can penetrate deep into the concrete over time especially through defects such as cracks [12]. Irradiated building materials can be a significant part of the waste volumes encountered during decommissioning of nuclear plants [13].

## 1.3 Risks and challenges of buried radioactive wastes

### 1.3.1 Human exposure to ionising radiation

The short-term effects of human exposure to ionising radiation include ulceration of the skin and internal organs (in case of ingestion), while long-term effects include cancer, gene mutation and death [5, 6]. Consequently, sources of human exposure to ionising radiation are major public health risks.

Shallow buried radioactive sources can induce high levels of radiation above the ground. For example, one of the cobalt-60 sources found buried at the Cambodian hospital [7] induced radiation levels of up to  $60 \text{ mSv h}^{-1}$  above the ground. This is about 26,000 times higher than the stipulated effective dose limit of 20 mSv per year

[14]. Also, buried radioactive sources in beaches like the Dounreay particles can be inadvertently dug up by beachgoers resulting in direct contact and even ingestion.

Another risk associated with buried radioactive waste is their absorption by plants. For instance, caesium-137 is highly soluble and is easily taken up by plants as a substitute for potassium [15]. This can lead to ingestion of caesium-137 either through direct consumption of these plants or through consumption of products from animals that graze on these plants. In addition, the dissolution of these underground wastes can lead to contamination of underground water.

### 1.3.2 Nuclear decommissioning challenges

Nuclear decommissioning is the systematic shutdown, removal or reduction of radiological hazards to regulatory levels and restoration of a nuclear site to unrestricted use [10]. This is an expensive process that can last for decades. For instance, the ongoing decommissioning of the Sellafield nuclear site is expected to be completed by 2120 at a cost of about £53 billion [16]. One of the first critical tasks in nuclear decommissioning is radiological characterisation. This is the identification of the type, category, quantity and location of all radioactive sources in the nuclear site. Characterisation is critical because the entire decommissioning process is heavily influenced by the nature and quantity of wastes and their regulatory requirements [10].

The characterisation of buried radioactive wastes poses a unique decommissioning challenge mainly because of the difficulty in estimating the burial depth of these wastes. Knowledge of the burial depth is important because it determines the best waste decontamination method. For instance, the decontamination of concrete struc-

tures is usually a choice between removal of the contaminated layer (e.g. scarification) and designation of the entire structure as waste [13]. However, removal of the contaminated layer is expensive and laborious if the contamination is too deep. On the other hand, designation of the entire structure as waste unnecessarily increases the volume and cost of wastes to be disposed if the contamination is shallow.

## **1.4 Buried radioactive wastes characterisation methods and limitations**

The risks and challenges of buried radioactive wastes discussed in the previous section underscores the need for effective characterisation to ensure their prompt and safe disposal. The traditional methods of characterising buried radioactive sources are:

### **1.4.1 Gamma logging and core sampling**

Gamma logging involves lowering sensing probes (consisting of a gamma-ray detector and associated electronics) into boreholes to measure the variation of radioactivity with depth along the borehole. This technique is commonly used in geological exploration to investigate variations in natural radioactivity when searching for mineral deposits such as petroleum and uranium [17, 18]. Gamma logging have also been used in estimating the depth and activity of buried waste during decommissioning and land remediation [7, 19]. Figure 1.4.1 is an example of a gamma log plot of a radioactive source buried at about 32 cm.

Core sampling is related to gamma logging however, instead of lowering the

gamma-ray detector into the borehole, columns of the soil or concrete are extracted and analysed [20]. The analysis could be simply moving a gamma-ray detector along the extracted core or dividing the core into sections for detailed analysis. Core sampling is useful when the detector is to be protected from contamination.

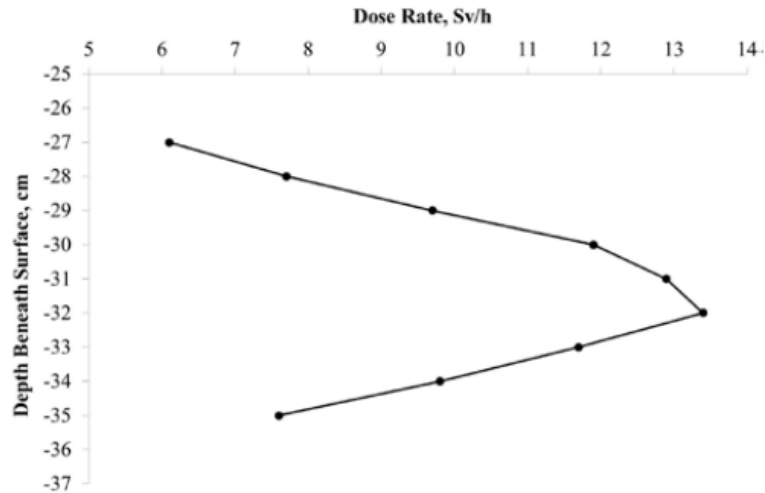


Figure 1.4.1: Gamma log showing variation of dose rate with depth of a buried cobalt-60 source [7]. The maximum dose rate is at 32 cm which indicates the likely depth of the source.

Gamma logging and core sampling usually yield accurate results however, they are intrusive and time consuming. They also have limited sampling extent because subsurface contaminations often span a wide area. In addition, the gamma logging probe can easily become contaminated during operation and become an additional radioactive waste.

### 1.4.2 Radiation imaging

Radiation imaging techniques are also used in the detection and localisation of radioactive sources [21–24]. The radiation cameras used in the localisation of radioactive sources can be broadly divided into two namely: collimated and Compton cameras. Collimated cameras use a collimator to limit the gamma rays reaching the detector to those only in the direction of interest. They include pin-hole cameras that have only a single tiny aperture into the collimator [21], and coded-aperture cameras that have multiple apertures arranged in a pattern [22]. Compton cameras use the Compton scattering principle to reconstruct an image of the source in order to find its location [24].

The images produced by radiation cameras are two-dimensional (2D) spatial distribution of the intensity of a radioactive source on a plane. When overlaid on a visual image of the scene, the radiation images provide a rapid way of localising a buried radioactive source on the surface of the material volume in which it is buried. However, the burial depth remains unavailable thereby limiting the usefulness of these images in three-dimensional (3D) localisation of buried sources.

## 1.5 Research objectives and contributions

To overcome the limitations of the aforementioned methods, this thesis proposes to integrate gamma-ray detectors and ground-penetrating radar (GPR) to improve the non-intrusive localisation of buried radioactive wastes. The key objectives are:

- Develop a method for estimating the depth of buried radioactive sources from radiation images.
- Identify contextual information obtainable from GPR that is relevant to the localisation of buried radioactive sources.
- Identify and develop suitable models for the contextual parameter(s).
- Develop a method to integrate the contextual data from the GPR, and the radiation data from the gamma-ray detectors for non-intrusive depth estimation of buried radioactive sources.

The main research contributions are:

- Development of a new method for non-intrusive depth estimation of buried radioactive sources using 2D raster radiation images.
- Development of a new method for integrating data from GPR and gamma-ray detectors for non-intrusive depth estimation of buried radioactive sources.

## 1.6 Achievements

### 1.6.1 Peer-reviewed journal publications

1. I. K. Ukaegbu, K. A. A. Gamage and M. D. Aspinall. Integration of Ground-Penetrating Radar and Gamma-Ray Detectors for Non-intrusive Characterisation of Buried Radioactive Objects. *Sensors*, 19(12):2743, 2019.

2. I. K. Ukaegbu, K. A. A. Gamage and M. D. Aspinall. Non-intrusive Depth Estimation of Buried Radioactive Wastes Using Ground Penetrating Radar and a Gamma Ray Detector. *Remote Sensing*, 11(2):141, 2019.
3. I. K. Ukaegbu and K. A. A. Gamage. A Model for Remote Depth Estimation of Buried Radioactive Wastes Using CdZnTe Detector. *Sensors*, 18(5):1612, 2018.
4. I. K. Ukaegbu and K. A. A. Gamage. A Novel Method for Remote Depth Estimation of Buried Radioactive Wastes. *Sensors*, 18(2):507, 2018.
5. I. K. Ukaegbu and K. A. A. Gamage. Ground Penetrating Radar as a Contextual Sensor for Multi-Sensor Radiological Characterisation. *Sensors*, 17(4):790, 2017.

### 1.6.2 Conference publications

1. I. K. Ukaegbu, K. A. Gamage, M. Aspinall. Estimating the Depth of Buried Radioactive Sources using Ground Penetrating Radar and a Gamma Ray Detector. *In Proceedings of the 2019 IEEE International Symposium on Antennas and Propagation and USNC-URSI Radio Science Meeting*, Atlanta, US, 7-12 July 2019.
2. I. K. Ukaegbu, K. A. Gamage. Validation Of A Model For non-intrusive Depth Estimation Of Radioactive Wastes. *In Proceedings of the 2018 IEEE Nuclear Science Symposium and Medical Imaging Conference*, Sydney, Australia, 10-17 November 2018.

3. I. K. Ukaegbu, K. A. Gamage. Real-Time Non-Intrusive Depth Estimation Of Buried Radioactive Wastes Based On Approximate Three-Dimensional Relative Attenuation Model. *In Proceedings of the 21st IEEE Real Time Conference*, Virginia, USA, 9-15 June 2018.
4. I. Ukaegbu, K.A.A. Gamage. Radiological Characterisation Using Radiation Imaging And Ground Penetrating Radar. *In Proceedings of the 10th International Topical Meeting on Industrial Radiation and Radioisotope Measurement Applications (IRRMA-X)*, Chicago, USA, 9-13 July 2017.
5. I. K. Ukaegbu and K. A. A. Gamage. Parametric Analysis and Bandwidth Optimisation of Hybrid Linear-exponential Tapered Slot Vivaldi Antennas. *In Proceedings of the IET Loughborough Antenna and Propagation Conference*, Loughborough, UK, 13-14 November 2017.

## 1.7 Chapter outline

- **Chapter 2:** This chapter presents the relevant radioactivity and GPR theories that were used in this thesis.
- **Chapter 3:** This chapter is a critical review of existing literature on the integration of gamma-ray detectors with a wide variety of sensors to improve the characterisation of radioactive sources. It identifies the limitations of these sensors and proposes GPR as a contextual sensor for characterising buried radioactive sources.

- **Chapter 4:** The development of a non-intrusive method for estimating the depth of a buried radioactive source from 2D raster gamma images is presented in this chapter. The method is based on an approximate 3D gamma-ray attenuation model. The results from Monte Carlo simulations and experiment using an organic liquid scintillator gamma-ray detector are presented and discussed.
- **Chapter 5:** Further investigation of the depth estimation method developed in Chapter 4 is presented in this chapter. The experiments were undertaken using a cadmium zinc telluride (CZT) gamma-ray detector which has better energy resolution compared to the organic liquid scintillator detector. The use of the CZT detector increased the maximum detectable depth by 50% using only 14% of the average count rate compared to organic liquid scintillator detector.
- **Chapter 6:** The combination of GPR and gamma-ray detector for the non-intrusive estimation of buried radioactive sources is presented in this chapter. The role of the GPR was to enable non-intrusive estimation of the bulk density required by most depth estimation methods including that developed in Chapters 4 and 5. Four density models were investigated and the results showed that the exponential mixing model with an exponential value of 0.65 gave the best bulk density estimates across a suite of materials.
- **Chapter 7:** This chapter presents the development of a method for integrating GPR and gamma-ray detector for rapid characterisation of buried radioactive objects. The method exploits the density relationship between the flux measured by the gamma-ray detector and the density model identified in Chapter

6 to simultaneously estimate the radius and depth of a disk-shaped radioactive object, and the density of the material in which it is buried. The results from Monte Carlo simulations using experimentally validated detector models are presented and discussed.

- **Chapter 8:** Discussions and summary of the thesis is presented in this chapter in addition to suggestions on further improvements on the methods developed in the thesis.

# Chapter 2

## Background

### 2.1 Introduction

This chapter presents the theories underlining the principles used in this thesis and is broadly divided into two parts. The first part introduces the concept of radioactivity with special focus on gamma rays which is the radiation of interest in this thesis. It also discusses the interaction of gamma rays with matter which is important in understanding the operations of gamma-ray detectors and the behaviour of gamma rays emitted by radioactive sources buried inside materials. The last section in this part introduces gamma-ray spectroscopy which is the process of measuring gamma rays. The second part of this chapter presents the electromagnetic theories pertinent to GPR and derives some of the key GPR equations used in this thesis.

## 2.2 Gamma rays

Gamma rays are high-energy electromagnetic (EM) radiation emitted when the nucleus of an atom transits from a higher to a lower excitation state [25]. This is typically preceded by the emission of alpha or beta rays from the nucleus of the unstable atom in the process known as radioactivity. Alpha rays are positively charged atoms of Helium ( ${}^4_2\text{He}$ ) while beta ( $\beta$ ) rays can either be negatively charged (i.e. electrons) or positively charged (i.e. positrons). For a given radioactive source, the number of unstable nuclei decreases exponentially over time by a characteristic factor known as the decay constant [26], i.e.,

$$N = N_0 e^{-\lambda t} \quad (2.2.1)$$

where  $N$  is the number of nuclei at time  $t$ ,  $N_0$  is the number of nuclei at  $t = 0$  and  $\lambda$  is the decay constant. Furthermore, the time taken for the number of unstable nuclei to reduce by one-half is known as the half-life  $T_{1/2}$  and is related to the decay constant by

$$T_{1/2} = \frac{\ln 2}{\lambda} \quad (2.2.2)$$

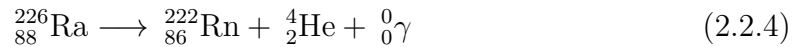
The rate at which a given radioactive sample decays is known as the specific activity or decay rate and is given by [26]

$$D_r = \frac{\lambda A_v}{M} \quad (2.2.3)$$

where  $D_r$  is decay rate (decays  $\text{s}^{-1} \text{g}^{-1}$ ),  $A_v$  is the Avogadro's number and  $M$  is the sample's molecular weight.

Gamma rays were first identified in 1900 by Paul Villard as part of the stream of emissions from radioactive materials earlier observed by Henri Becquerel in 1896 [27]. In his experiments, Paul Villard observed that gamma rays easily penetrate thick black paper and are chargeless, i.e. they do not respond to magnetic fields. In addition to having no charge, gamma rays are also massless and exist as packets of EM energy commonly referred to as photons. This makes them to have significantly higher penetrability compared to alpha and beta particles. For instance, alpha and beta rays are stopped by thin layers of paper and aluminium respectively, while thick blocks of lead are required to stop gamma rays. Consequently, gamma rays are the primary radiation of interest in buried radioactive waste detection and is the focus of this research.

Finally, radioactive elements that emit gamma rays can be naturally occurring, e.g. radium-226, which undergoes alpha decay (Equation (2.2.4)), or artificially synthesised e.g. caesium-137, which undergoes beta decay (Equation (2.2.5)). However, the synthesised radioisotopes constitute most of the gamma-emitting radioactive wastes encountered during nuclear decommissioning.



### 2.2.1 Gamma-ray interactions with matter

The energy of a gamma ray is an important factor in its interaction with matter because it determines the type of interaction the gamma ray undergoes [26]. This energy is measured in electron volts (eV) where  $1 \text{ eV} = 1.60217657 \times 10^{-19} \text{ J}$  is the work done when an electron moves through a potential difference of one volt. Gamma rays undergo three major types of interactions namely: photoelectric absorption, Compton scattering and pair production [26].

#### Photoelectric absorption

In photoelectric absorption, the incident gamma ray transfers all of its energy upon interaction with the orbital electron of an atom and goes into extinction. A small percentage of the gamma-ray energy is used to dislodge the electron from its orbit however, most of the energy is transferred to the dislodged electron as kinetic energy. The probability of photoelectric absorption depends on the energy of the gamma ray, the binding energy of the electron and the atomic number. Tightly-bound electrons, i.e. electrons closer to the nucleus, have a greater probability of causing photoelectric absorption. Consequently, a large percentage of photoelectric absorption interactions involve K-shell electrons [28]. In addition, the dependence of photoelectric absorption on the atomic number  $Z$  is approximately of the order of  $Z^n$  where  $n$  varies between 4 and 5 [26]. Therefore, materials with high atomic numbers are commonly used as gamma-ray shields and detectors. Finally, the almost complete transfer of the gamma energy makes photoelectric absorption an important process in the detection

of gamma ray. This is because the pulses induced by the freed electrons result in a full-energy peak in the generated gamma spectrum.

### Compton Scattering

The main feature of Compton scattering is the partial transfer of the gamma-ray energy upon interaction with the electrons of an atom. This occurs when the gamma ray collides with outer shell electrons that are weakly bonded to the nucleus. Since the binding energy of these electrons are much less than the energy of the gamma ray, only part of the gamma-ray energy is transferred due to the law of conservation of energy and momentum. Consequently, the gamma ray does not cease to exist, rather it is scattered at an angle and continues travelling with decreased energy (Figure 2.2.1). The new energy of the scattered gamma ray,  $\mathcal{E}_s$ , is:

$$\mathcal{E}_s = \frac{\mathcal{E}_i}{1 + \left(\frac{\mathcal{E}_i}{m_0c^2}\right) (1 - \cos \theta)} \quad (2.2.6)$$

where  $\mathcal{E}_i$  is the energy of the incident gamma ray,  $m_0c^2$  is the mass of an electron at rest (0.511 MeV) and  $\theta$  is the scatter angle. The probability of Compton scattering depends mainly on the electron density and only slightly on the atomic number since it involves electrons relatively far away from the nucleus.

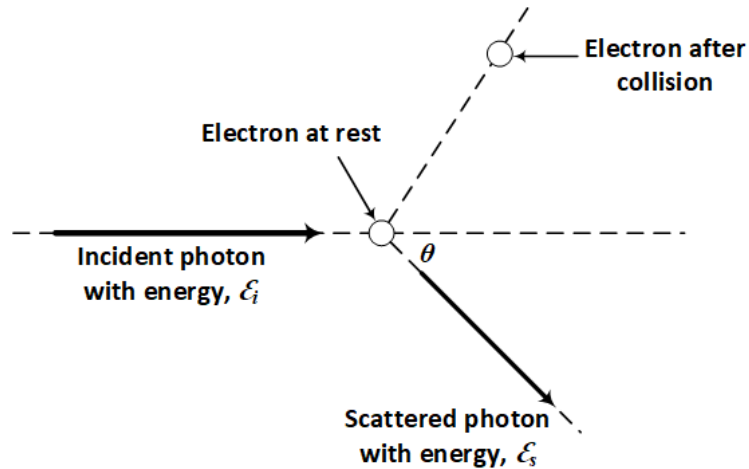


Figure 2.2.1: Compton scattering of an electron by a photon.

### Pair production

Pair production interaction occurs when the energy of the incident gamma ray is greater than 1.022 MeV, i.e. twice the rest-mass energy of an electron. In this interaction, the gamma ray ceases to exist and is replaced by an electron-positron pair. Any excess energy left after the creation of the pair is shared between the electron and positron as kinetic energy. The positron will eventually be slowed down by the material medium and combine with an electron in an annihilation process. The annihilation process mostly produces two gamma rays with energies of 0.511 MeV, which may escape or be absorbed in the material. In addition, the probability of pair production increases with the square of the atomic number (i.e.  $Z^2$ ).

#### 2.2.1.1 Gamma ray attenuation in matter

When gamma rays pass through a bulk of material, some lose part or all of their energy and cease to exist due to the interaction mechanisms already described. The

cumulative effect of these atomic interactions is the attenuation of the gamma rays as they travel through the material. This attenuation was discovered to be exponential by Soddy and Russel in 1909 [29] and is the basis of the gamma-ray attenuation law which states that the intensity  $I$  of gamma rays after passing through a material of thickness  $z$  is:

$$I = I_0 e^{-\mu z} \quad (2.2.7)$$

where  $I_0$  is the intensity of the gamma rays at the point of incidence with the material and  $\mu$  is the linear attenuation coefficient ( $\text{cm}^{-1}$ ). The linear attenuation coefficient is a composition of the attenuation effects of the three atomic interaction mechanisms. This is illustrated in Figure 2.2.2 which shows the relative contribution of each of the interactions to the linear attenuation coefficient. The mass attenuation coefficient  $\mu_m$  (Equation (2.2.8)), is the ratio of the linear attenuation coefficient and the material's bulk density  $\rho_b$  and is constant for all physical states of a material at a given energy [26].

$$\mu_m = \frac{\mu}{\rho_b} \quad (2.2.8)$$

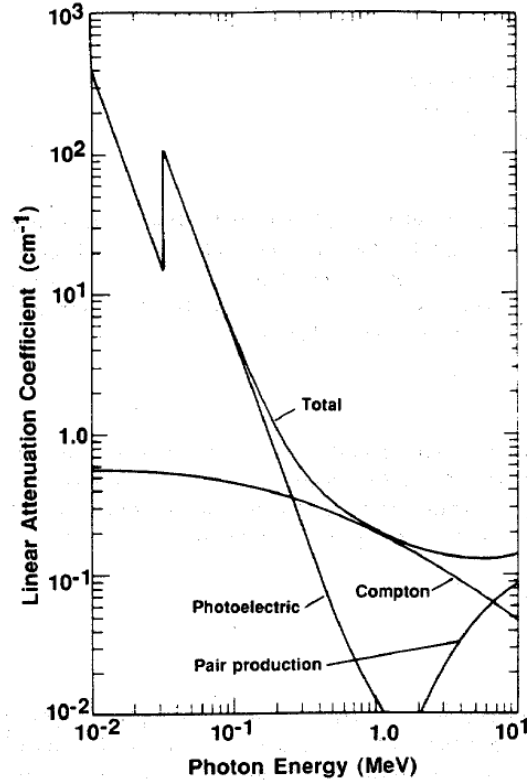


Figure 2.2.2: Contribution of photoelectric absorption, Compton scattering and pair production to the linear attenuation coefficient of NaI [28]

### 2.2.2 Detection of gamma rays

The presence of gamma rays is detected by means of the electrons liberated when they interact with the atoms of matter [26]. The liberated electrons usually go off to free more electrons within the surrounding material volume. This results in the building up of charges which can be collected and converted into an electrical pulse whose amplitude is proportional to the energy deposited by the incident gamma ray. Therefore, a gamma-ray detector typically consists of a material that is sensitive to gamma-ray interactions, and appropriate electronics to convert the resulting freed

charges to voltages.

### 2.2.2.1 Gas-filled detectors

Gas-filled detectors have a sensitive volume of gas between two electrodes which create an electric field that collects the electrons liberated when the gamma rays interact with the gas molecules. There are three types of gas-filled detectors depending on the voltage supplied to the electrodes. These are ionisation chamber, proportional counter and Geiger-Mueller (GM) detector. Ionisation chambers operate at the lowest voltage that ensures that only the primary electrons liberated by the gamma rays are collected. Proportional counters operate at a higher voltage compared to ionisation chambers. This results in secondary ionisation which helps to amplify the output signal [26]. Both ionisation chambers and proportional counters produce outputs that are proportional to the energy deposited by the incident gamma rays. GM detectors operate at the highest voltage level for gas-filled detectors. This high voltage causes ionisation saturation resulting in an output signal that is not proportional to the deposited energy.

Ionisation chambers and proportional counters are mostly used in low-energy gamma ray monitoring and spectroscopy in medicine and physics research [30, 31]. GM detectors are employed as dosimeters in radiation monitors as they lack the energy information required for spectroscopy. Gas-filled detectors are commonly not used in non-destructive gamma-ray assay because scintillation and solid-state detectors provide significantly better performance.

### 2.2.2.2 Scintillation detectors

Scintillation detectors consist of a luminescent material (scintillator) that emits light upon interaction with gamma rays. The scintillator is optically coupled to a light sensitive device called a photomultiplier tube (PMT) as shown in Figure 2.2.3. Light emissions striking the photocathode of the PMT release electrons, which are accelerated across the PMT by a strong electric field. As the electrons are accelerated, they collide with each dynode thereby liberating more electrons. The cumulative effect of this multiple collisions is the amplification of the electron flux that finally arrives at the anode. The output pulse at the anode is proportional to the energy deposited by the gamma ray if light loss is kept at minimum [32].

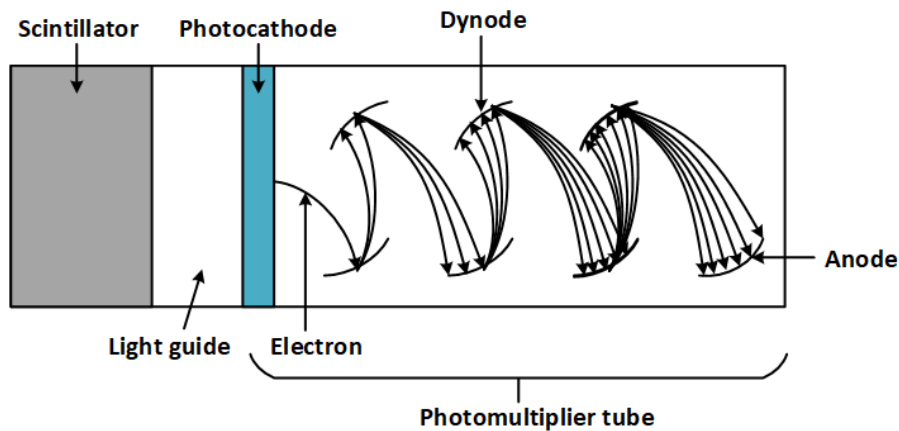


Figure 2.2.3: Scintillator optically coupled by a light guide to the PMT.

The scintillator material can be organic or inorganic. Common inorganic scintillators include thalium doped sodium iodide ( $\text{NaI}(\text{Tl})$ ) and caesium iodide ( $\text{CsI}(\text{Tl})$ ). These are the workhorse of the of the nuclear industry and are widely used in decommissioning, medicine, safety and security, and physics research [33–37] because

they are relatively cheap and have reasonably good spectroscopic qualities. Other common inorganic detectors include bismuth germanate ( $\text{Bi}_4\text{Ge}_3\text{O}_{12}$ ) [38], cerium bromide ( $\text{CeBr}_3$ ) [39], and cerium doped lanthanum bromide ( $\text{LaBr}_3(\text{Ce})$ ) [40]. Organic scintillators are hydrocarbon compounds which can be liquid e.g. EJ309 [41] or solid crystals e.g. Anthracene and Stilbene [42]. Organic liquid scintillators can also be solidified into plastics using polymerising solvents. These plastic scintillators are popular alternatives to the liquid and crystal scintillators because they are inexpensive, and can easily be machined into various shapes and sizes [43]. Organic scintillators have a characteristic fast decay time making them suitable for detecting mixed gamma and neutron fields using pulse shape discrimination techniques [44].

Despite their popularity, scintillation detectors have limited energy resolution. The energy resolution of a detector is defined as the ratio of the full width at half maximum of the photo-peak to the photo-peak energy [45]. The resolution of scintillation detectors is typically between 3 to 10 % [26]. This limited resolution makes them unsuitable for high resolution applications such as the verification of nuclear fuel materials e.g. plutonium-239 and uranium-235.

### 2.2.2.3 Solid-state detectors

The sensitive material in a solid-state detector is a semi-conductor that produces electron-hole pairs when incident by a gamma ray. When a bias voltage is applied, an electric field is created which forces the liberated electrons and holes to migrate to the corresponding electrodes. This flow of charges is converted to a voltage pulse that is proportional to the energy of the incident gamma ray using a charge amplifier.

Solid-state detectors are at the highest end in the grade of gamma-ray detectors because of their superior energy resolution (typically below 1 % [26]). A common example is high-purity germanium (HPGe) which has the high resolution required for verification of nuclear materials such plutonium-239 and uranium-235 [46, 47]. However, one major limitation of HPGe detectors is the need for cooling during operation. Consequently, they are always bundled with bulky cooling systems which decreases their portability. Other solid-state detectors such as cadmium telluride (CdTe) and cadmium zinc telluride (CZT) operate at room temperature but have lower energy resolution compared to HPGe. However, they are suitable alternatives to HPGe when portability is a priority e.g. hand-held gamma cameras [24, 48, 49].

### 2.2.3 Gamma-ray spectroscopy

The rate and energy of the gamma rays emitted by a nucleus are characteristic of the decaying radioisotope. This means that information about the radioisotope can be obtained by measuring and studying the range of energies of the emitted gamma rays. This is referred to as gamma-ray spectroscopy and is an indispensable tool in gamma-ray assay. The key components of a gamma-ray spectroscopy system are shown in Figure 2.2.4. The preamplifier converts the low amplitude current pulse from the detector to a voltage pulse that is proportional to the energy deposited by the gamma ray. This voltage pulse is further amplified and shaped by the amplifier to meet the input requirements of the multichannel analyser (MCA).

The MCA digitises and sorts the voltage pulses into a histogram of amplitudes called the pulse height spectrum [50]. The digitisation is done by an ADC which

accepts the analogue pulse and outputs a binary number that is proportional to the pulse's amplitude. The binary outputs of the ADC are then sorted into appropriate channels by other components of the MCA to generate the spectrum. The MCA can also operate in other modes such as multichannel scaling mode where the number of pulses over a given time is counted in order to generate a histogram of counts [50]. A comprehensive description of the gamma-ray spectroscopy instrumentation and method used in this research is presented in Subsection 5.3.3. In addition, a description of the custom programme developed for data acquisition and a MATLAB implementation of the pulse height spectrum algorithm are given in Appendices B and C respectively.

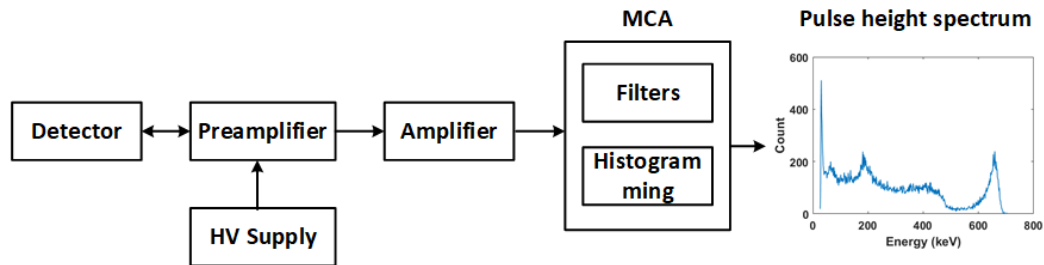


Figure 2.2.4: Components and process of gamma-ray spectroscopy.

## 2.3 Ground-penetrating radar

Ground-penetrating radar is a geophysical technique that employs radio detection and ranging (radar) for non-intrusive subsurface investigation. It uses EM waves to actively interrogate the medium under investigation in order to extract information about its internal properties and objects that may be buried therein. It is widely used in fields such as mining and mineral exploration [51], monitoring of soil properties in

agriculture [52], unexploded ordnance survey [53], non-destructive testing [54] and monitoring of utilities [55].

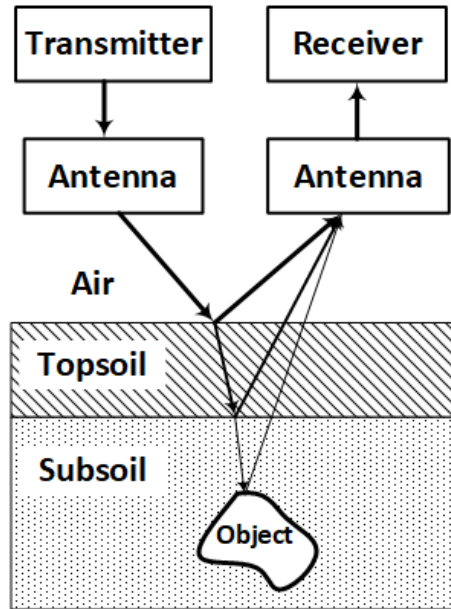


Figure 2.3.1: Operational principles of the GPR technique. The transmitted signals are reflected by any intervening objects and are captured by the receiving antenna. Adapted from [56]

In general, the operation of the GPR involves transmitting an EM signal into the medium under investigation (Figure 2.3.1). As the signals propagate inside the medium, they are reflected when they encounter a boundary, i.e. an object or a different material layer. These reflected signals are then measured by the receiving antenna for processing and analysis. The time between transmission and reception of the signal is related to the distance of the cause of the reflection, while the amplitude of the received signal is also related to the electromagnetic properties of the reflector.

### 2.3.1 GPR Systems

The most common type of GPR system is the impulse GPR, which operates in the time domain using an ultra-wide bandwidth pulse [57]. A high-level block diagram of the key components of a typical impulse GPR system is shown in Figure 2.3.2. The transmitter unit consists mainly of the pulse generator which generates a high amplitude pulse upon initiation by the timing unit. The generated pulse have a very short duration (in the order of micro and nano seconds) and is centred on the operating frequency of the GPR system. Typical centre frequencies for GPR systems range from a few hundred megahertz to about 5 GHz [58]. The generated pulse is fed into the transmitting antenna. The antenna plays the role of a transducer and is a critical component of any GPR system. This is because it determines the characteristics of the pulse that is eventually transmitted. In other words, the output signal from the GPR system is a convolution of the transfer function of the pulse with that of the antenna [57]. Therefore, the choice and design of the antenna should ensure desirable properties such as high gain and narrow beamwidth across the bandwidth of the pulse [59]. Common types of antennas used in GPR systems include bow-tie [60], Vivaldi [61] and horn [62] antennas.

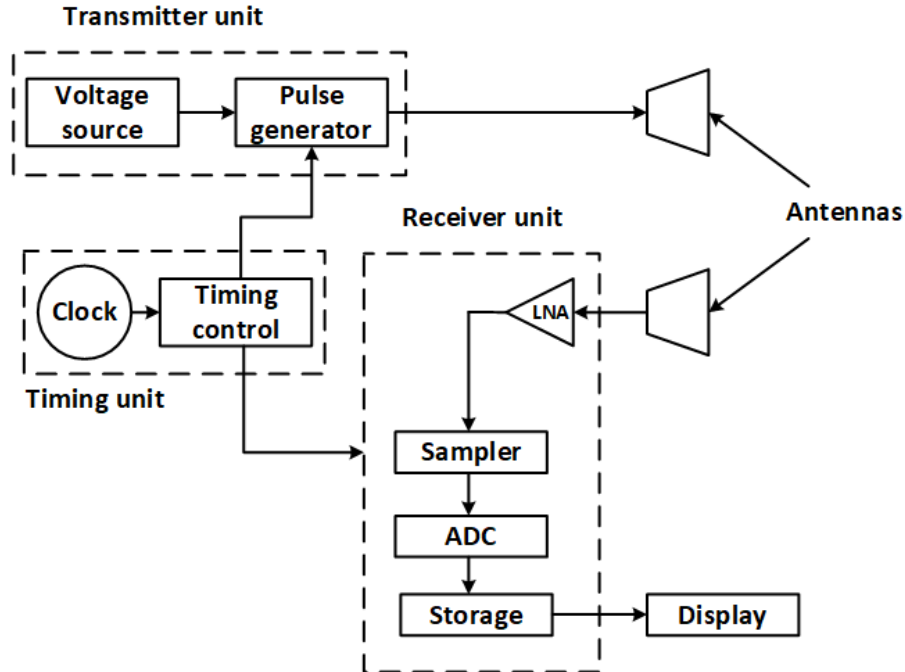


Figure 2.3.2: Block diagram showing key components of an impulse GPR system.

Adapted from [56]

The reflected pulse captured by the receiving antenna is a significantly attenuated version of the transmitted pulse and needs to be amplified in the receiver unit. This is done using a low noise amplifier (LNA) to minimise the amplification of system noise. After amplification, the pulse is sampled and digitised by the analogue to digital converter (ADC) and stored for display and post processing.

### 2.3.2 Electromagnetic theory related to GPR

The application of GPR relies on the interaction between EM waves and the constituent materials of the surrounding medium. The two interaction mechanisms relevant to GPR are EM wave propagation and EM wave scattering.

### 2.3.2.1 Propagation of electromagnetic waves

The properties of an EM wave propagating through a medium depends on the source of the field and the EM properties of the medium [63]. The EM properties of a medium are permittivity, conductivity and permeability. The permittivity is a measure of the resistance offered by a material to the influence of an electric field and has unit of farad per meter ( $\text{F m}^{-1}$ ). The permeability is a magnetic property of a material that indicates its ability to allow the formation of magnetic fields. It is the magnetic equivalent of the permittivity and has unit of henry per meter ( $\text{H m}^{-1}$ ). However, in GPR applications, the influence of permeability is minimal because the materials often investigated are non-magnetic. Consequently, permeability is usually assumed to be equal to that of free space (i.e.  $4\pi \times 10^{-7} \text{ H m}^{-1}$ ). Conductivity is a measure of a material's ability to allow the flow of charges under the influence of electric fields and is measured in siemens per meter ( $\text{S m}^{-1}$ ).

The relationship between these aforementioned EM material properties and the electric field induced by the EM wave is described by the Maxwell's equations and constitutive relations. Furthermore, for a source-free lossy homogeneous medium with permittivity,  $\epsilon$ , conductivity,  $\sigma$ , and permeability  $\rho$ , the Maxwell's equations can be reduced to the Helmholtz equation of a propagating wave [63], i.e.

$$\nabla^2 \vec{E} + \omega^2 \rho \epsilon \left(1 - j \frac{\sigma}{\omega \epsilon}\right) \vec{E} = 0 \quad (2.3.1)$$

where  $\vec{E}$  is the electric field vector and  $\omega$  is the angular frequency (assuming a time dependency of the form  $e^{j\omega t}$ ). Equation (2.3.1) can further be simplified by considering

the  $x$  component of a plane wave that varies only in the  $z$  direction. This yields

$$\frac{\delta^2 E_x}{\delta z^2} + \omega^2 \rho \epsilon \left(1 - j \frac{\sigma}{\omega \epsilon}\right) E_x = 0 \quad (2.3.2)$$

The solution to Equation (2.3.2) is

$$E_x(z) = E_0^+ e^{-kz} + E_0^- e^{kz} \quad (2.3.3)$$

where  $k$  is known as the wave number and is given by

$$k = j\omega \sqrt{\rho \epsilon \left(1 - j \frac{\sigma}{\omega \epsilon}\right)} \quad (2.3.4)$$

The first term in Equation (2.3.3) represents a wave travelling in the  $+z$  direction while the second term represents a wave travelling in the  $-z$  direction. If a complex propagation constant is defined for the medium such that

$$k = j\omega \sqrt{\rho \epsilon \left(1 - j \frac{\sigma}{\omega \epsilon}\right)} = \mathbf{a} + j\mathbf{b} \quad (2.3.5)$$

where  $\mathbf{a}$  is the attenuation constant (nepers per meter) and  $\mathbf{b}$  is the phase constant (radians per meter), then the  $+z$  travelling wave can be rewritten as

$$E_x(z) = E_0(e^{-\mathbf{a}z} e^{-j\mathbf{b}z}) \quad (2.3.6)$$

which has a time domain equivalent of

$$E_x(z, t) = \text{Re}\{E_0(e^{-\mathbf{a}z} e^{-j\mathbf{b}z})e^{j\omega t}\} = E_0 e^{-\mathbf{a}z} \cos(\omega t - \mathbf{b}z) \quad (2.3.7)$$

It can be seen from Equation (2.3.7) that the wave is exponentially attenuated by a factor of  $\mathbf{a}$  as it propagates through the medium. Furthermore, if the phase of the wave is set to a constant and differentiated with respect to time, the velocity  $v$  of propagation will be obtained as

$$v = \frac{\omega}{\mathbf{b}} \quad (2.3.8)$$

Also, the expansion of Equation (2.3.5) will yield the expressions for  $\mathbf{a}$  and  $\mathbf{b}$  as

$$\mathbf{a} = \omega\sqrt{\varrho\epsilon}\sqrt{0.5\left(\sqrt{1+\left(\frac{\sigma}{\omega\epsilon}\right)^2}-1\right)} \quad (2.3.9)$$

and

$$\mathbf{b} = \omega\sqrt{\varrho\epsilon}\sqrt{0.5\left(\sqrt{1+\left(\frac{\sigma}{\omega\epsilon}\right)^2}+1\right)} \quad (2.3.10)$$

The velocity of the EM wave in the investigated medium is important in GPR applications because it enables the estimation of the depth of buried objects. Therefore, an expression of the velocity in terms of the medium's EM properties (i.e. permittivity, conductivity and permeability) is useful. This can be obtained from Equations (2.3.8) and (2.3.10) as

$$v = \frac{1}{\sqrt{\varrho\epsilon}\sqrt{0.5\left(\sqrt{1+\left(\frac{\sigma}{\omega\epsilon}\right)^2}+1\right)}} \quad (2.3.11)$$

Furthermore, for most materials such as soil and concrete, and for frequencies used in GPR applications, the  $\left(\frac{\sigma}{\omega\epsilon}\right)^2$  term in Equation (2.3.11) is much less than 1. Also, both the permittivity and permeability are usually expressed as relative quantities, i.e. as a ratio of their corresponding free space values,  $\epsilon_0$  and  $\varrho_0$  respectively. Therefore, Equation (2.3.11) can be approximated as

$$v = \frac{1}{\sqrt{\varrho\epsilon}} = \frac{c}{\sqrt{\frac{\varrho\epsilon}{\varrho_0\epsilon_0}}} = \frac{c}{\sqrt{\varrho_r\epsilon_r}} \quad (2.3.12)$$

where  $c$  is the free space velocity (299,792,458 m s<sup>-1</sup>),  $\varrho_r$  and  $\epsilon_r$  are the relative permeability and permittivity respectively. Equation (2.3.12) plays a very important role in GPR applications because it enables the velocity of the transmitted GPR signal to be characterised only by the medium's permittivity. This is because the relative

permeability of the materials typically investigated using GPR (e.g. soil, concrete, ice etc.) can be assumed to be equals to 1 since they are non-magnetic.

### 2.3.2.2 Scattering of electromagnetic waves

A propagating EM wave undergoes scattering when it encounters a boundary or interface, i.e. a change in the EM properties of the traversed medium. This scattering phenomenon causes a portion of the wave to be reflected while the remaining portion is transmitted through the interface. The proportion of the reflected and transmitted waves is determined by the reflection and transmission coefficients, which depends on the geometry of the interface and the EM properties of the two media at the interface. For a planar interface between two media e.g. air-ground interface, the scattering of an incident EM wave is illustrated in Figure 2.3.3.

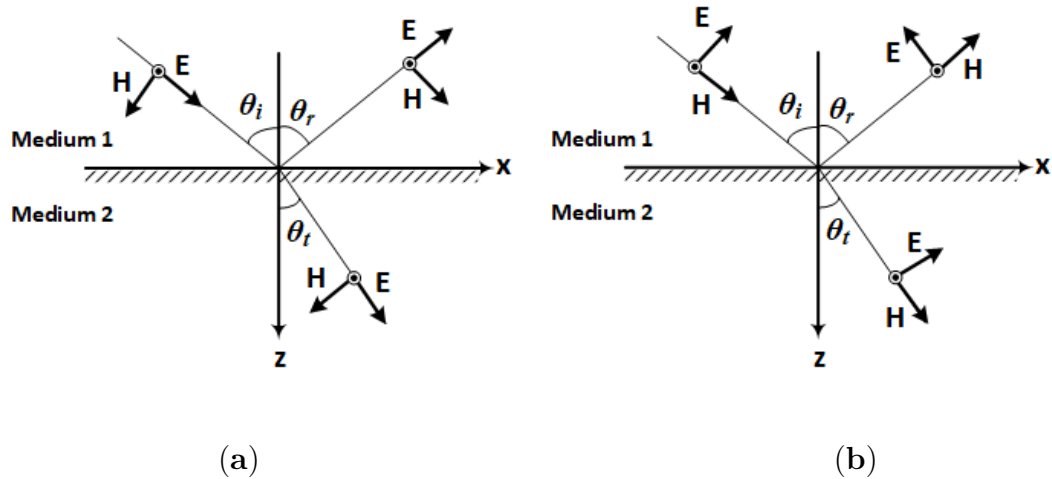


Figure 2.3.3: Scattering of an EM wave at the interface between two media. (a) Transverse electric (TE) scattering (b) Transverse magnetic (TM) scattering

As can be observed in Figure 2.3.3, there are two canonical cases: transverse elec-

tric (TE) and transverse magnetic (TM), depending on which field is in the interface plane. By applying the boundary conditions for the tangential fields at the interface [63], the reflection and transmission coefficients,  $R$  and  $T$  respectively, for the TE and TM cases can be determined as:

$$R_{TE} = \frac{\sqrt{\frac{\epsilon_{r,2}}{\varrho_{r,2}}} \cos \theta_i - \sqrt{\frac{\epsilon_{r,1}}{\varrho_{r,1}}} \cos \theta_t}{\sqrt{\frac{\epsilon_{r,2}}{\varrho_{r,2}}} \cos \theta_i + \sqrt{\frac{\epsilon_{r,1}}{\varrho_{r,1}}} \cos \theta_t} \quad (2.3.13)$$

$$T_{TE} = \frac{2\sqrt{\frac{\epsilon_{r,2}}{\varrho_{r,2}}} \cos \theta_i}{\sqrt{\frac{\epsilon_{r,2}}{\varrho_{r,2}}} \cos \theta_i + \sqrt{\frac{\epsilon_{r,1}}{\varrho_{r,1}}} \cos \theta_t} \quad (2.3.14)$$

$$R_{TM} = \frac{\sqrt{\frac{\epsilon_{r,2}}{\varrho_{r,2}}} \cos \theta_t - \sqrt{\frac{\epsilon_{r,1}}{\varrho_{r,1}}} \cos \theta_i}{\sqrt{\frac{\epsilon_{r,2}}{\varrho_{r,2}}} \cos \theta_t + \sqrt{\frac{\epsilon_{r,1}}{\varrho_{r,1}}} \cos \theta_i} \quad (2.3.15)$$

$$T_{TM} = \frac{2\sqrt{\frac{\epsilon_{r,2}}{\varrho_{r,2}}} \cos \theta_i}{\sqrt{\frac{\epsilon_{r,2}}{\varrho_{r,2}}} \cos \theta_t + \sqrt{\frac{\epsilon_{r,1}}{\varrho_{r,1}}} \cos \theta_i} \quad (2.3.16)$$

where  $\epsilon_{r,1}$ ,  $\epsilon_{r,2}$ ,  $\varrho_{r,1}$  and  $\varrho_{r,2}$  are the relative permittivities and permeabilities of the media, and  $\theta_i$  and  $\theta_t$  are the incident and transmission angles respectively. At normal incidence (i.e.  $\theta_i = \theta_t = 0$ ) and using the fact that  $\varrho_{r,1} = \varrho_{r,2} = 1$ , the transmission and reflection coefficients reduces to

$$R = \frac{\sqrt{\epsilon_{r,2}} - \sqrt{\epsilon_{r,1}}}{\sqrt{\epsilon_{r,2}} + \sqrt{\epsilon_{r,1}}} \quad (2.3.17)$$

$$T = \frac{2\sqrt{\epsilon_{r,2}}}{\sqrt{\epsilon_{r,2}} + \sqrt{\epsilon_{r,1}}} \quad (2.3.18)$$

Equations (2.3.17) and (2.3.18) are important in GPR applications because it enables the estimation of the relative permittivity of a homogeneous media if that of the second media is known e.g. air which has a known relative permittivity of 1.

## Chapter 3

# Ground-Penetrating Radar as a Contextual Sensor for Multi-Sensor Radiological Characterisation

I. K. Ukaegbu and K. A. A. Gamage

*Sensors*, 17(4):790, 2017. DOI: 10.3390/s17040790

### 3.1 Abstract

Radioactive sources exist in environments or contexts that influence how they are detected and localised. For instance, the context of a moving source is different from a stationary source because of the effects of motion. The need to incorporate this contextual information in the radiation detection and localisation process has necessitated the integration of radiological and contextual sensors. The benefits of the success-

ful integration of both types of sensors is well known and widely reported in fields such as medical imaging. However, the integration of both types of sensors have also led to innovative solutions to challenges in characterising radioactive sources in non-medical applications. This paper presents a review of such recent applications. It also identifies that these applications mostly use visual sensors as contextual sensors for characterising radiation sources. However, visual sensors cannot retrieve contextual information about radioactive wastes located in opaque environments encountered at nuclear sites, e.g., underground contamination. Consequently, this paper also examines ground-penetrating radar (GPR) as a contextual sensor for characterising this category of wastes and proposes several ways of integrating data from GPR and radiological sensors. Finally, it demonstrates combined GPR and radiation imaging for three-dimensional localisation of contamination in underground pipes using radiation transport and GPR simulations.

## **3.2 Introduction**

The detection of ionising radiation is critical in fields such as medicine, security and monitoring, and decommissioning of nuclear sites and facilities. While every ionising radiation is associated with some level of hazard, highly penetrating neutron and gamma radiations are of particular interest. This is because their high penetrability makes them to be both harmful and beneficial: harmful because they pose significant dosage risks to both humans and materials even from far off distances, and beneficial because they can be used to detect and image objects located in opaque environ-

ments, such as internal body organs [64], buried mines [65], etc. Furthermore, their high penetrability enables them to be detected from stand-off distances, thereby allowing appropriate safety measures to be implemented. Consequently, a wide range of radiological sensors [21–24] have been developed for stand-off non-destructive detection of both neutron and gamma radiations. These sensors exploit the effects of the interactions (i.e. absorption, scattering and pair production) of these radiations with special materials to detect and image the sources of these radiation, thereby enabling them to be characterised [26].

However, radiation sources exist in an environment referred to as context. This refers to surrounding extrinsic factors that influence the detection, localisation and subsequent retrieval of these sources of radiation. For instance, the context of a stationary source is different from a source in motion because the motion of the source imposes additional challenges to its detection. Similarly, characterising sources located on visible surfaces is different from characterising sources embedded in materials because of the difficulty in obtaining the depth of contamination and the increased influence of background radiation. Furthermore, the relative location of diseased organs, induced with radiation, with respect to other vital organs is critical in proper treatment planning. Other contextual factors include, material and geometry of surrounding objects and weather condition, e.g., rainfall, pressure, etc. [66]. Unfortunately, radiation detectors are unable to measure these extrinsic factors, hence the need for integration with a host of contextual sensors, e.g., visual, ultrasonic, microwave, location, etc. This enables the creation of a holistic view of the environment under investigation, thereby enabling the detection and characterisation of the radioactive

sources of interest.

Furthermore, the benefits of integrating radiological and contextual sensors in medical imaging have been extensively researched and reported [67]. However, integration of both types of sensors have also resulted in interesting and innovative solutions to challenges in characterising radioactive sources in non-medical applications, such as security, non-proliferation and decommissioning of nuclear sites and facilities. However, this latter category of applications is dominated by the integration of radiation and visual sensors. Furthermore, visual sensors are unable to retrieve contextual information about radioactive wastes located in opaque and hard to access environments commonly encountered in nuclear sites and facilities. These wastes include: contaminated underground pipelines used to transport liquid waste; leaked effluents from such pipes and storage ponds; and radioactive contaminant ingress into porous materials, such as concrete [8, 13]. Consequently, there is need to integrate radiation data with contextual data from geophysical sensors such as ground-penetrating radar (GPR).

Therefore, this paper presents a comprehensive review of non-medical applications of the integration of radiological and contextual sensors. Furthermore, it proposes several ways of integrating contextual data from GPR with radiological data in light of the techniques presented in the reviewed works and with particular focus on nuclear decommissioning applications. In addition, it also demonstrates the effectiveness of combined GPR and radiation imaging for three-dimensional (3D) localisation of contamination in underground pipes using radiation transport and GPR simulations. The remaining part of the paper is divided into four sections. Section 3.3 is a review

of the integration of radiological and contextual sensors in non-medical applications with the aim of highlighting the key role played by contextual sensors. Section 3.4 proposes GPR as a contextual sensor for radiological characterisation of hard to access wastes in nuclear sites. Section 3.5 presents modelling and simulation of combined radiation and GPR for 3D localisation of contamination in buried pipes. Finally, concluding discussions and future directions are presented in Section 3.6.

### **3.3 Integration of radiological and contextual sensors**

The reported techniques used in integrating data from radiological and contextual sensors can be broadly classified into passive and active depending on the integration process and the role played by the contextual data in the final output. In passive techniques, the integration process is not based on any mathematical or logical formalism, and the contextual data only serve as a passive backdrop for the radiation data. A classic example is the superimposing of radiation images over visual images of the scene (Figure 3.3.1b,d). On the other hand, active techniques are based on some mathematical or logical model where both the radiation and contextual data actively contribute in determining the final outcome of the integration process. Specific applications of both classes of integration techniques will be described in the following subsections.

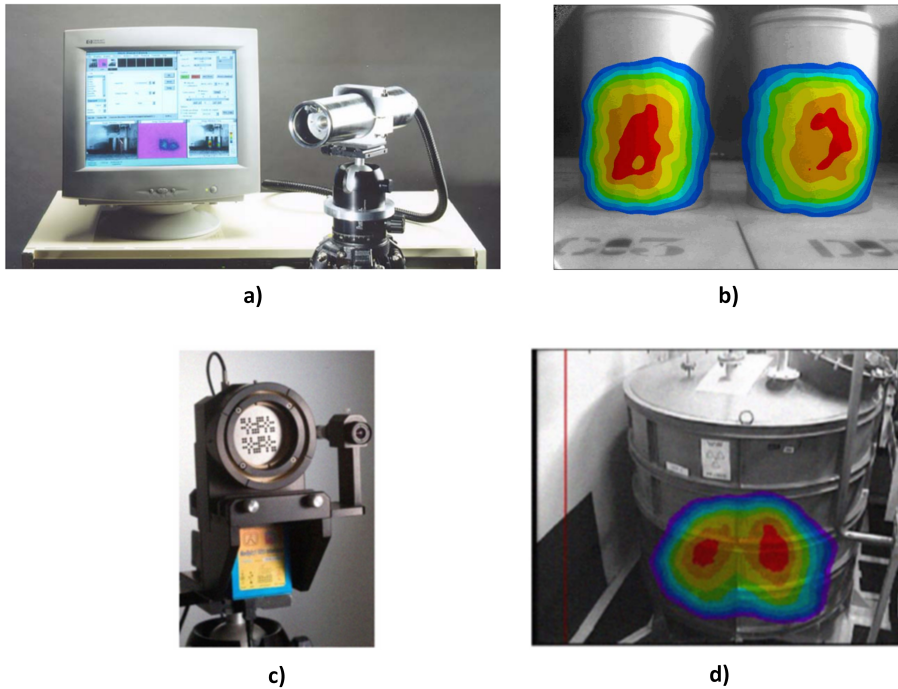


Figure 3.3.1: (a) CARTOGAM imaging system. The detector head beside the PC is mounted on a tripod [68]. (b) Superimposed radiation and visual images from the CARTOGAM [69]. (c) GAMPIX gamma camera (small visual camera attached on the left). (d) Superimposed radiation and visual images from the GAMPIX camera [22].

### 3.3.1 Passive integration of radiological and contextual sensors

Superimposing of the images of the detected sources over a visual image of the environment [21, 22, 24, 68, 69] is perhaps the default scheme for combining radiation and contextual data because of its simplicity. This quickly identifies the object(s) to which the radiation sources are attached. Both images could be obtained by the same

camera since a gamma detector is sensitive to both gamma and visible photons. For instance, the CARTOGAM gamma camera (Figure 3.3.1a) is able to operate in both visible and gamma image mode. During gamma imaging, a thin shutter closes the collimator and prevents the entrance of visible light so that scintillation is only caused by gamma photons penetrating the shutter. To capture visible images, the shutter is opened, and a small lens is remotely placed at the collimator centre. This makes both images be accurately aligned spatially with respect to the imaged scene. However, capturing both gamma and visual images with the same camera increases the overall image acquisition time as both images cannot be captured simultaneously because they require different camera settings [21]. Other cameras, such as [22, 24, 70], employ a separate visual camera co-located with the detector (Figure 3.3.1c). Such configurations are able to take advantage of advances in visual camera technology (e.g., panoramic imaging) and video imaging to give a more realistic and real-time visual rendering of the imaged scene over which the gamma image is subsequently overlaid (Figure 3.3.1d). However, the radiation and visual cameras will have to be physically aligned for accurate superimposing of both images.

Advances in stereo imaging and light or laser detecting and ranging (LiDAR) has enabled the development of systems [71, 72] that can generate 3D visual maps of the environment. These systems have also been used as contextual sensors, in a passive sense, for radiation imaging. In [73, 74], the authors demonstrated the effectiveness of combining a 3D design information verification (DIV) system with a Compton camera for nuclear safeguard applications. The 3D DIV system consisted mainly of a LiDAR system, dolly and associated algorithms that is able to generate high precision 3D

visual maps of rooms and identify any modification or changes in object position [72]. The contaminated environment was simulated by two mock-up pipes (Figure 3.3.2a), one of which contained a line source (i.e. Europium-152). Integration of the images from both systems was accomplished by backprojecting the gamma image from the Compton camera into the 3D visual map. Consequently, objects and regions coincident with the gamma image are identified as contaminated (Figure 3.3.2b). In another similar experiment, the authors in [75] combined a coded aperture gamma camera and a LiDAR system for 3D radiation imaging. However, since the coded aperture camera provides no direction or depth information, a stereo camera was used as a bridge between the two systems. The stereo camera was attached to the gamma camera's mask to align with the optical axis of the gamma camera so that the images from both cameras are automatically aligned. Then 3D points on the stereo image were then aligned to 3D points in the LiDAR image using software algorithms. After the alignment process, the 2D gamma image was then projected into the 3D image of the scene (Figure 3.3.2c).

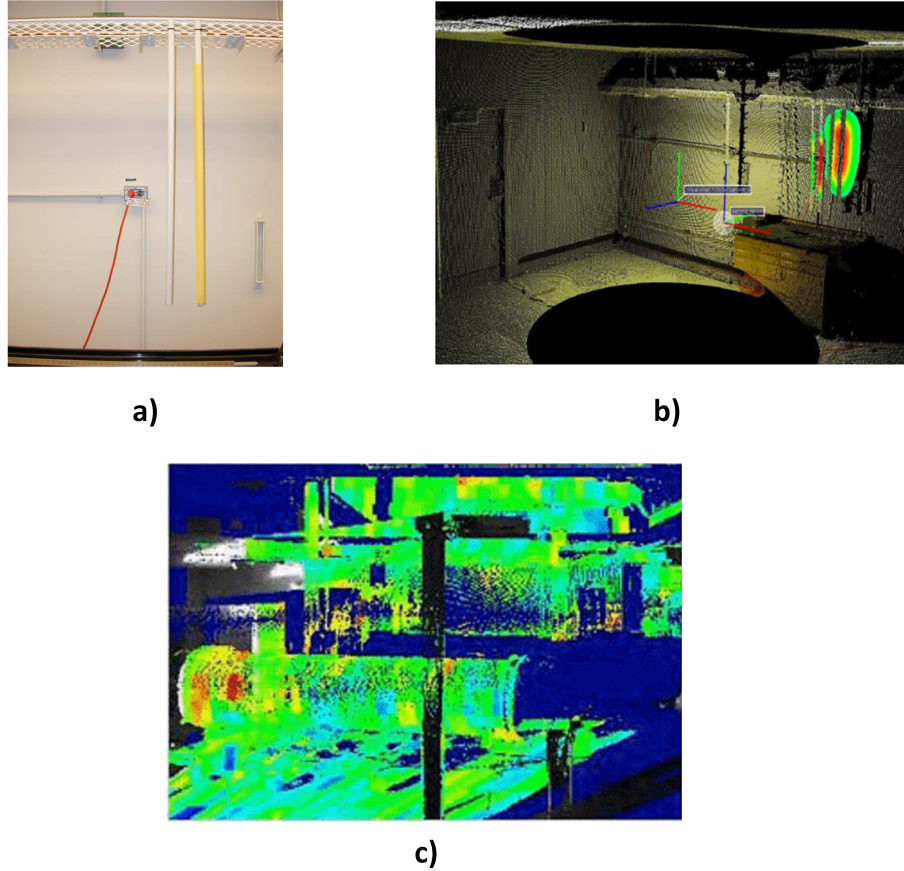


Figure 3.3.2: (a) Zoomed-in picture of the experimental contaminated environment. The contaminated pipe is indicated in yellow colour [73]. (b) Gamma image projected into the 3D LiDAR image of the scene in (a) [73]. (c) Gamma image projected into the 3D LiDAR image of another contaminated environment described in [75].

Passive integration of radiological and contextual sensors described so far is relatively simple to implement and certainly gives a better understanding of the contaminated environment. However, simply overlaying or projecting the radiation image into the images generated by the contextual sensors does not fully account for the underlying dissimilarities between both systems especially in terms of resolution. This results in ambiguities as uncontaminated nearby objects or regions are indicated as

contaminated, as seen in Figure 3.3.2b,c. Furthermore, such ambiguities will require human intervention to be resolved since the process is not quantified, thus preventing the automation of the process, which is very desirable in nuclear environments.

### **3.3.2 Active integration of radiological and contextual sensors**

In order to fully harness the potential of contextual sensors for improved radiation detection/imaging, the data from these sensors need to play an active role in the final result of the combination process and not serve only as a passive backdrop over which the radiation image is overlaid. Such integration can be realised in the context of multi-sensor data fusion (MSDF). MSDF can be described as a well-defined organisation of sensors, data acquisition and processing techniques and decision support algorithms governed by a fusion architecture [76]. This enables the creation of a holistic view of an observation of interest and inferencing of additional information that will otherwise be impossible using only the individual sensors. The participating sensors in the fusion could be similar sensors measuring the same physical phenomenon from the same point in a kind of competitive fashion [77]. In such organisation, the goal of fusion is to increase the reliability and signal to noise ratio with the redundant data. The participating sensors can also be similar sensors measuring the same phenomenon, but from different points or different types of sensors measuring different phenomena from different points [77]. Fusion of radiation and contextual sensors belong to this latter organisation where the complementary data from the multiple sensors are used

to create a holistic understanding of the point of interest.

Furthermore, fusion of data from different sensors can be accomplished at broadly three different levels of data abstraction, namely: low (signal or pixel), medium (feature) and high (decision) levels [78, 79]. Low-level fusion techniques operate on the raw signal or in most cases on the image representations of the raw signals; hence, it is also referred to as signal- or pixel-level fusion. The output of pixel-level fusion is another image, which can be the input to higher fusion levels [79]. Medium- or feature-level fusion techniques operate on characteristic features extracted from the raw data. These features are representative of the observed physical phenomena and can be geometrical, statistical, structural or spectral features [79]. The extracted features are combined into a single feature vector to enable classification usually by automated reasoning algorithms that find correlations among the features [76]. In high- or decision-level fusion, the data from each sensor is fully processed to arrive at an intermediate decision about the phenomenon measured by that sensor. These decisions are then combined using automated reasoning algorithms to arrive at a global decision with a higher confidence [76]. It is important to note that feature and decision fusion levels are closely related, and it is a matter of design choice whether to fuse the extracted features before deriving a decision or to fuse the different decisions derived from the different features [79].

Finally, the fusion of radiological and contextual sensors have been extensively researched and applied in the field of medical imaging where images from positron emission tomography (PET) and single photon emission computer tomography (SPECT) are fused with X-rays, ultrasound, magnetic resonance imaging (MRI), etc., images

for improved diagnosis and localisation of diseased tissues [67]. These applications employ a plethora of techniques and algorithms that cuts across the three levels of MSDF. However, of interest in this paper is the relatively recent fusion of data from radiological and contextual sensors in non-medical applications [66, 80–85]. Furthermore, since the interest is on the key role played by the contextual sensors in radiation detection and imaging, applications with the fusion of multiple datasets from only radiation detectors [86–88] are not included in the following review.

### **3.3.2.1 Low-level fusion of radiological and contextual sensors**

Most fusion techniques operate at this level because of time efficiency and avoidance of loss of information associated with higher fusion levels as a result of extracting only part of the raw data [79]. Consequently, most reported fusions of radiological and contextual sensors are low-level fusions. In addition, these applications are dominated by the fusion of data from radiological and visual sensors, and can be broadly divided into three application areas, namely: (1) detection and tracking of moving sources; (2) motion compensation of images of moving sources; (3) 3D volume fusion of radiation and visual images of the environment.

#### **Detection and tracking of moving sources**

The trajectories of moving radioactive sources in a security scenario are not predefined, e.g., a suspect carrying a radioactive source in a moving crowd. In addition, the trajectories also intersect with those of nearby objects and must be identified in real time with a minimum false alarm rate. A simple and low cost solution to this problem

was proposed and demonstrated in [80]. The authors employed signal-/pixel-level fusion of a commercial depth sensor (Microsoft Kinect) and radiation detectors in order to track moving radiation sources. The method was based on extending traditional camera calibration [89] by attaching a radiation source to a chequerboard pattern and using the pattern to calibrate both sensors. This enabled the estimation of the radial distance of the radiation detector from the source using an integrated model of the detector's count rate and the depth sensor's calibration data. Consequently, the authors were able to track a source hidden amongst multiple moving targets by finding the target whose trajectory most closely matches the trajectory of the source (Figure 3.3.3).

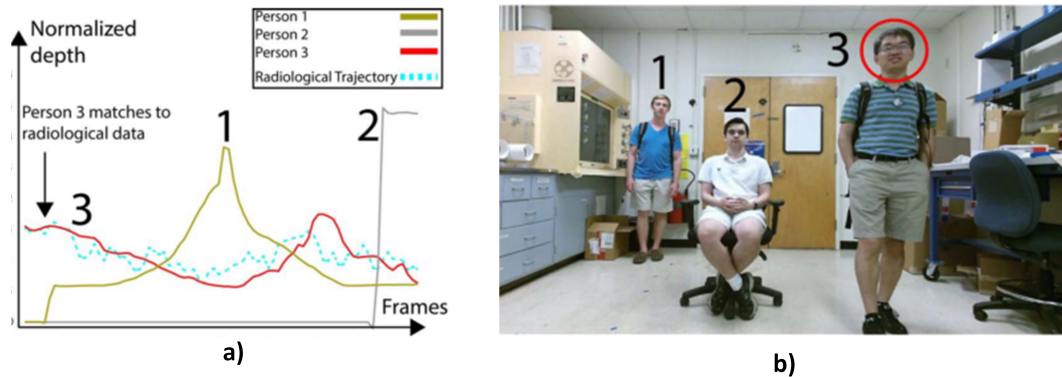


Figure 3.3.3: (a) Normalised depth trajectories of three targets (solid lines) and a radiation source (dotted lines). The trajectory of Target 3 closes matches that of the radiation source therefore he is identified as the suspect; (b) Picture of the three targets with the suspect highlighted [80].

In another, but more elaborate solution, the authors in [82] combined a detector array of gamma imagers [90] with stereo cameras to demonstrate a portal-less highway

radiation monitoring system. The classical radiation portal monitors are associated with several limitations amongst which are: interference with the flow of traffic as vehicles need to slow down at the portals; ease of evasion by smugglers because the portal location is always fixed; and susceptibility to background variation caused by shielding of the detectors as vehicles pass in front of them [82]. Therefore, the portal-less system was designed to overcome these limitations.

The system consisted of two identical sets of equipment fitted on two mobile trailers positioned on either side of the highway (Figure 3.3.4a). Vehicle detection and tracking algorithms [91] were applied to image frames from the video cameras to track the location of the vehicle from frame to frame as it traverses the camera's field of view. These algorithms look for vehicle cues (e.g., regions with high gradients) that are consistent across these frames. After reconciliation of the video data from both trailers, the information was used to generate a sequence of video events that were in turn used to select the subset of gamma events from the gamma cameras that corresponds to the tracked vehicle. These gamma events were then used to generate a high statistic gamma image of the vehicle where radioactive sources are indicated by pixels whose significance is greater than a predefined threshold (Figure 3.3.4b). Results from field trials proved that the system was able to detect unshielded 27-MBq gamma point sources on five-lane highway traffic moving at speeds of up to 113 km/h. Also, adaptation of this same system for autonomous radiation monitoring of small vessels in a maritime environment was also reported in [81].

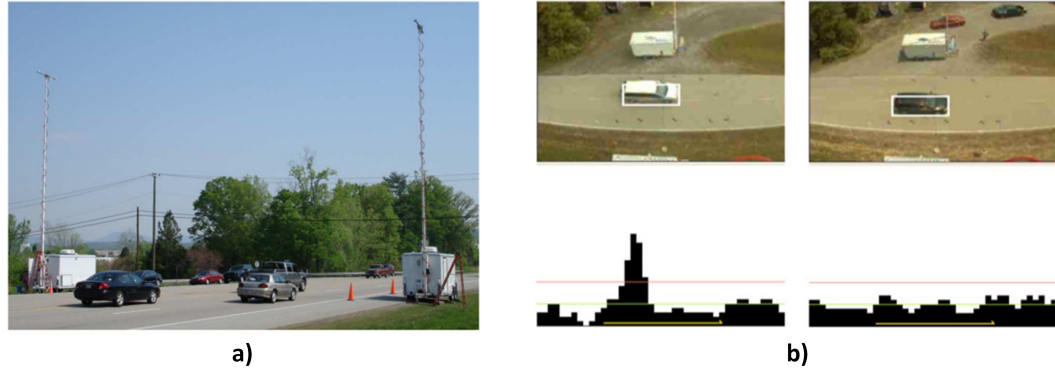


Figure 3.3.4: (a) Two trailers (painted in white) were both equipped with radiation detectors and video cameras and positioned on opposite sides of the road. (b) Output of the fusion algorithm. The top row pictures are frames from the video camera showing the moving vehicle (bounded by the white square). The bottom graphs are the corresponding gamma count per pixel of the generated gamma image. The first vehicle contains a source hence its gamma count is above the threshold (red line) [82].

### Motion compensation of images of moving sources

Another challenge associated with imaging moving radioactive sources is the smearing of the source image across several pixels. This results in a blurred image where the source becomes indistinguishable from background radiation (Figure 3.3.5a). For instance, Compton imaging relies on the fact that Compton cones formed by photons from the same source will overlap coherently, thus forming a point in the image of higher intensity than the background. However, if the source is in motion, the apex of the cones end up in several pixels along the direction of motion; therefore, very few will overlap, resulting in the blurred image. A solution to this problem was demonstrated in [83] by combining video and Compton cameras. In the system, frames from the

video cameras were analysed by a two-stage detection and tracking process in order to estimate the trajectory of the moving vehicle. The estimated trajectory was then used to adjust the position of the Compton cone during reconstruction so that the moving source appears stationary with respect to the detector, thus allowing the cones to overlap in a distinguishable hotspot on the image (Figure 3.3.5a).

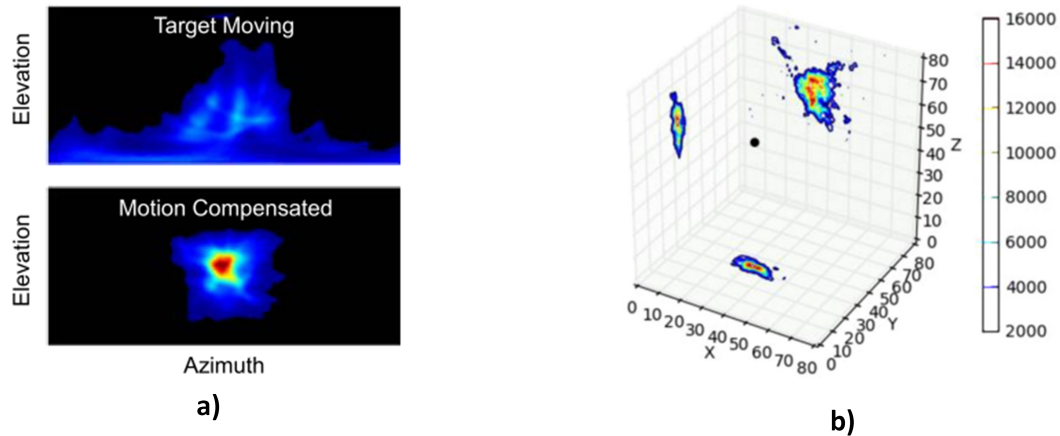


Figure 3.3.5: (a) Reconstructed image of moving source without (top) and with (bottom) motion compensation [83]; (b) 3D tomographic radiation source image on a stationary volume collapsed to the  $x$ - $y$ ,  $y$ - $z$ ,  $x$ - $z$  planes [92].

The use of video camera image data to correct blurring of moving source images was also applied in [92] for ship to ship inspection in order to detect maritime smuggling of nuclear materials. The blurring of the image in this case is a result of wave action, which keeps both the inspection and target vessels in continuous motion. The key components of the system were a stereo video camera and a coded aperture gamma camera. Using both video and disparity images (which give the distance of points in the image from the camera plane) from the stereo camera, the relative location and orientation of both vessels were tracked in 3D across video frames. Using

this information, a stationary reconstruction volume was then defined on a new coordinate system fixed at the target vessel. Voxels from this volume were then projected onto 2D images generated from the gamma camera from different position around the target vessel. Finally, gamma events from pixels in the 2D image closest to the centre of each of the projected voxels were accumulated into gamma events for that voxel resulting in a 3D tomographic radiation image (Figure 3.3.5b).

### **3D volume fusion of the radiation image with the visual image of the environment**

Instead of simply projecting radiation images into already reconstructed 3D visual images of the environment, the data from both systems can be fully integrated during reconstruction to yield a 3D radiation image that is fused with the environment. This was demonstrated in [84] using a Compton camera and a 3D Design Information Verification system consisting mainly of a LiDAR system. First, the 3D data from the LiDAR were used to build a sparse 3D image space model divided into voxels. Then, backprojection weights were calculated for each photon event from the Compton camera image. Finally, a list-mode maximum likelihood algorithm [93] was then used to reconstruct the image by assigning weighted radiation intensity values to each voxel that was intersected by the surface of the Compton cone. This resulted in a spectroscopic 3D gamma-ray image of the scene, as shown in Figure 3.3.6a, which is the image of the same contaminated environment shown in Figure 3.3.2a. It can be clearly observed that the radioactive source is well localised in the pipe compared to the image in Figure 3.3.2b. The poor rendering of the surroundings is due to the use

of a sparse image space in order to reduce computational resources. Figure 3.3.6b is a plot of the intensity of voxels around the pipe from top to bottom, which confirms that the gamma image is fused with the scene. Further application of this technique using other types of radiation cameras and Microsoft Kinect were also presented in [94].

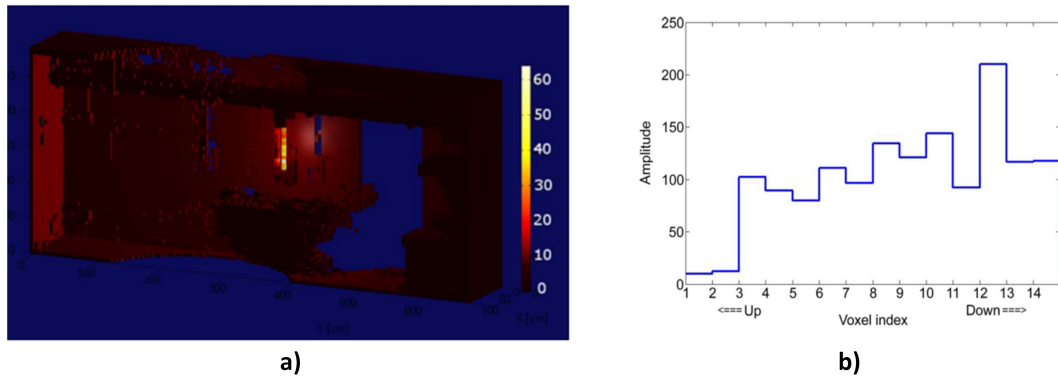


Figure 3.3.6: (a) Reconstructed image of contaminated environment shown in Figure 3.3.2a using the MSDF of the Compton camera and LiDAR images; (b) intensity of voxels from top to bottom around the pipe containing the line source [84].

### 3.3.2.2 Higher-level fusion of radiological and contextual sensors

In general, the decision on the presence or otherwise of radioactive sources of interest in any radiation detection scheme is determined by the value of a threshold. The specific value of this threshold is derived from the measured data, and it defines the boundary above which the influence of naturally-occurring radiation (referred to as background radiation) is minimal. This is to ensure acceptable false alarm rates. However, large variations in background radiation across different environments increases uncertainty in the measurements (e.g., statistical noise), thereby making it

difficult to select a suitable threshold value for a constant false alarm rate across different environments [95]. These variations are due to environmental factors, such as weather conditions, natural and man-made structures, e.g., roads, buildings, soil, etc. Furthermore, this variation cannot be well accounted for by assuming a Poisson background distribution [96]. A more robust solution will involve measuring background radiation in a variety of environments and finding correlations between the probability distribution of each environment with other environmental information, such as location, weather condition, material properties of both natural and man-made surrounding objects, etc. [66]. This implies the fusion of radiation data with data from a wide variety of sensors that measure these contextual factors in order to classify the background distributions from these environments. Furthermore, establishing meaningful relationship between datasets with such a high degree of heterogeneity is only possible at higher levels of data abstraction.

Such an elaborate and exotic fusion described in the previous paragraph has been the objective of a series of researches [66, 94, 96, 97] using the Radiological Multi-sensor Analysis Platform (RadMap). RadMap (Figure 3.3.7a) is a truck-mounted platform fitted with a variety of radiological and contextual sensors for large-scale acquisition of radiological and associated contextual data across different environments [96]. Results from a routine survey of districts in California [66] showed interesting correlations between identifiable features in the contextual data (i.e. places, objects, level of rainfall, etc.) and the background gamma spectra. For instance, Figure 3.3.7b shows the probability distribution of background radiation of four different environments categorised based on GPS locations. In addition, atmospheric pres-

sure was confirmed to be the most dominant factor affecting variability in neutron background radiation [96]. This fusion of different features of the various datasets accurately captures the variability in the background radiation across different environments. Therefore, a detector system can simply adjust its detection threshold to the corresponding environment, thus maintaining a constant false alarm rate. Furthermore, such fused dataset can be used for advanced simulation of the performance of detector systems in real world using the concept of source injection where simulated radioactive sources are injected into real-world models of background radiation [97].

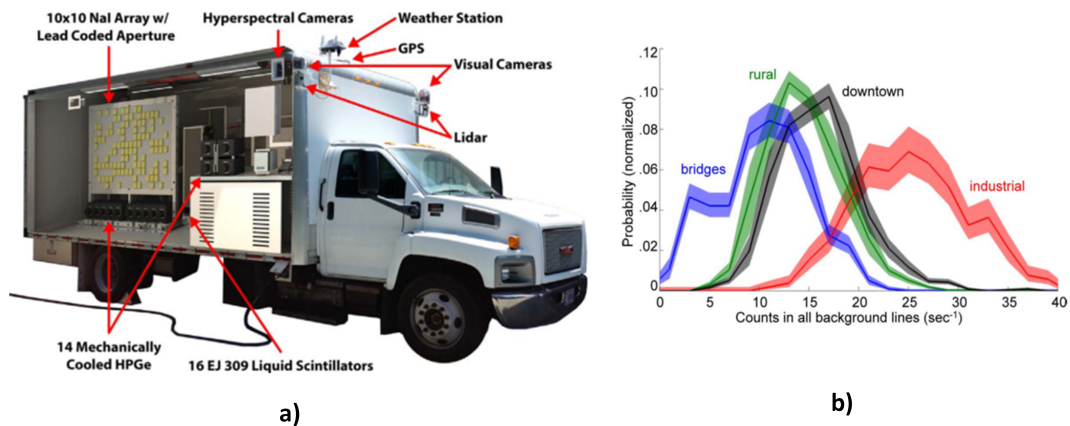


Figure 3.3.7: (a) Radiological Multi-sensor Analysis Platform (RadMap) [96]; (b) background radiation distribution classified by location [66].

Another example of the high level fusion of radiological and contextual sensor was presented in [85] where decision-level fusion was used to integrate radiation and electromagnetic induction (EMI) data in order to detect and distinguish between buried depleted uranium (DU) and its oxide. Distinguishing between DU and DU oxide is important because DU oxides present a higher nuclear hazard; hence, their removal needs to be prioritised [85]. However, radiation detection techniques [98] are

not able to distinguish between these two metals, hence the need for complementary information from the EMI data. First, the radiation data, collected over a gridded survey area, were processed by two anomaly detection algorithms. Each algorithm is able to come to an independent decision (i.e. radiation or non-radiation) about the presence or otherwise of a radiation target by using various background suppression methods. The quadrature components of the H-field measured by the EMI were analysed and compared with a database of known metals to produce three possible decisions, namely: DU metal, non-DU metal and non-metal.

Fusion of the decisions from both sensors followed a two-stage process (Figure 3.3.8a) after re-gridding the survey area so that mismatched survey paths of both systems can fall into the same cell (Figure 3.3.8b). The first stage was to fuse multiple radiation decisions from a single cell into one radiation decision and multiple EMI decisions from the same cell into one EMI decision. This was done using the maximum vote (MV) and weighted maximum vote (WMV) fusion methods [99]. The next stage combined the single decisions from each of the systems using eight fusion rules. These rules were if-then conditions that define the outcome for the desired combinations of both sets of decisions. For instance, two of the rules are: (1) if the EMI decision is “DU” and the radiation decision is “radiation”, then final decision is “DU”; (2) if the EMI decision is “non-DU metal” and the radiation decision is “radiation”, then the final decision is “oxide”. Experimental results confirmed the effectiveness of this fusion framework with over a 90% detection rate.

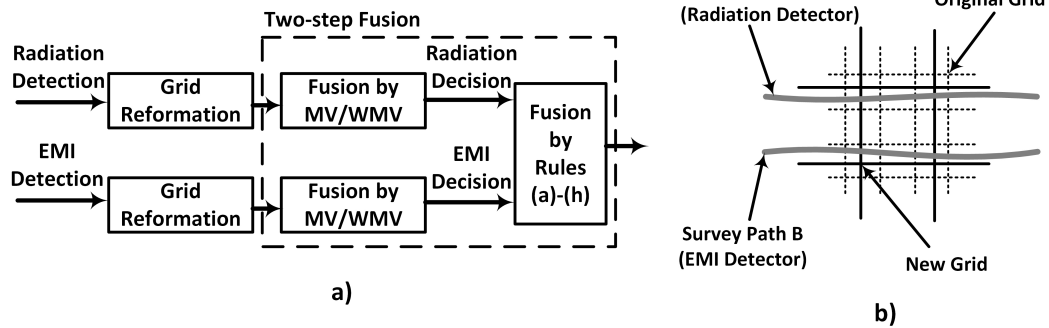


Figure 3.3.8: (a) Decision-level fusion framework for radiation and electromagnetic induction (EMI) data fusion (MV = mean vote, WMV = weighted mean vote); (b) re-gridding of the survey area [85].

MSDF of radiological and contextual sensors at the pixel level yields high quality images with richer information content. However, the most significant advantage of MSDF is the quantification of the fusion process both at lower and higher levels. This enables the definition of metrics, such as root mean square error, entropy, fusion factor, etc. [100], for signal/pixel fusion, and the receiver operator characteristic (ROC) for higher level fusion. These metrics provide an analytical basis for evaluating and optimising the outputs so as to reduce false alarm rates. Furthermore, arriving at a decision on the presence or otherwise of a radiation target in MSDF is inherently an automated process, thereby eliminating human errors. However, accurately calibrating and synchronizing the operations of the participating sensors in the fusion remains a challenging task. In addition, supervised classifiers used in higher level fusion require training with large datasets in order to perform at acceptable levels.

### **3.4 GPR as a contextual sensor for radiological characterisation of nuclear sites**

Radiological characterisation involves the identification of the location, type and other physical properties of radioactive wastes. It is a critical stage in decommissioning potential nuclear contaminated sites and facilities as it provides input to other stages of the decommissioning process [10]. However, some of these wastes are often located in opaque and hard to access areas such as below the ground and inside concrete structures, as noted in Section 3.2. Traditional methods of characterising such wastes, e.g., gamma logging and core sampling, involve excavation, which leads to the generation of secondary wastes and increases the risks of exposure of personnel and equipment to ionising radiation. However, since these wastes are usually liquids or solids (i.e. the radioisotopes are usually attached to liquid or solid matter), contextual information about these liquids and solids (e.g., depth, volume, material type, etc.) inside these opaque areas can be obtained using non-intrusive geophysical methods. This contextual information can then be integrated with data from radiological sensors for enhanced non-intrusive characterisation of these wastes. The fusion of radiation and EMI sensors discussed in Section 3.3.2.2 tries to solve the case of radiation waste buried underground. However, EMI sensors can only detect metals and provide limited and unreliable target depth information [101]. Nevertheless, the successful fusion of both sensors shows the possibility of integrating radiological sensors with more advanced geophysical sensors like GPR.

GPR is a non-destructive geophysical technique for obtaining subsurface snapshots of visually opaque structures, thereby revealing hidden objects or internal property changes in the structure, such as defects and cavities. It is important to note that the term GPR is commonly used to refer to both the technique and the device. Figure 3.4.1 shows the block diagram of a typical GPR unit in a reflection survey. The transmitter generates a series of excitation voltages, which are transformed into a radiating electromagnetic (EM) field by the transmitting antenna. As the signal propagates through the subsurface, it undergoes different types of distortions, such as reflection, attenuation, etc., due to changes in the permittivity and conductivity of the subsurface. These changes are indicative of the presence of objects or discontinuities due to the transition from one material layer to another. The reflected signals are captured by the receiving antenna and processed in order extract useful information about the subsurface.

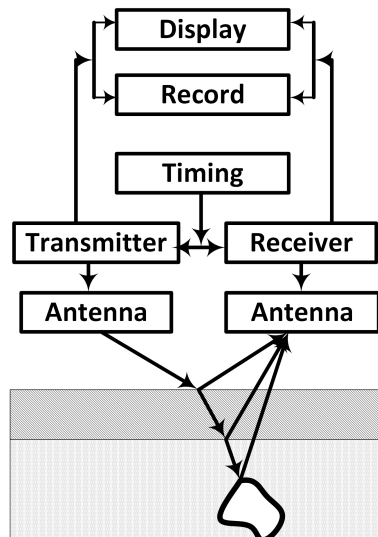


Figure 3.4.1: Block diagram of GPR operation showing reflections from different layers and an object underground. Adapted from [56].

GPR is widely used for non-destructive subsurface investigation across a wide range of application areas [102]. However, of interest are: (1) non-destructive investigation of underground pipes; (2) non-destructive investigation of concrete structures. This is because these application areas are directly relevant to the challenges of characterising wastes in the identified hard to access areas. These application areas will further be discussed in the following subsections with the aim of highlighting where and how GPR and radiation detection/imaging can be integrated for radiological characterisation.

### 3.4.1 Non-destructive investigation of underground pipes

Underground utility pipes and cables form a complex network of pipes, cables and drains in the subsurface [103]. This complexity in addition to their underground location makes their maintenance difficult without prior knowledge of their location. Furthermore, it has been shown that third party damages to utility pipes and cables during excavation is one of the major causes of increasing construction costs [104]. Consequently, GPR is widely used in location, classification and conditional assessment of underground pipelines [55, 105, 106]. Methods for locating buried pipes exploit the characteristic hyperbolas (Figure 3.4.2a) formed by buried objects in GPR radargrams. These hyperbolas are formed by the spreading of the EM waves (beam) as they leave the antenna, thereby illuminating the target before the target is directly under the antenna (Figure 3.4.2b). The equation for this hyperbola can be readily derived from Figure 3.4.2b (Equations (3.4.1) and (3.4.2)). It can be deduced from Equation (3.4.2) that by fitting synthetic hyperbolas to suitable points on a radar-

gram (Figure 3.4.2c), the pipe’s radius, the wave velocity and the pipe’s depth can be estimated [107–109]. In addition, the retrieved wave velocity is an important parameter used in GPR reconstruction algorithms, such as matched filtering, backprojection, migration and tomographic inversion [53, 110]

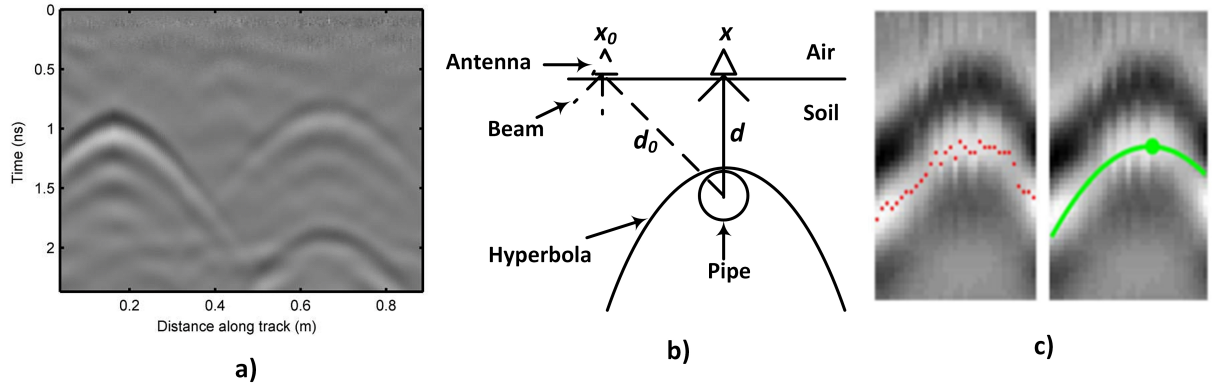


Figure 3.4.2: (a) GPR image showing three hyperbolas [111]; (b) formation of diffraction hyperbola; (c) hyperbola curve fitting [112].

$$d_0^2 = (x - x_0)^2 + d^2 \quad (3.4.1)$$

Substituting  $d_0 = v \times t_0 / 2 + R$  and  $d = v \times t / 2 + R$  into Equation 3.4.1 yields:

$$\frac{(t + \frac{2R}{v})^2}{(t_0 + \frac{2R}{v})^2} = \frac{[2(x - x_0)]^2}{(\frac{vt_0}{2} + R)^2} \quad (3.4.2)$$

Extensive pipeline networks, both underground and encased in concrete, are common features of nuclear facilities and are used for transporting liquid wastes [8]. Therefore, they constitute a significant amount of potential radioactive wastes that need to be characterised for effective decommissioning. However, their location in addition to inaccurate records makes their characterisation difficult. For instance, the

UK has approximately 760 km of pipelines on nuclear sites out of which only about 26% have been characterised [8]. Typical detection of significant contamination in shallow buried pipes consists of a ground-level survey along the length of the pipe with a sensitive radiation detector [9]. However, the depth of the radiation source is required in order to know the intensity of the radiation at the pipe location, so as to implement the required safety measures before and during decommissioning. Furthermore, knowledge of the condition of the pipe is important so as not to destroy the pipe during excavation, thereby contaminating the surrounding soil. However, this contextual information is not available from a simple ground-level radiation measurement, thereby making pipeline decommissioning particularly challenging.

However, this required contextual information can be readily supplied by GPR. For instance, the depth of the pipes can be obtained from the GPR and used for 3D localisation of the contaminated hot spot (see Section 3.5). This can be used to guide automated systems, such as robots, to carry out the decommissioning operation. Furthermore, since the intensity of a radioactive source varies with the inverse of the square of the distance, a high level fusion framework can be design to integrate the radiation and GPR datasets to automatically identify and classify hot spots using the estimated radiation intensity. Such a system can be trained with historical data to be able to identify and distinguish significant contamination in pipes from background radiation in a variety of underground environments.

### 3.4.2 Non-destructive investigation of concrete structures

GPR is widely used as a non-destructive technique in monitoring the health of concrete structures such as bridges, dams, tunnels, etc. Some of these applications include: moisture and chloride ingress; detection of reinforced steel bar (rebar) corrosion; and detection of voids and cracks [54, 112, 113]. GPR techniques for detecting moisture and chloride in concrete are based on energy loss by the GPR signals to water molecules and chloride ions due to increased conductivity. This can be detected as an increase in the attenuation of the reflected signals (Figure 3.4.3a). GPR detection of concrete rebar corrosion makes extensive use of hyperbola detection techniques described in Section 3.4.1. This is because reflections from corroded rebar are weaker than reflections from non-corroded rebar and are displayed as lighter hyperbola traces in GPR images (Figure 3.4.3b). This information can then be processed to produce a deterioration map of the concrete structure [112].

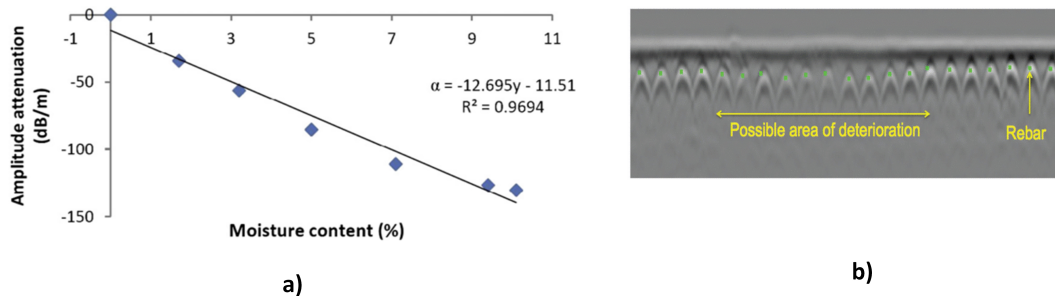


Figure 3.4.3: (a) GPR signal attenuation with varying moisture content in a concrete sample where  $\alpha =$  attenuation ( $\text{dB m}^{-1}$ ),  $y =$  moisture content (%) [54]; (b) GPR image of concrete showing weak reflections from possibly corroded rebar [112].

Concrete is a ubiquitous construction material used extensively in nuclear sites

due to its shielding ability [11, 13]. Therefore, it is the main component of many structures, such as reactor containments and biological shields at nuclear sites. Contamination of these concrete structures is as a result irradiation from fission products and from leaks and spills of liquid contaminants during operations [10]. Furthermore, interaction between the concrete and these contaminants results in defects [11], thereby enabling the contamination to penetrate deep into the concrete, and can even lead to neutron activation of the concrete rebar. Decontamination of concrete for free release is done by removing the contaminated layers using methods such as scarification [13]. However, without knowledge of the depth of the contamination, the amount of material to be removed can only be known by continuous radiation survey after each pass of the equipment, which is expensive and time wasting. In addition, if the contamination is beyond certain depths, it is usually more cost effective to adopt complete removal of the structure rather than scarifying [10].

The use of GPR to detect the state of the rebar might be a useful technique for estimating the depth of contamination. However, this assumes that the contaminant has penetrated to the rebar, which is not always true. A more robust solution is to analyse the changes in the electrical properties (i.e. permittivity and conductivity) of concrete as a result of the presence of radioactive sources and finding correlations between these changes and reflected GPR signals. This is because GPR signals are responsive to changes in the electrical properties of the medium in which they propagate. These correlations can then serve as a basis for fusing the GPR and radiation data in order to develop new techniques for non-destructive characterisation of internal contamination in concrete structures.

## 3.5 Combined GPR and radiation imaging for 3D localisation of radioactive contamination in underground pipes

Localisation of radiation sources in 3D space is an important part of radiological characterisation. This section uses MCNPX (Version 2.7) [114] and gprMax (Version 3.0) [115] modelling and simulations to demonstrate the inadequacy of ground-level radiation imaging for localising underground contamination and how additional information from GPR can help to localise the contamination in 3D, thereby resolving ambiguities.

### 3.5.1 Methodology

The modelled environment (Figure 3.5.1a) is a section of two underground pipes used for transporting liquid radioactive wastes. Both pipes are separated vertically and horizontally with contamination located at their crown beneath the points (1 and 2) indicated in the figure. This type of internal contamination is mostly due to scale build-up on the internal surfaces of pipes or accumulation of sludge and silt in pipes and can be detected at the ground surface for shallow buried pipes [8, 9]. The MCNPX model (Figure 3.5.1b) consisted of two cast iron pipes (internal radius = 4 cm, external radius = 5 cm, density =  $7.15 \text{ g cm}^{-3}$ ) buried in dry sand (density =  $1.7 \text{ g cm}^{-3}$ ). The contaminated points were modelled as Co-60 point sources (a common radioac-

tive contaminant in pipes [8]) with relative strengths of 0.15 and 0.85 for Sources 1 and 2, respectively. In gprMax, the environment was modelled as a 2D slice along section x-x, which is centred at the  $y$ -axis (Figure 3.5.1c). A 2D GPR model was used because the modelled environment is symmetrical about the  $x$ -axis. Furthermore, the pipes were modelled as two perfect electrical conducting cylinders buried in dry sand (relative permittivity = 3.89).

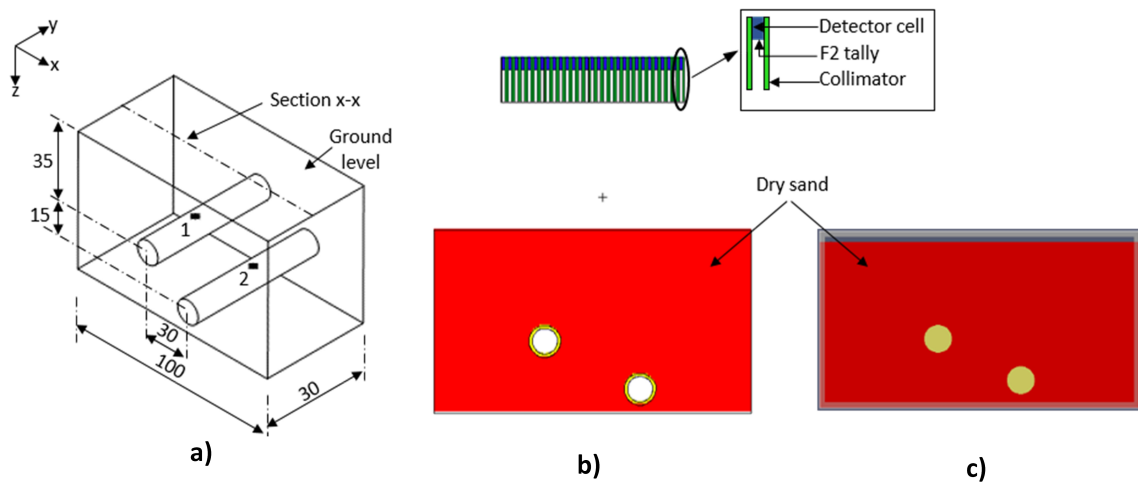


Figure 3.5.1: (a) Modelled contaminated environment (dimensions in cm); (b) MCNPX model with grid of detectors (section x-x); (c) gprMax model (section x-x).

The radiation image was acquired by a  $29 \times 15$  grid of detectors (Figure 3.5.1b) placed 40 cm above the ground and centred at the  $x$ - $y$  plane. This is equivalent to moving a single detector in  $29 \times 15$  discrete positions on the ground surface. This number of grids was chosen because they were enough to cover the area occupied by both pipes. Each detector (Figure 3.5.1b inset) consisted of a cylindrical cell (radius = 0.5 cm and height = 3 cm) surrounded by 0.5 cm-thick tungsten collimator, which is 14 cm long. The MNCPX F2 tally was placed at the bottom of the detector cell

to record all gamma photon events at that surface. The GPR data were obtained by a co-located transmitter-receiver Hertzian dipole pair at 256 locations along section  $x$ - $x$ . It should be noted that in practice, the path along which to acquire the GPR measurements can be determined from the acquired radiation image. Furthermore, the GPR transmitter was excited with a Gaussian wavelet centred at 1 GHz because of the relatively shallow depth of the pipes. In order to minimise dispersion errors, the GPR simulation used a spatial resolution of  $\Delta x = \Delta y = 0.002$  m, which is less than one tenth of the smallest wavelength present in the model. Finally, the temporal resolution  $\Delta t$  was calculated to be 4.7 ps using the Courant, Freidrichs and Lewy stability condition given by (3.5.1), where  $c$  is the wave velocity in free space.

$$\Delta t \leq \frac{1}{c \sqrt{\frac{1}{\Delta x^2} + \frac{1}{\Delta y^2}}} \quad (3.5.1)$$

### 3.5.1.1 Matched filter synthetic aperture radar imaging

The GPR data was processed using the matched filter synthetic aperture radar (SAR) imaging algorithm [110]. Consider the monostatic linear collection scenario in Figure 3.5.2. The data  $d(u, t)$  collected along the cross range are the time delayed, amplitude scaled version of the point spread response (PSR)  $s(u, t - t_d)$  of the stationary scatterer at  $(x, y)$  where the time delay  $t_d$  is given by (3.5.2) ( $v$  is the wave velocity in the medium). However, for a signal corrupted with additive white Gaussian noise, the optimum match filter is the conjugate of the time reversed version of the signal of interest [110]. Therefore, the matched filtered output at a given location is given by the convolution of the collected data and the conjugate of the PSR at that location.

This convolution operation is given by (3.5.3).

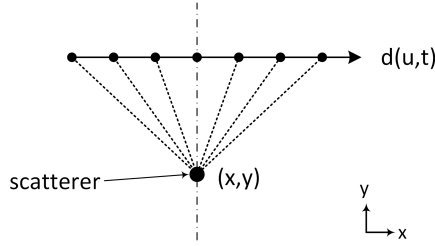


Figure 3.5.2: Monostatic linear SAR data collection.

$$t_d = \frac{2}{v} \sqrt{(u - x)^2 + y^2} \quad (3.5.2)$$

$$I(x, y) = d(u, t) * s^*(u, t - t_d) = \int_{-\infty}^{\infty} \int_{-\infty}^{\infty} d(u, t) s^*(u, t - t_d) du dt \quad (3.5.3)$$

In matched filter SAR imaging, the PSR is calculated for each pixel and applied to the collected data using (3.5.3). This results in an image where pixels in the location of scatterers have higher signal to noise ratios compared to surrounding pixels. Finally, even though the matched filter SAR algorithm requires significant processing power for large datasets, it is however robust and has practical applications for small and moderate datasets.

### 3.5.2 Simulation results

The radiation image is shown in Figure 3.5.3a after resampling and smoothing with a  $25 \times 25$  pixel Gaussian window [21]. As expected, the vertical separation between the two pipes is not observable in the radiation image because of the lack of depth information. Furthermore, the fact that Source 2 is measured as having a higher intensity could easily be misconstrued to imply that Source 2 is closer to the surface than

Source 1. Figure 3.5.3b shows the GPR image after processing with the matched filter SAR imaging algorithm described in Section 3.5.1.1. This yields the required depth information, as it shows the points where the GPR signals were reflected by the pipe surfaces. Using this depth information, the radiation image can be projected into the ground to yield a 3D localised radiation image (Figure 3.5.3c), thereby resolving any ambiguity associated with the lack of depth information. Note that only pixels with normalised intensity  $\geq 0.7$  for both sources were projected back to the pipe locations. This integration of GPR and radiation imaging is similar to the passive integration methods described in Section 3.3.1 where the radiation image is projected into a 3D visual image of the environment. However, the use of GPR rather than visual sensors enabled the detection of the pipe beyond the ground surface, thereby allowing the contaminated spot to be localised on the pipe surfaces. Furthermore, this 3D image can be used to guide automated systems, such as robots, during decommissioning of the contaminated pipes.

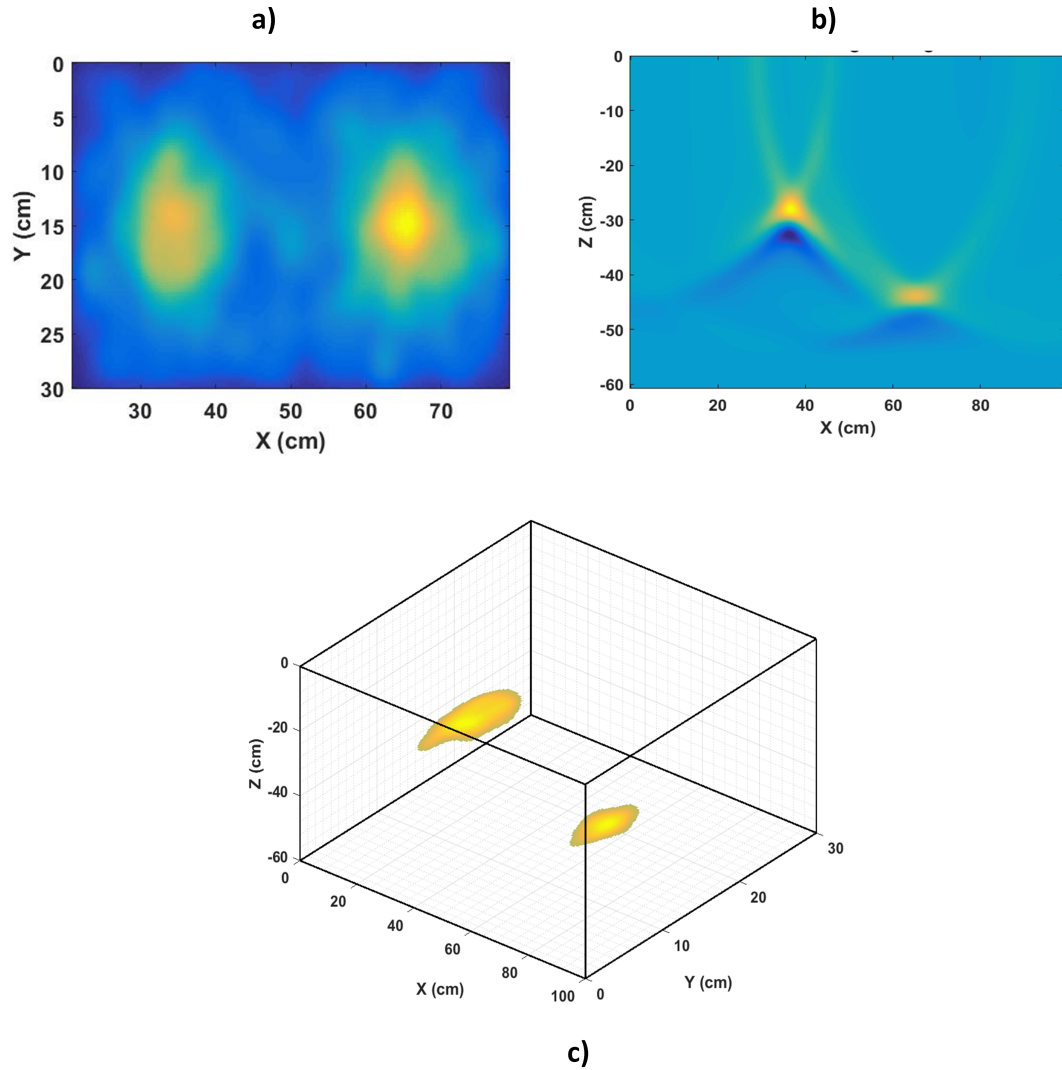


Figure 3.5.3: (a) Ground level image of radiation sources; (b) matched filtered GPR image of pipes; (c) 3D localised image of radiation sources.

However, it must be noted that these simulations assume an idealised scenario where the effects of noise, both from background radiation and clutter in the radiation and radar images, respectively, were not considered. However, techniques for dealing with noise encountered both in radiation and radar images from the field have been presented in the literature [85, 109]. In addition, the retrieved depth of the con-

tamination assumes that each pipe's thickness is negligible so that the distances from the ground surface to both the pipe's surface and the pipe's crown (actual location of the contamination) are approximately the same. This is a practical assumption as the thickness of typical metallic and PVC pipes used in nuclear pipelines are between 5 and 12 mm [8]. Finally, another potential improvement is the simultaneous reconstruction of the GPR and radiation data at the point of reflection (i.e. the pipe surfaces). This will require acquisition of GPR measurements at multiple slices along the  $y$ -axis (i.e. 3D GPR data) so that points in the radiation data that correlate with points in the GPR data can be backprojected during reconstruction of the GPR image. The output of such an algorithm will be a 3D fused image of the radiation and GPR data at the pipe surface similar to the output of the 3D volume fusion technique described in Section 3.3.2.1.

## 3.6 Conclusion

Recent applications of integrated radiological and contextual sensors techniques for detecting and localising radioactive sources in non-medical field have been reviewed. The use of contextual sensors enabled the retrieval of additional contextual information about the radiation source, thereby enabling characterisation of radioactive sources in challenging scenarios. However, these applications are dominated by the use of visual sensors as contextual sensors. Furthermore, visual sensors cannot retrieve contextual information about radioactive wastes in visually-inaccessible locations typically encountered at nuclear sites and facilities. Therefore, GPR was proposed and

examined as a contextual sensor for characterising such wastes in light of the techniques presented in the reviewed literature.

Furthermore, it was identified that integration of GPR and radiological sensors will potentially enable non-intrusive characterisation of radioactive wastes in nuclear sites and facilities especially in two critical areas namely: (1) contaminated pipelines buried underground or encased in concrete and (2) contamination ingress into porous materials, such as concrete. This will enable rapid characterisation of wastes in these hard to access areas while reducing dosage risks and the generation of secondary wastes. However, more research is required in order to understand and identify correlating attributes in both GPR and radiation datasets acquired from these contaminated environments. This is because multi-sensor integration techniques rely on establishing relationships among the data from the participating sensors.

Finally, the presented simulation results have demonstrated the effectiveness of combined GPR and radiation imaging for 3D localisation of contamination in buried pipelines by projecting the radiation image back to the pipe location. 3D localisation is an important part of the characterisation process, and such 3D localised images can be used to guide automated systems, such as robots, during decommissioning of the contaminated pipes. However, a 3D reconstruction algorithm needs to be developed in order to enable simultaneous reconstruction of the radiation and GPR data at the point of reflection. This will yield a fused radiation and GPR image with improved localisation of the contaminated region compared to simply projecting the radiation image back to the location of the pipes. Furthermore, the implementation of the reconstruction algorithm can take advantage of available fast microprocessors

to enable real-time reconstruction of the underground contaminated environment.

### **3.7 Acknowledgment**

The authors would like to acknowledge the funding support from the Engineering and Physical Sciences Research Council (EPSRC), U.K. (EPSRC Grant Number EP/N509231/1) and the Nuclear Decommissioning Authority, U.K.

# Chapter 4

## A Novel Method for Remote Depth Estimation of Buried Radioactive Contamination

I. K. Ukaegbu and K. A. A. Gamage

*Sensors*, 18(2):507, 2018. DOI: 10.3390/s18020507

### 4.1 Abstract

Existing remote radioactive contamination depth estimation methods for buried radioactive wastes are either limited to less than 2 cm or are based on empirical models that require foreknowledge of the maximum penetrable depth of the contamination. These severely limits their usefulness in some real life subsurface contamination scenarios. Therefore, this work presents a novel remote depth estimation method that

is based on an approximate three-dimensional linear attenuation model that exploits the benefits of using multiple measurements obtained from the surface of the material in which the contamination is buried using a radiation detector. Simulation results showed that the proposed method is able to detect the depth of caesium-137 and cobalt-60 contamination buried up to 40 cm in both sand and concrete. Furthermore, results from experiments show that the method is able to detect the depth of caesium-137 contamination buried up to 12 cm in sand. The lower maximum depth recorded in the experiment is due to limitations in the detector and the low activity of the caesium-137 source used. Nevertheless, both results demonstrate the superior capability of the proposed method compared to existing methods.

## 4.2 Introduction

A significant amount of radioactive waste is generated during the life cycle of a typical nuclear facility e.g., nuclear power plant [10]. These wastes can be by-products of radioactive materials such as nuclear fuels or previously non-radioactive materials that become contaminated either through contact with radioactive materials or through activation by ionising radiation. Characterisation of these wastes is critical in decommissioning these facilities because it provides vital information required for effective planning, dismantling, transporting and storage of these wastes to meet nuclear regulatory standards [116, 117].

A key step in the characterisation process is the localisation of these wastes [118]. However, some of these wastes can be in difficult to access areas, which causes their

localisation to be particularly challenging. Examples of such wastes commonly encountered during decommissioning of nuclear facilities include wastes buried inside porous materials such as concrete and soil. The contamination of concrete structures is usually due to ingress of radioactive contaminants as a result of irradiation or leaks and spills [10]. Furthermore, these contaminants can also interact with the constituent of the concrete resulting in cracks that allow the contaminants to penetrate deeper into the concrete structure over time [11]. There are several pathways through which anthropogenic radiological contaminants can end up in the soil. This include leaks from underground waste transportation pipes and storage ponds [8], deliberate burial of wastes in the soil [7] and particles from radiological fallouts that precipitate into the soil [119]. For instance, the reported contamination at the beaches of Northern Scotland covers an area of about 200,000 m<sup>2</sup> and consists mainly of caesium-137 fuel fragments with activities of up to 10<sup>8</sup> Bq buried at depths of less than 1 m [5, 6].

The major difficulty in localising wastes buried in concrete or soil is the determination of the depth of penetration of the contamination. This is because of the visually opaque nature of these porous materials. However, knowledge of the depth of penetration of these contaminants is vital in choosing the most cost-effective decommissioning strategy. For instance, decommissioning concrete structures is usually a trade-off between scarification and designation of the entire concrete structure as waste [13]. However, scarification is expensive and time wasting if the contamination is found to have penetrated deeper than expected. On the other hand, designation of the entire concrete structure as wastes significantly increases the volume and cost of wastes to be disposed if the contamination is shallow. Therefore, the importance

of effective depth profiling methods for entrained contamination cannot be over emphasised. Traditional depth profiling methods include: Logging, Micro drilling and Core sampling [7, 20]. However, these methods are destructive and time-consuming. In addition, they also have limited spatial extent for sampling.

Consequently, various remote depth profiling methods have been investigated and reported in literature. These include: the relative attenuation method [12, 120, 121] and principal component analysis (PCA) method [122–124]. The relative attenuation method exploits the relative difference in the attenuation of two prominent peaks (typically the X-ray and gamma photo peaks) in the measured energy spectrum of the buried radionuclide. However, the use of the X-ray photo peak limits the maximum detectable depth to less than 2 cm due to high attenuation of the X-rays. Furthermore, the technique is not effective for radionuclides such as cobalt-60 (Co-60) that do not emit sufficient X-rays [120]. The PCA method is based on a non-linear regression model that correlates a derived variable referred to as the synthetic angle with the depth of the buried radionuclide. The synthetic angle is the inverse tangent of the ratio of the first two principal components of a set of measured spectra of the radioactive source for different burial depths. However, such empirical models are data dependent. Consequently, the model parameters change whenever a new spectra is added to the original data [124]. This makes the model useful only when the maximum penetrable depth of the contamination is known a priori.

Therefore, this paper presents a novel remote depth estimation method for buried radioactive contamination based on an approximate three-dimensional (3D) linear attenuation model. Both simulation and experimental results have shown that the

method has significantly improved depth profiling ability in both concrete and soil compared to existing remote techniques thereby increasing its range of application. The next section presents the derivation of the 3D linear attenuation model and the simulation and experimental setups. The results and discussions are presented in Sections 4.4 and 4.5, respectively, while conclusions and future directions are presented in Section 4.6.

## 4.3 Materials and methods

### 4.3.1 The approximate 3D linear attenuation model

Consider a point source  $S$  buried in a section of a material at a depth  $z$  from the front surface as shown in Figure 4.3.1. The intensity  $I_{(x,y,z)}$  of the source measured by a collimated detector at any position on the  $x$ - $y$  plane (i.e. the material surface) is given by:

$$I_{(x,y,z)} = I_{(x,y,0)} e^{-\mu(x^2+y^2+z^2)^{\frac{1}{2}}}, \quad (4.3.1)$$

where  $I_{(x,y,0)}$  is the intensity at any position on the  $x$ - $y$  plane when the source is at  $z = 0$  and  $\mu$  is the linear attenuation coefficient. Equation (4.3.1) is the well-known linear attenuation model [26] in 3D coordinates. Furthermore, Equation (4.3.1) can also be re-written as:

$$I_{(x,y,z)} = I_{(x,y,0)} e^{-\mu z \left(1 + \frac{x^2+y^2}{z^2}\right)^{\frac{1}{2}}}. \quad (4.3.2)$$

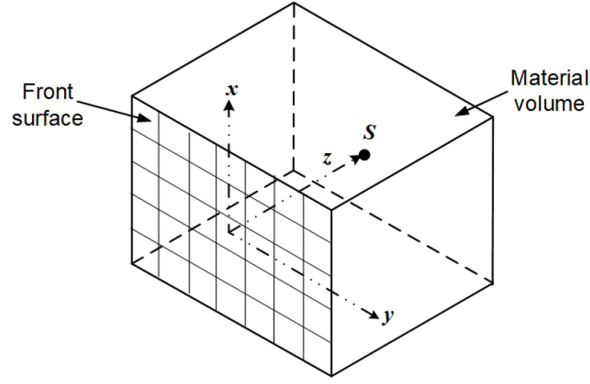


Figure 4.3.1: A point radioactive source buried in a section of a material.

Expanding the index of the exponential term in Equation (4.3.2) using the binomial theorem and retaining only the first two terms of the binomial expansion results in:

$$I_{(x,y,z)} \approx I_{(x,y,0)} e^{-\mu(z + \frac{x^2}{2z} + \frac{y^2}{2z})}. \quad (4.3.3)$$

However, it can be observed in Figure 4.3.1 that the intensity at the centre position of the  $x$ - $y$  plane (i.e.  $x = y = 0$ ) is given by:

$$I_{(0,0,z)} = I_{(0,0,0)} e^{-\mu z}. \quad (4.3.4)$$

Therefore, dividing Equation (4.3.3) by Equation (4.3.4) results in Equation (4.3.5), which can be rewritten as Equation (4.3.6):

$$\frac{I_{(x,y,z)}}{I_{(0,0,z)}} \approx \frac{I_{(x,y,0)}}{I_{(0,0,0)}} e^{-\frac{\mu}{2z}(x^2 + y^2)}, \quad (4.3.5)$$

$$\log_e(J_{(x,y,z)}) \approx -\frac{\mu}{2z}(x^2 + y^2) + \log_e(K_{(x,y,0)}), \quad (4.3.6)$$

$$\text{where: } J_{(x,y,z)} = \frac{I_{(x,y,z)}}{I_{(0,0,z)}} \quad \text{and} \quad K_{(x,y,0)} = \frac{I_{(x,y,0)}}{I_{(0,0,0)}}.$$

Equation (4.3.6) is the approximate linear attenuation model of the intensity measured at any position on the  $x$ - $y$  plane normalised by the intensity measured at the

central position on the same plane. This is valid for  $x^2 + y^2 < z^2$ , which is the validity condition of the binomial expansion. Therefore, it can be deduced that, for a source buried at some depth  $z$ , the graph of  $\log_e(J_{(x,y,z)})$  against  $x^2 + y^2$  for all  $x^2 + y^2 < z^2$  should be a straight line passing through the origin since  $\log_e(K_{(x,y,0)}) = 0$  at  $x = y = 0$ . However, since  $z$  is not known, the normalised intensities from all the measured positions can be plotted and a weighted curve fitting method used to fit a straight line through the best points. The approximate depth of the radioactive source from the surface of the material can then be calculated from the slope of the fitted line. However, it is important to account for the dependence of the linear attenuation coefficient on the energy of the emitted photons. This can be done by using only gamma photons from a section of the measured energy spectrum over which the linear attenuation coefficient can be assumed to be constant. Theoretically, any region of the spectrum can be used since Equation (4.3.6) is a ratio of two spectra. However, the ideal region of interest is obviously the characteristic photo-peak region of the buried radionuclide.

### 4.3.2 Monte Carlo modelling and simulation

In order to validate the derived model, Monte Carlo modelling and simulations were performed using MCNPX version 2.7 (Los Alamos National Laboratory, Los Alamos, New Mexico, USA). MCNPX is a radiation transport code used to simulate the transportation and interaction of atomic particles in different media using Monte Carlo statistics [114]. A sketch of the MCNPX model used for the simulations is shown in Figure 4.3.2. It consists of an array of  $n \times n$  detectors placed on the surface of a

section of a material of uniform density where  $n$  depends on the grid (or detector) size and the total surface area to be measured. This configuration is equivalent to moving a single detector in  $n \times n$  discrete locations across the material surface. Each detector (Figure 4.3.2 inset) is made up of a cylindrical detector cell surrounded by a 0.1 cm-thick square collimator. The MCNPX F2 tally was used to record all gamma photons crossing the front surface of the detector cell. The MCNPX F2 tally measures the average flux over a given surface area, i.e. number of particles per  $\text{cm}^2$  [114]. In order to prevent crosstalk among neighbouring detectors, the collimator was set to be completely impenetrable by gamma photons.

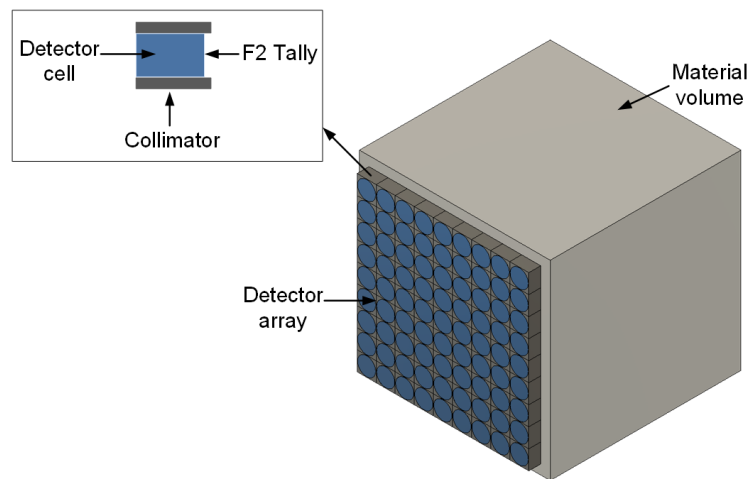


Figure 4.3.2: Sketch of the MCNPX simulation model.

Two radionuclides, namely: caesium-137 (Cs-137) and Co-60, were used in the simulations. These are by-products of the nuclear fuel cycle commonly encountered during decommissioning [124]. Both radionuclides were modelled as radioactive point sources. Furthermore, three different materials, namely: sand, ordinary dry concrete and high density concrete, were investigated. The properties of these materials are as

shown in Table 4.3.1. Finally, for each material, a radionuclide was buried at varying depths ranging from 2 to 40 cm at 2 cm increments. At each depth, a total of  $10^8$  gamma particles were generated and the total number of gamma rays crossing each detector surface were recorded together with their corresponding energies.

Table 4.3.1: Densities and elemental composition of the three materials used in the simulation. The information was obtained from [125].

Elements	Weight Fraction		
	Sand <i>(density = 1.7 g cm<sup>-3</sup>)</i>	Ordinary Concrete <i>(density = 2.18 g cm<sup>-3</sup>)</i>	High Density Concrete <i>(density = 3.35 g cm<sup>-3</sup>)</i>
H	0.007833	0.004000	0.003585
C	0.003360	-	-
O	0.536153	0.482102	0.311622
Na	0.017063	0.002168	-
Mg	-	0.014094	0.001195
Al	0.034401	0.069387	0.004183
Si	0.365067	0.277549	0.010457
K	0.011622	0.013010	-
Ca	0.011212	0.080229	0.050194
Fe	0.013289	0.057461	0.047505
S	-	-	0.107858
Ba	-	-	0.463400
	1.000000	1.000000	1.000000

### 4.3.3 Experiment setup

The experiment setup is as shown in Figure 4.3.3a. It consists of a sandbox filled with fine silica sand in which a radioactive source was buried. The sandbox was constructed using 0.8 cm thick Perspex sheets (Direct Plastics Ltd., Sheffield, UK) because of its relative transparency to gamma radiation. This ensures that the scattering of the gamma radiation is almost exclusively due to the sand matrix. The radioactive source used was a sealed 392 kBq Cs-137 radioactive point source. The source was attached to one end of a graduated Ploy vinyl chloride pipe whose other end protrudes behind the sandbox (Figure 4.3.3b). This enables the distance of the source from the front of the sandbox (i.e. scanning surface) to be easily varied and the value read off from the pipe.

The detector used in the experiment consists of an organic liquid scintillator and a photomultiplier tube enclosed in a cylindrical aluminium case whose diameter is 3.5 cm and height is 9.13 cm. The organic liquid scintillator is the EJ-301 from Eljen Technology (Sweetwater, Texas, USA) with a scintillation efficiency of 12,000 photons/MeV [126]. The entire detector assembly was placed inside the tungsten collimator shown in Figure 4.3.3a. The collimator is a hollow cylinder open at both ends with an internal diameter of 4 cm, thickness of 1 cm and length of 25 cm. The use of the tungsten collimator was to ensure that only gamma photons within the detector's field of view are detected. However, since no material can provide 100% shielding, some gamma photons are still able to penetrate through the walls of the collimator. For instance, the collimator has a penetration of 14.4% at 662 keV for

photons striking the curved surface at  $90^\circ$ . However, it is obvious from the experiment setup that none of the photons leaving the sandbox will strike the curved surface of the collimator at  $90^\circ$ . Therefore, assuming a maximum striking angle of  $45^\circ$ , a photon will travel a minimum thickness of 1.4 cm resulting in a significantly lower penetration of 6.4%. Finally, the collimator was mounted on a custom fabricated motorised mount to enable automated and accurate positioning at specified  $x$ - $y$  coordinates.

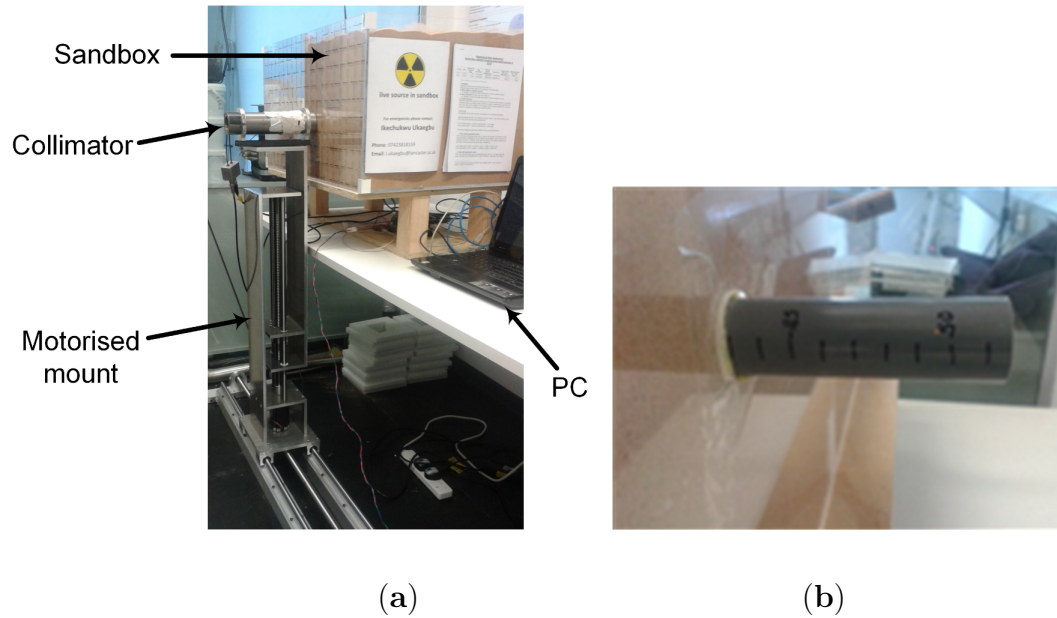


Figure 4.3.3: (a) Experiment setup; (b) Graduated pipe for adjusting the distance of the source from the front of the sandbox.

During the experiment, the source was positioned at the centre of the scanning surface while its distance from this surface was varied from 2 cm to 14 cm at 2 cm intervals. At each distance, the spectrum of the source was measured on a total scan area of  $28 \times 28 \text{ cm}^2$ , which was divided into  $4 \times 4 \text{ cm}^2$  cells where a cell represents the area covered by the detector at that position. This yields a total of 49 spectra per distance. Finally, a scanning time of 10 min per position was used in the experiment.

## 4.4 Results

### 4.4.1 Simulation results for Cs-137 buried in sand

The normalised radiation image of the Cs-137 point source buried in sand and acquired using a cell size of  $4 \times 4 \text{ cm}^2$  and a maximum scan area of  $36 \times 36 \text{ cm}^2$  are shown in Figure 4.4.1. The intensity of each pixel is the number of gamma photons with energy between 640 and 662 keV detected by the detector at that position. This part of the energy spectrum was chosen because it contains the characteristic photo-peak of Cs-137. As expected, the intensities of the images gradually spreads out to neighbouring pixels as the depth of the source increases. This is mainly due to increasing spreading of the emitted gamma rays and scattering of the photons by the sand matrix. This makes the photons be detected by an increasing number of detectors as the source depth increases.

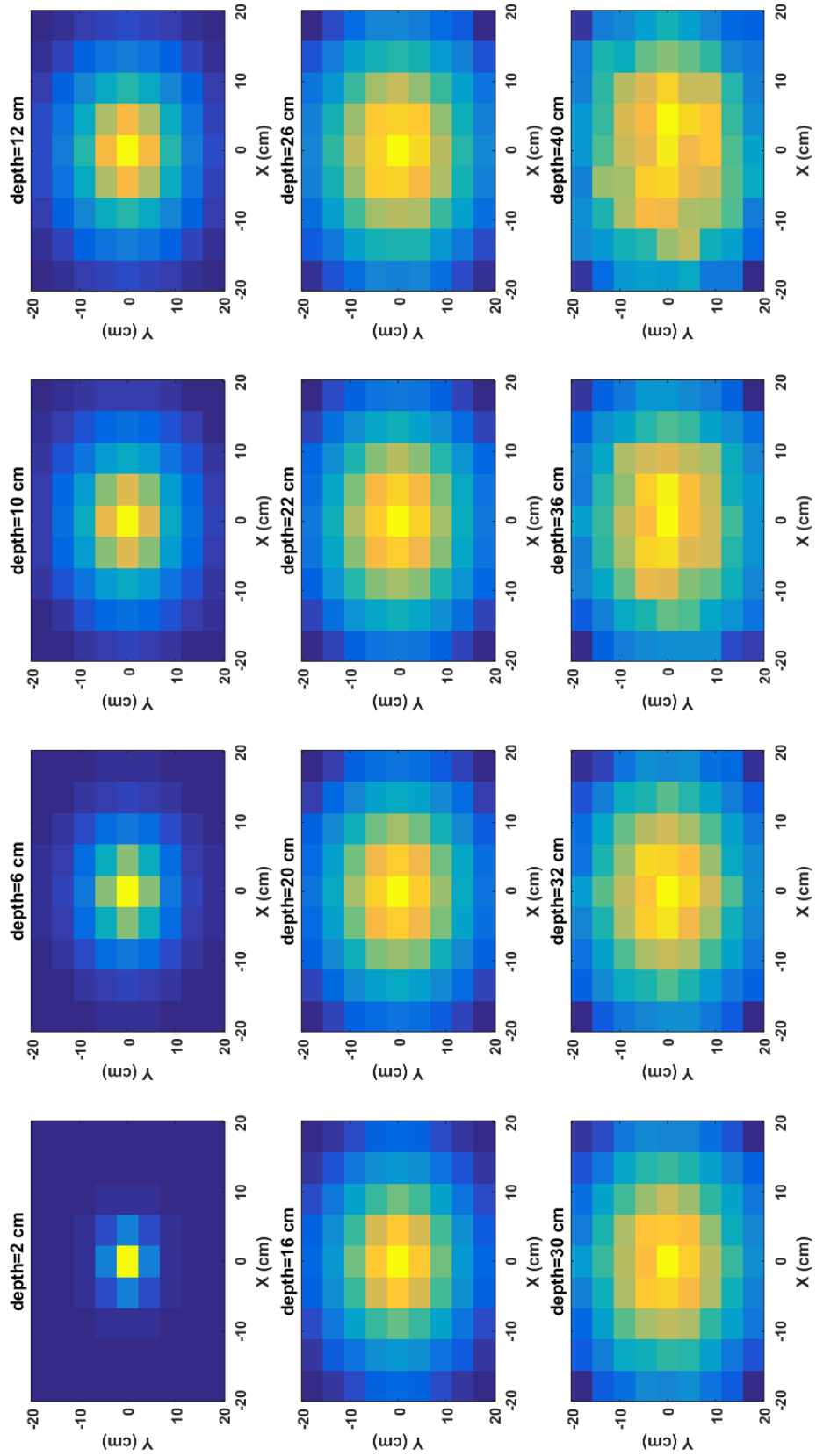


Figure 4.4.1: Normalised radiation images of Cs-137 buried in sand for selected depths.

The graph of the model (i.e. Equation (4.3.6)) for each of the images in Figure 4.4.1 are shown in Figure 4.4.2. As predicted by the model, it can be observed that the data points approach a straight line with negative slope as the depth increases. This is because more cells meet the validity condition of the binomial expansion at lower depths. Furthermore, the effects of attenuation at lower depths can be observed where the points become increasingly scattered at random about the straight line.

In order to estimate the approximate depth from the slope of the fitted line in the model plots (Figure 4.4.2), the mean linear attenuation coefficient for sand at 640–662 keV is required. This was calculated using (4.4.1), where  $\rho$  is the density of sand,  $\mu_{m,i}$  is the mean mass attenuation coefficient between 640–662 keV for each element  $i$  of the sand mixture and  $W_i$  is the weight ratio of each element  $i$  of the sand mixture. The elements that constitute the sand mixture, their weight ratios and mass attenuation coefficients were obtained from standard published tables [127]:

$$\mu = \rho \sum_{i=1}^n \mu_{m,i} W_i. \quad (4.4.1)$$

The estimated and real depths for the Cs-137 point source buried in sand are shown in Figure 4.4.3a. It can be observed that the real depth is well approximated by the estimated depth for depths of up to 5 cm. However, the estimated depth increasingly deviates from the real depth at lower depths. This seems counter intuitive at first glance because it is expected that more cells should fulfil the validity condition of the binomial expansion at lower depths; consequently, lower depths should be better approximated than shallow depths. However, this increasing error at lower depths is as a result of the exponential increase in the truncation error caused by se-

lecting only the first two terms of the binomial expansion. However, of more practical importance is the linear relationship between the real and estimated depths as shown in Figure 4.4.3b. This shows that the real depth can be predicted from the estimated depth by a simple calibration.

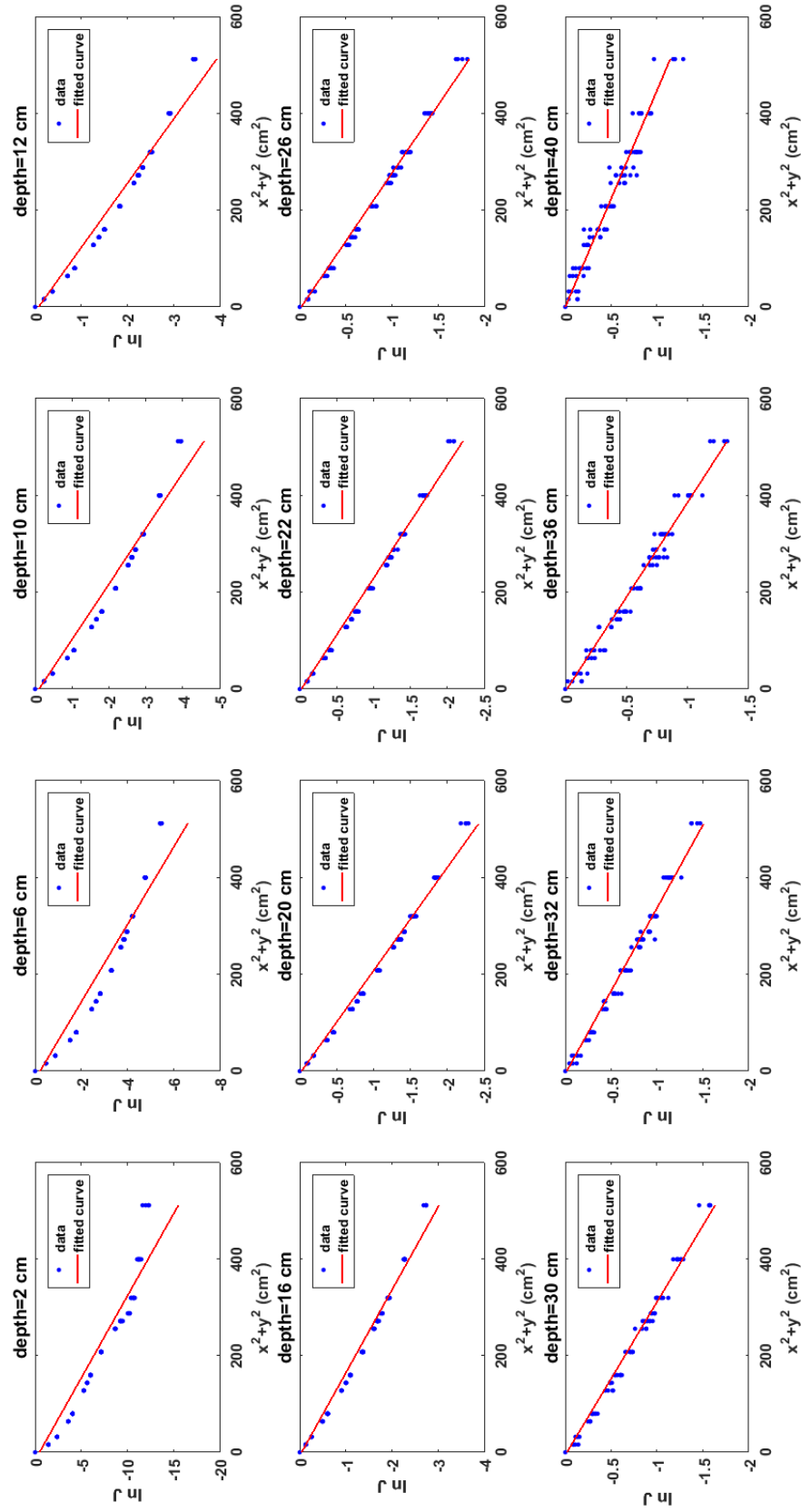


Figure 4.4.2: Plots of model for Cs-137 buried in sand for selected depths.

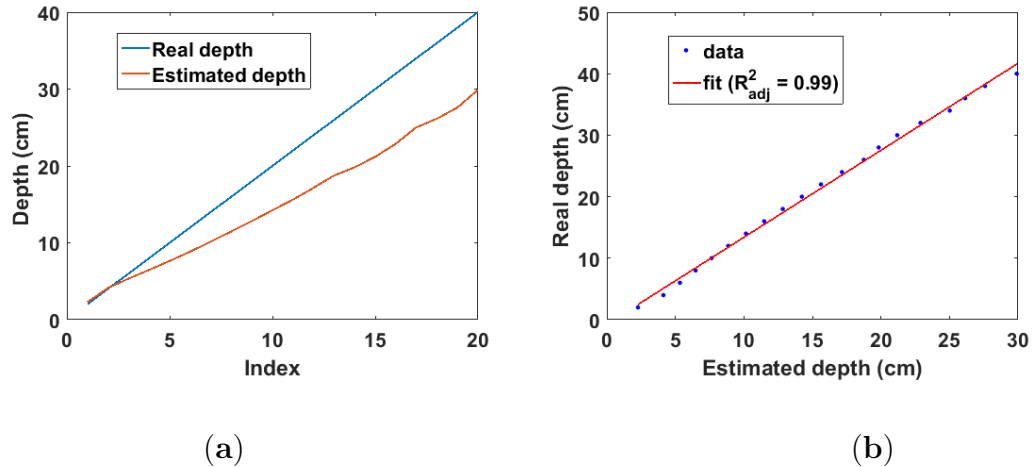


Figure 4.4.3: (a) Real and estimated depths for Cs-137 buried in sand. Index is the position of each depth value in the depth array; (b) Linear fit of real and estimated depth for Cs-137 buried in sand.

#### 4.4.1.1 Effects of scan area and grid cell size

The two parameters that affect the estimated depth using the proposed method are the size of the grid cells and the total scan area. This is because they determine the depth beyond which the binomial expansion used in the derivation of (4.3.6) becomes valid. For instance, smaller cell sizes increase the number of cells that meet this validity condition, thereby yielding more valid points, which increases the accuracy of the fitted line from which the approximated depth is estimated. However, as can be observed from Figure 4.4.4a, larger cell sizes result in smaller errors in the estimated depth compared to smaller cell sizes. This suggests that the number of gamma photons detected per cell is an important factor because larger cell sizes (i.e. larger detectors) detect more gamma rays per cell compared to smaller cell sizes. However, cell sizes beyond  $3 \times 3 \text{ cm}^2$  yield only marginally smaller errors. Figure 4.4.4b shows the

error per depth for different scan areas using a fixed cell size of  $4 \times 4 \text{ cm}^2$ . As expected, larger scan areas yield smaller errors with a consistent linear relationship with the depth. However, a sudden drop in the error for depths above 30 cm can be observed for the smaller scan area of  $20 \times 20 \text{ cm}^2$ . This is probably due to error in the Monte Carlo statistics as the same trend is not observed for Co-60 buried in sand (see Subsection 4.4.3). Finally, though a larger scan area will yield better estimates, practical limitations such as available space and time may place a limit on the maximum surface area that can be scanned.

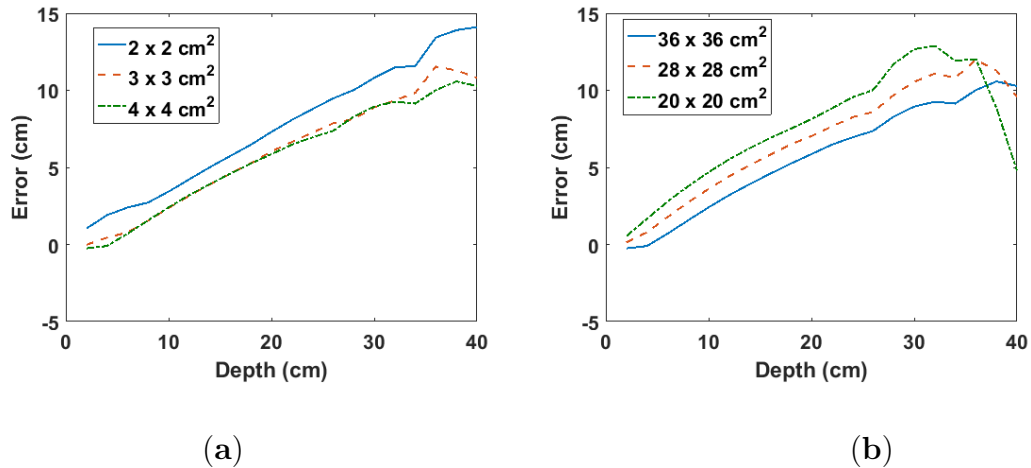


Figure 4.4.4: (a) Error per depth for different cell sizes for Cs-137 buried in sand; (b) Error per depth for different scan areas for Cs-137 buried in sand.

#### 4.4.2 Simulation results for Cs-137 buried in concrete

Figure 4.4.5a,b shows the linear fit of the estimated and real depths for the two types of concrete, respectively. The effects of attenuation of the emitted gamma rays in both types of concretes can be observed. This corresponds to the region where the data points begin to lose their linearity. Furthermore, as expected, this loss of linearity is

more pronounced in the higher density concrete. This shows that Equation (4.3.6) correctly models the attenuation behaviour of gamma rays in different materials.

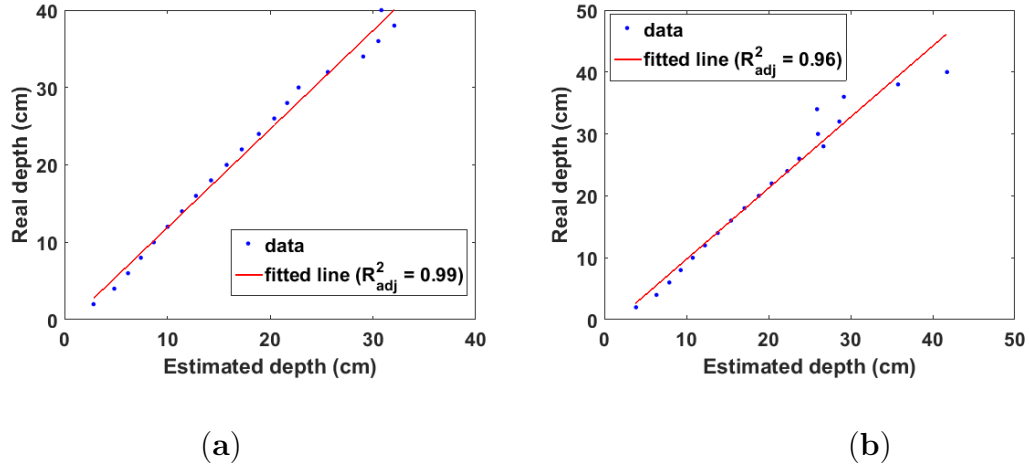


Figure 4.4.5: (a) Linear fit of estimated and real depth for Cs-137 buried in concrete of density =  $2.18 \text{ g cm}^{-3}$ ; (b) Linear fit of estimated and real depth for Cs-137 buried in concrete of density =  $3.35 \text{ g cm}^{-3}$ .

### 4.4.3 Simulation results for Co-60 buried in sand and concrete

Co-60 is known to have two prominent photo-peaks at 1.17 MeV and 1.33 MeV on its energy spectrum. The results using photon counts from both photo-peak regions are shown in Figure 4.4.6a,b. The same error pattern in the estimated depth as seen in Cs-137 can also be observed. This proves the consistent behaviour of the proposed model. Furthermore, there is no significant difference in the estimated depth using photon counts from either photo-peaks. This is because the probability of Co-60 emitting gammas with either energies is almost equal in addition to the fact the difference

between both energies is not substantial. It can be observed in Figures 4.4.7a,b that larger cell sizes and scan areas yield better estimates similar to the results obtained for Cs-137. This shows that the behaviour of these parameters is independent of the energy of the gamma rays.

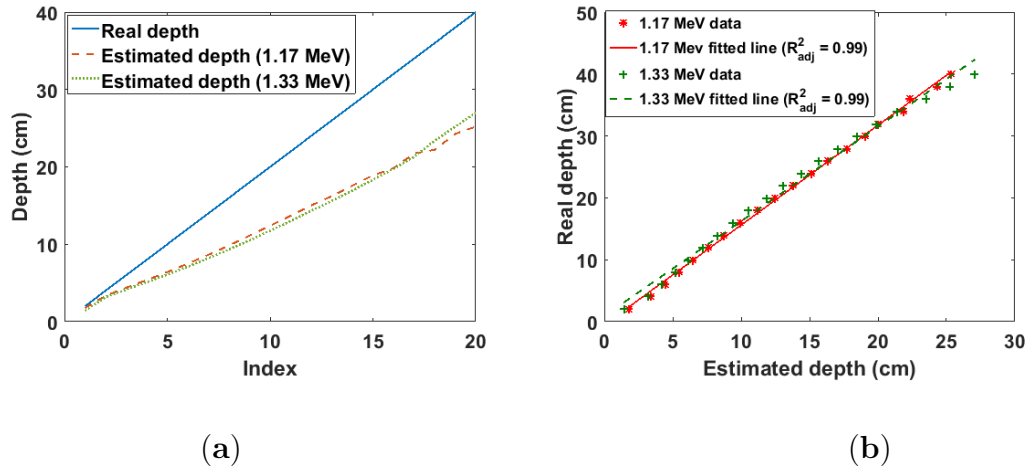


Figure 4.4.6: (a) Real and estimated depths for Co-60 buried in sand. Index is the position of each depth value in the depth array; (b) linear fit of real and estimated depth for Co-60 buried in sand.

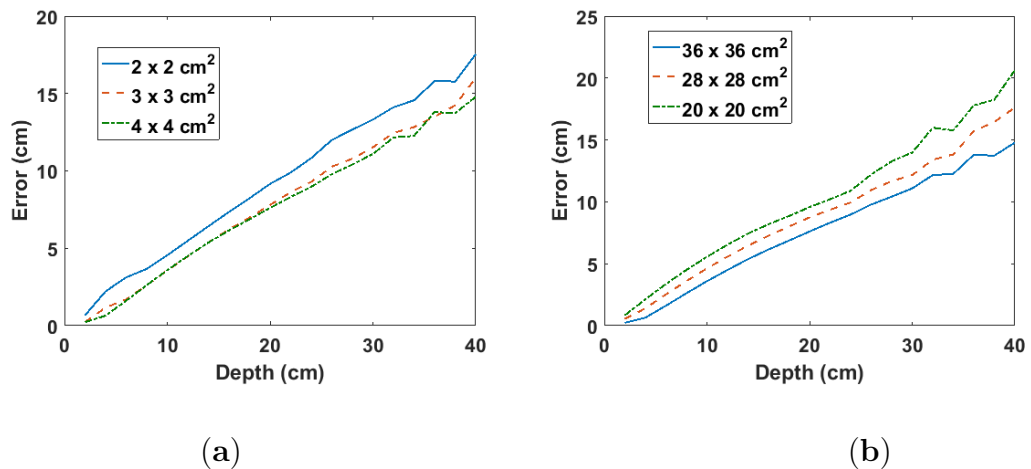


Figure 4.4.7: (a) Error per depth for different cell sizes for Co-60 buried in sand; (b) Error per depth for different scan areas for Co-60 buried in sand

The linear fit of the estimated and real depths for Co-60 buried in the two types of concrete are shown in Figure 4.4.8. As can be observed, the depth at which there is significant uncertainty in the estimated depth due to attenuation is lower compared to the case of Cs-137 (4.4.5). This is as expected because attenuation decreases with increasing gamma energy. Consequently, Co-60 should have a higher maximum detectable depth compared to Cs-137 when buried in the same material.

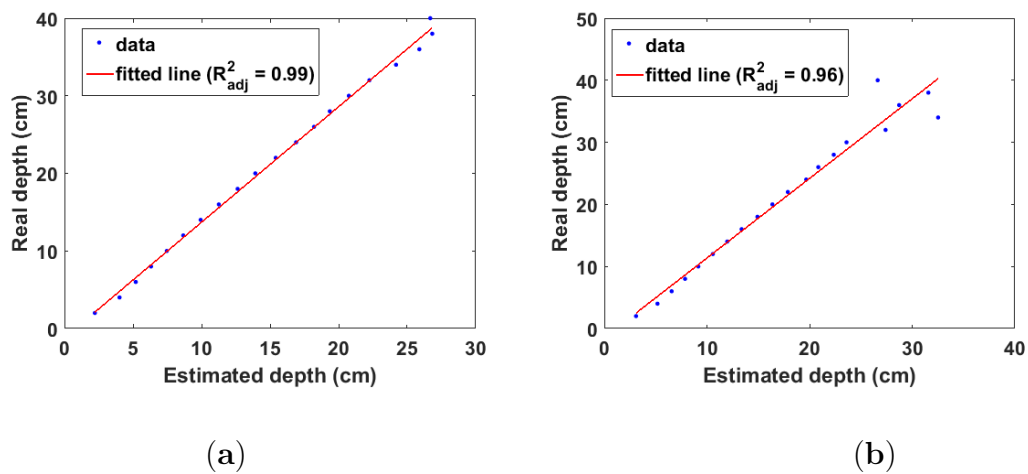


Figure 4.4.8: (a) Linear fit of estimated and real depth for Co-60 buried in concrete of density  $= 2.18 \text{ g cm}^{-3}$ ; (b) Linear fit of estimated and real depth for Co-60 buried in concrete of density  $= 3.35 \text{ g cm}^{-3}$ .

#### 4.4.4 Experiment results

As pointed out in Section 4.3.1, any region of the measured energy spectrum can theoretically be used in the depth estimation. This is especially useful for detectors that cannot detect the characteristic photo-peak of the entrained radionuclide such as the detector used in the experiment. Therefore, gamma photons from the Compton

peak were used in estimating the depth from the measured spectra. This corresponds to the energy range between 451 to 500 keV. The radiation images and corresponding model plots for selected source depths from the experiment are shown in Figure 4.4.9. The same trend seen in the simulation results can be observed. However, one or two outlier data points due to measurement errors can be seen in the model plots (Figure 4.4.9 bottom row).

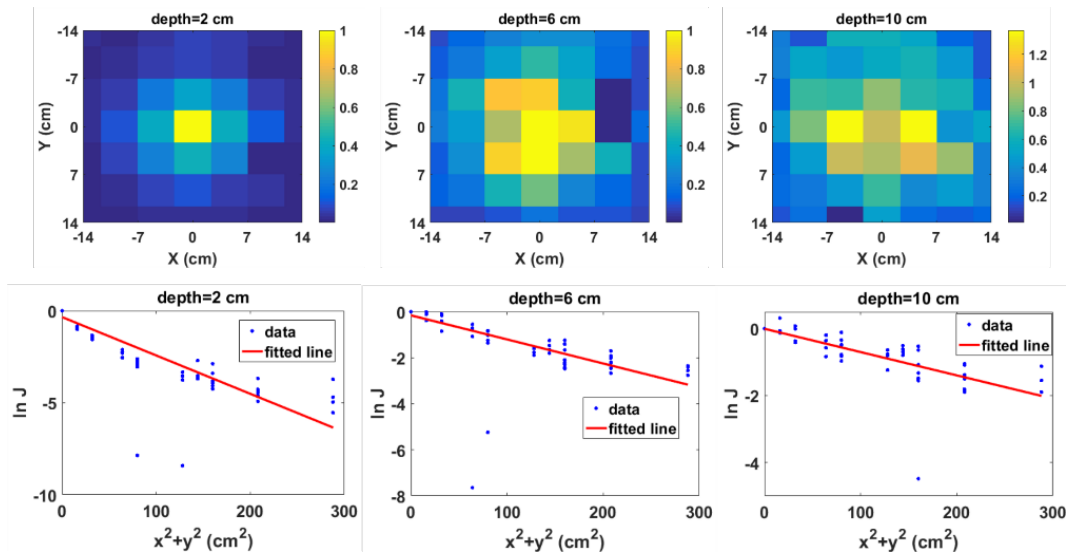


Figure 4.4.9: Normalised 2D radiation images using photons from the Compton peak region (**top row**) and corresponding model plot (**bottom row**) for selected depths from the experiment.

The real and estimated depths from the experiment are shown in Figure 4.4.10a. It can be observed that the real depth is well approximated by the estimated depth up to 10 cm. Beyond 12 cm, the effect of attenuation becomes significant, resulting in large errors in the estimated depth. This is also observed in the linear fit between the real and estimated depths (Figure 4.4.10b), where a depth of 29 cm was estimated

from the model when the real source depth is 14 cm. Due to this large error, this data point was not included in fitting the data. Therefore, the maximum detectable depth for the experiment setup is 12 cm with an adjusted R-squared value of 0.79. However, this depth is lower compared to that obtained from the simulation results. This can be attributed to three main factors, the first of which is the weak activity of the sealed Cs-137 point source used in the experiment. Secondly, unlike the simulation, the experiment used a realistic collimator therefore, its estimates will be affected by the uncertainties caused by photons that penetrate through the walls of the collimator; and, finally, the simulation used photons from the photo-peak region which are higher in number and energy compared to photons in the Compton peak region and are therefore less susceptible to attenuation.

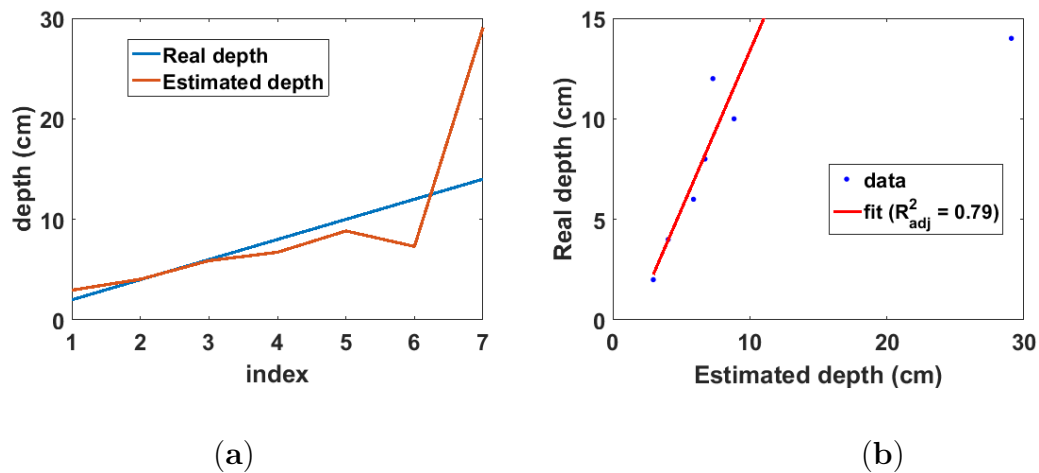


Figure 4.4.10: (a) Real and estimated depths from experiment. Index is the position of each depth value in the depth array; (b) Linear fit of real and estimated depths from experiments.

## 4.5 Discussion

The simulation and experiment results show that the proposed technique has significant advantages compared to existing remote contamination depth estimation methods. First, it has significantly higher maximum detectable depth, thereby increasing its range of applications. For instance, in a recent technical report [9], it was identified that significant internal contamination in pipes buried up to 50 cm deep can be detected on the ground surface using a radiation detector. The proposed method will enable non-intrusive monitoring and characterisation of such pipelines through remote 3D localisation of internal contamination. Secondly, the experiment results showed that the method can be used with non-spectroscopic gamma radiation detectors such as plastic scintillators [128]. This is advantageous because these type of detectors are cheaper compared to other type detectors.

The main limitation of the proposed method is in the estimation of the linear attenuation coefficient of the material in which the radionuclide is buried. This is because it requires foreknowledge of the mass attenuation coefficient and density of the entraining material (see Equation (4.4.1)). However, Table 4.5.1 shows that the average mass attenuation coefficient for a given energy range is relatively constant for different materials. Therefore, the problem of estimating the linear attenuation coefficient is reduced to that of finding only the density of the entraining material. While a table of the densities of common materials can be prepared, such a solution does not take into account the changes the material may have undergone overtime due to environmental factors. Therefore, a better solution will be to integrate data

from other non-intrusive techniques such as ground penetrating radar as proposed in [129]. This multi-sensor data fusion solution will enable real-time determination of the entraining material properties and also potentially improve the accuracy of the estimated depth.

Table 4.5.1: Average mass attenuation coefficients for different materials at the photo-peak region of Cs-137 and Co-60 calculated from [127].

Material	Cs-137		Co-60
	600–700 keV	1.1–1.2 keV	1.3–1.4 keV
Sand	0.0800	0.0606	0.0557
Concrete 1 (2.18 g cm <sup>-3</sup> )	0.0795	0.0602	0.0553
Concrete 2 (3.35 g cm <sup>-3</sup> )	0.0809	0.0576	0.0526

## 4.6 Conclusion

A novel method for remote depth estimation of radioactive contamination has been presented. The method is based on a derived approximate 3D linear attenuation model and exploits the information obtained from multiple measurements of the intensity of the radiation on the surface of the material in which the contamination is buried. Results from simulations and experiments of Cs-137 and Co-60 contaminations in sand and concrete showed significantly improved remote depth estimation capabilities compared to existing methods. Finally, the proposed method will significantly enhance the non-intrusive characterisation of buried radioactive wastes commonly encountered

during the decommissioning of nuclear sites and facilities.

## **4.7 Acknowledgement**

This work was supported by the Engineering and Physical Sciences Research Council and Nuclear Decommissioning Authority, UK (EP/N509231/1).

# Chapter 5

## A Model For Remote Depth

## Estimation of Buried Radioactive

## Wastes Using a CdZnTe Detector

I. K. Ukaegbu and K. A. A. Gamage

*Sensors*, 18(5):1612, 2018. DOI: 10.3390/s18051612

### 5.1 Abstract

This paper presents the results of an attenuation model for remote depth estimation of buried radioactive wastes using a CZT detector. Previous research using an organic liquid scintillator detector system showed that the model is able to estimate the depth of a 329-kBq Cs-137 radioactive source buried up to 12 cm in sand with an average count rate of 100 cps. The results presented in this paper showed that the use of the

CZT detector extended the maximum detectable depth of the same radioactive source to 18 cm in sand with a significantly lower average count rate of 14 cps. Furthermore, the model also successfully estimated the depth of a 9-kBq Co-60 source buried up to 3 cm in sand. This confirms that this remote depth estimation method can be used with other radionuclides and wastes with very low activity. Finally, the paper proposes a performance parameter for evaluating radiation detection systems that implement this remote depth estimation method.

## 5.2 Introduction

Wastes generated during the nuclear fuel cycle can end up in the soil, resulting in large-scale land contamination. This is the case in the beaches of Dounreay in Northern Scotland where wide-spread radioactive soil contamination has been reported [5, 6]. This was caused by the so-called Dounreay particles resulting from the processing of the fuels from the Material Test Reactor at the Dounreay nuclear facility. These particles consist mainly of caesium-137 (Cs-137) fuel fragments buried at depths less than 40 cm and extending over an area of about 200,000 m<sup>2</sup>. Other sources of shallow subsurface radioactive contamination include: leaks from waste pipes [8, 9] and radioactive fallout from nuclear tests [119]. The characterisation of these subsurface wastes has continued to be a major nuclear decommissioning challenge [121]. This is mainly because of the difficulty in estimating the depth of penetration of these contaminants without having recourse to destructive methods such as logging or core sampling [7, 20]. Furthermore, reported non-intrusive depth estimation methods for

such wastes are either based on empirical models [123, 124] or are limited to a maximum depth of 3 cm [12, 120].

Consequently, a novel remote depth estimation method for buried waste was recently developed [130]. This method is based on an approximate three-dimensional linear attenuation model that makes use of multiple radiation measurements obtained from the surface of the material in which the radioactive contaminant is buried. The results from simulation showed that the method is able to estimate the depth of radioactive point sources buried up to 40 cm in both sand and concrete. Furthermore, results from initial experiments using an organic liquid scintillator (EJ-301) from Eljen Technologies (Sweetwater, TX, USA) and a high-speed multichannel analyser MFAx1.3 from Hybrid Instruments Limited (Lancaster, Lancashire, U.K.) achieved a maximum detectable depth of approximately 12 cm at an average count rate of 100 cps, where the average count rate is defined as the average of the count rates at each depth when the detector is located axially with the source. These preliminary results indicate that improved results can be obtained using a radiation detector with a better gamma spectral response. This is because the gamma spectral response of the EJ-301 scintillator is limited to the Compton continuum.

Therefore, this paper presents improved results from the depth estimation method using a CZT detector. The CZT detector is a semiconductor detector that is well known for its good spectral response at room temperature [131]. Consequently, it is widely used in the characterisation of nuclear materials in fields such as nuclear safeguarding and decommissioning [24, 132]. The paper also reports on the effect of data acquisition time on the depth estimation performance of the method and pro-

poses a performance parameter for evaluating systems that will implement the depth estimation method. The next section gives a detailed description of the materials and methods used in the research. The experimental results are presented and discussed in Section 5.4, while the conclusions and future directions are presented in Section 5.5.

## 5.3 Materials and methods

### 5.3.1 The approximate three-dimensional linear attenuation model

Let  $I_{(x,y,z)}$  be the radiation intensity measured at any position  $(x, y)$  on the surface of a material volume in which a radiation source is buried at depth  $z$ . The ratio of this intensity to that measured from a reference position (i.e.  $(x, y) = (0, 0)$ ) on the same surface is given by:

$$\log_e(J_{(x,y,z)}) \approx -\frac{\mu}{2z}(x^2 + y^2) + \log_e(K_{(x,y,0)}) \quad (5.3.1)$$

where  $J_{(x,y,z)} = \frac{I_{(x,y,z)}}{I_{(0,0,z)}}$ ,  $\mu$  = linear attenuation coefficient and  $K_{(x,y,0)} = \frac{I_{(x,y,0)}}{I_{(0,0,0)}}$ . Equation (5.3.1) is the approximate three-dimensional linear attenuation model derived in a previous work [130]. It expresses the ratio of the intensity measured at any position on the surface of the material volume to that measured at the reference position on the same surface. Furthermore, it can be deduced that the approximate depth of the source can be estimated from the gradient of the model. The gradient can be obtained by fitting a linear polynomial to the graph of the model for a set of spectra acquired

from multiple positions on the surface of the material volume in which the source is buried. The simulation result of this procedure for Cs-137 buried in sand at depths from 2 cm to 20 cm at 2-cm intervals is shown in Figure 5.3.1. The deviation observed at increasing depth is as a result of the approximation made in the derivation of Equation (5.3.1). The details of the model derivation and a comprehensive analysis of the simulation results have been reported in [130].

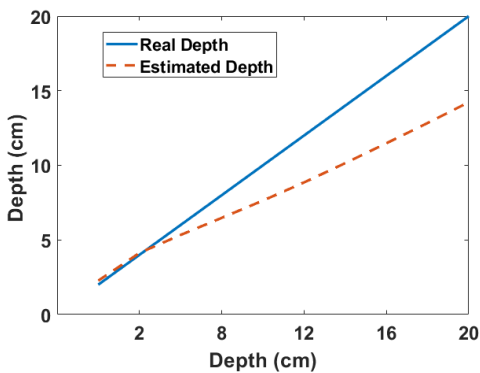


Figure 5.3.1: Estimated depth from the simulation of the Cs-137 point source buried in sand [130]

### 5.3.2 Experiment

The experimental setup (Figure 5.3.2) consisted of a sandbox filled with sand in which the radiation source was placed at varying distances from the front surface. The walls of the box were 0.8 cm thick and were constructed using acrylic plastic sheets. The density of the sand was  $1.66 \text{ g cm}^{-3}$ , and the weight fractions of its composite elements obtained using Scanning Electron Microscopy (SEM) are shown in Table 5.3.1. The radiation source was attached to one end of a plastic pipe whose other end protruded behind the box. This was used to vary the position of the source along the  $z$ -axis.

The detector was placed inside the cylindrical tungsten collimator shown in Figure 5.3.2 so that only gamma rays within the detector's field of view were detected at each  $x$ - $y$  position. The collimator was 1 cm thick, 25 cm tall and had an internal diameter of approximately 4 cm. Furthermore, the collimator was attached to a motorised mount for automated positioning of the detector at each specified position on the front surface of the sandbox.

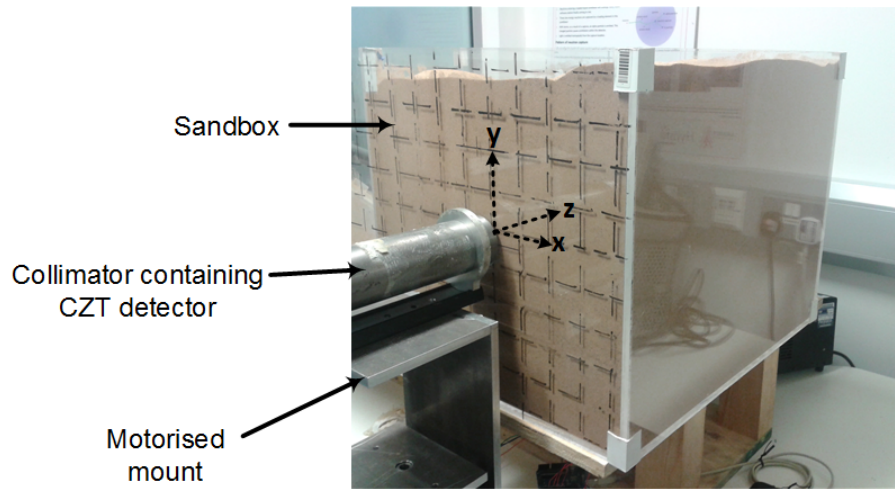


Figure 5.3.2: Setup for the experiment. The Cs-137 point source was placed at varying positions along the  $z$ -axis using a pipe that protruded behind the box, while the intensity was measured at the grid positions marked on the surface of the sandbox.

Table 5.3.1: Elemental composition from SEM analysis of the sand used in the experiment.

<b>Element</b>	<b>Weight Fraction</b>
C	0.1714
O	0.5163
Na	0.0013
Al	0.0151
Si	0.2755
K	0.0072
Ca	0.0006
Fe	0.0072
P	0.0003
S	0.0004
Ti	0.0005
Cu	0.0009
Mg	0.0020
Zn	0.0014
	1.0000

In order to acquire the data, the total scanning area was set to  $28 \times 28 \text{ cm}^2$ , which was divided into  $4 \times 4 \text{ cm}^2$  grids. The size of the grids were chosen to be approximately equal to the internal diameter of the collimator. The radiation source

was then positioned at distances (i.e. depths) varying from 2 cm to 20 cm at 2-cm intervals from the front of the sandbox. At each depth, the detector was moved across the scanning area, and the spectrum of the buried source was measured at each grid, thereby yielding a total of 49 spectra per depth.

### 5.3.3 Spectrum acquisition and pre-processing

The detector used in the experiment was the CZT/500S detector from Ritec (Riga, Latvia). It is a quasi-hemispherical CZT detector with a sensitive volume of  $0.5 \text{ cm}^3$  and is enclosed in a cylindrical casing of diameter 2.2 cm and height 3.3 cm. Therefore, it was able to fit inside the collimator used in the experiment. The output from the detector was connected to a charge-sensitive low noise preamplifier (PA101C also from Ritec), and the output pulses were sampled by an oscilloscope (sampling rate = 500 kS/s) controlled by a Personal Computer (PC). After digitisation by the oscilloscope, the pulses were then transferred to the PC via Ethernet for Pulse Height Analysis (PHA). The stages of the PHA are as shown in Figure 5.3.3. It consists of a fast and a slow processing channels whose outputs are used by the pile-up rejector to estimate the height of suitable pulses. The details of the PHA are discussed as follows:

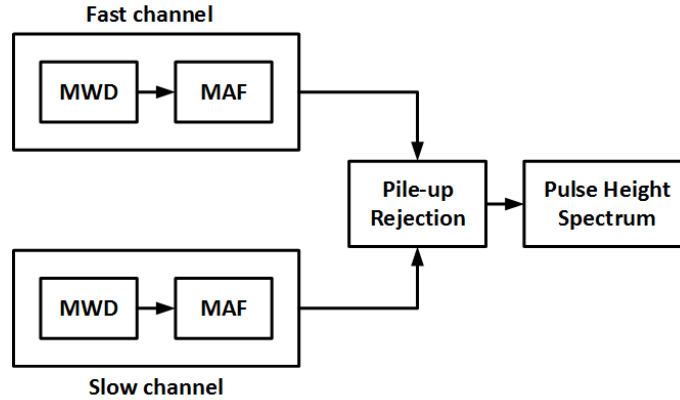


Figure 5.3.3: Pulse height spectrum analysis algorithm used in the experiment where MWD is the Moving Window Deconvolution and MAF is the Moving Average Filter.

(a) Moving window deconvolution:

The moving window deconvolution (MWD) is an efficient filter proposed by Georgiev et al. [133] for the retrieval of the amplitude of the step pulse from the output of the preamplifier. The charge collected when a photon strikes the CZT crystal creates a fast rising step in the output of the preamplifier with an amplitude that is proportional to the amount of charge collected. However, the step decays exponentially at a rate determined by the time constant of the preamplifier. This delay of the signal to return to baseline prevents the accurate measurement of the amplitude of subsequent voltage steps. However, since the output from the preamplifier is a convolution of the charge distribution function and the impulse response of the preamplifier, deconvolving this output signal will enable the reconstruction of the original charge distribution function while eliminating poles from the preamplifier transfer function [133]. The MWD

performs this deconvolution in a moving time window and is given by:

$$MWD(i) = X(i) - X(i - M) + \frac{1}{\tau} \sum_{j=i-M}^{i-1} X(j) \quad (5.3.2)$$

where  $X(i)$  is the value of the signal at the  $i$ -th sample,  $M$  is the window size and  $\tau$  is the preamplifier time constant in units of sample time. It can be observed that the MWD is a differentiator followed by an integration term that compensates for the exponential decay using the time constant of the preamplifier.

(b) Moving average filter:

The moving average filter is an optimum constant weight smoothing filter suitable for reducing random noise. It was applied to the output of the MWD so as to reduce the noise level without affecting the energy resolution [134]. It is given by:

$$MAF(i) = \frac{1}{L} \sum_{j=i-L}^{i-1} MWD(j) \quad (5.3.3)$$

where  $L$  is the filter length. The value of  $L$  in relation to the MWD window size  $M$  determines the output pulse shape. For instance,  $L < M$  results in trapezoidal shaping, while  $L = M$  results in triangular shaping.

(c) Pile-up rejection:

Pile-up is caused by two or more events occurring within the duration of the length of the shaping filter (i.e. the window size of the MWD). This causes the events to be processed into a single pulse resulting in the wrong estimation of the pulse

amplitude. The need to reduce pile-ups is usually in conflict with the need to ensure complete charge collection. This is because while long shaping times increase the probability of complete charge collection, they also increase the occurrence of pile-ups, especially at high count rates. Pile-up rejection was implemented in PHA by having two processing channels: a slow channel with a longer shaping time for increased probability of complete charge collection and a fast channel with a shorter shaping time for resolving closely occurring events. Therefore, any pulse from the slow channel with more than one pulse within the same duration in the fast channel is rejected as a pile-up.

The PHA algorithm was implemented in MATLAB (Natick, MA, USA) and used to process the pulses transferred from the oscilloscope. The Cs-137 spectrum obtained after 50,000 counts using long and short filter shaping times of 10  $\mu\text{s}$  and 7  $\mu\text{s}$ , respectively, is shown Figure 5.3.4. It can be observed that all the key features of the Cs-137 gamma spectrum can be clearly identified.

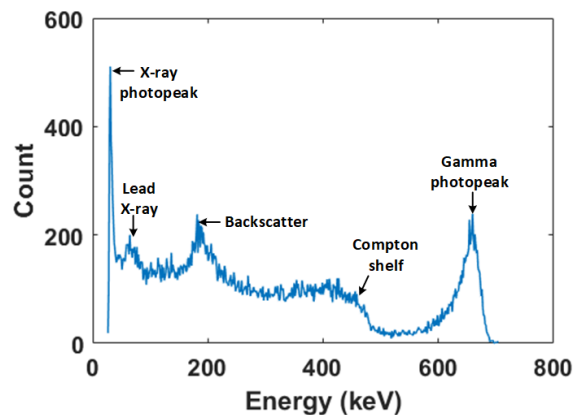


Figure 5.3.4: Cs-137 spectrum from the Pulse Height Analysis (PHA) algorithm after 50,000 counts.

### 5.3.3.1 Photo-peak fitting

One of the problems with the spectrum produced by CZT detectors is the elongated low-energy tail of the photo-peak. This is because of incomplete charge collection caused by early carrier recombination due to low hole mobility within the CZT crystal [135]. Consequently, the obtained spectrum photo-peaks are often asymmetric and cannot be adequately described by conventional Gaussian functions. Therefore, Montreau et al. [135] proposed a more robust peak fitting function given as:

$$F(i) = G(i) + S(i) + D(i) + B(i) \quad (5.3.4)$$

where  $i$  is the channel number, and  $G$  is a Gaussian function given by:

$$G(i) = A_g \exp[-(i - i_0)^2 / 2\varsigma^2] \quad (5.3.5)$$

where  $A_g$  is the amplitude of the Gaussian function,  $i_0$  is the centroid and  $\varsigma$  is the standard deviation.  $S(i)$  is a step function given by:

$$S(i) = A_s A_g \operatorname{erfc}[(i - i_0) / \sqrt{2}\varsigma] \quad (5.3.6)$$

where  $A_s$  is the height of the step.  $D(i)$  is an exponential tailing function described as:

$$D(i) = A_t A_g \exp[(i - i_0) / T_s \varsigma] \times \operatorname{erfc}[(i - i_0) / \sqrt{2}\varsigma] + 1 / (\sqrt{2} T_s) \quad (5.3.7)$$

where  $T_s$  is the inverse slope of the exponential tail. The last component of the fitting function  $B(i)$  represents background radiation; however, it can be neglected if background subtraction is performed before fitting the function to the photo-peak. Figure 5.3.5 shows the application of Equation (5.3.4) to the 662-keV photo-peak of the acquired Cs-137 spectrum. The contribution of each component of the fitting function

to the accuracy and robustness of the fit can be observed. Therefore, this photo-peak fitting function was used to analyse the spectra obtained from the experiments after background subtraction.

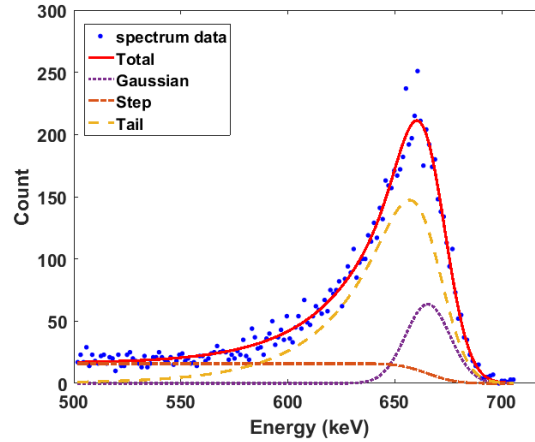


Figure 5.3.5: Cs-137 662-keV photopeak fitting using Equation 5.3.4.

## 5.4 Results and discussion

### 5.4.1 Results for caesium-137

The two-dimensional radiation image for some selected depths between 2 cm and 20 cm for a 329-kBq Cs-137 point source buried in the sandbox are shown in Figure 5.4.1. The pixel values of each image are the photon count at 662 keV of the spectrum acquired at that position on the front surface of the sandbox. In addition, the spectra were acquired using a scanning time of 25 min per  $x$ - $y$  position. It can be observed that the images show an increasing defocussing of the intensity from the centre towards the edges as the depth increases. This shows that the distribution of the intensity across the image pixels contains information about the depth of the source. Furthermore, it

can be observed that at the depth of 20 cm, the pixel intensities become randomly distributed. This is because of significant attenuation, which causes some pixels to have zero values. These zero-valued pixels represent positions where the photo-peak fitting function failed due to its inability to detect a peak. This distribution of the intensities across the image in addition to the decrease in the photon count due to attenuation are the two pieces of information exploited by this method to estimate the depth of the buried radioactive source.

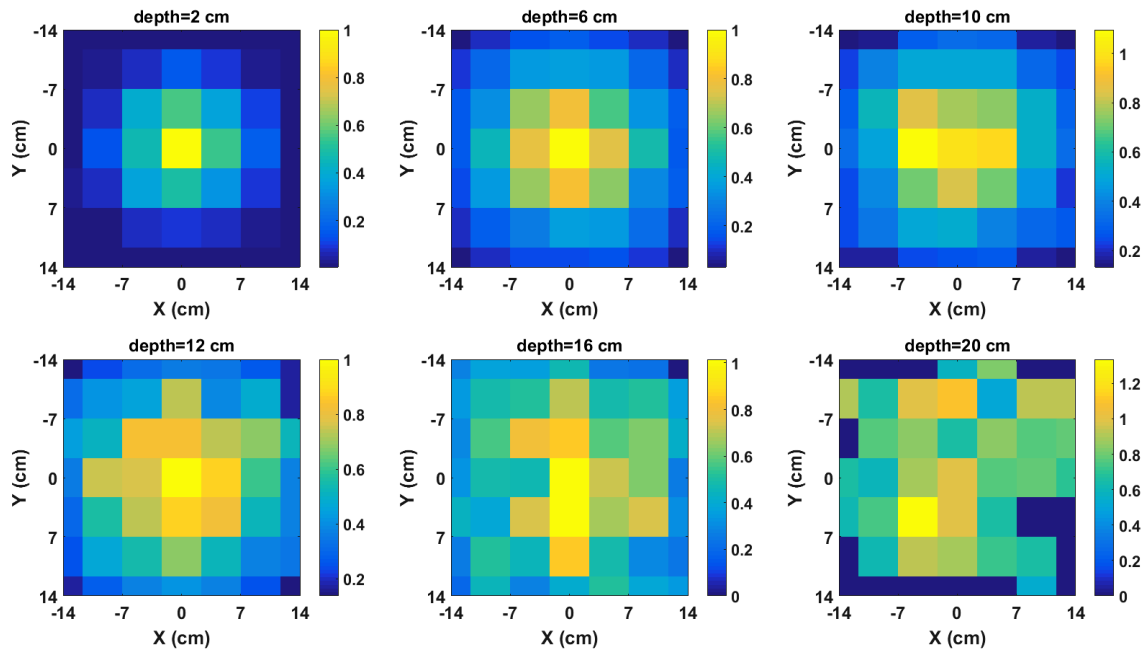


Figure 5.4.1: Normalised radiation images of Cs-137 buried in sand for selected depths.

The next step in the depth estimation process is the evaluation of the model (i.e. Equation (5.3.1)) using the radiation images. The graphs of the model for the same selection of depths whose images are shown in Figure 5.4.1 are shown in Figure 5.4.2. It can be observed that the graphs have negative gradients as predicted by the model. Furthermore, it can also be observed in the graphs in Figure 5.4.2

that the gradient of the fitted polynomial tends to zero as the depth increases. This shows that the model aptly preserves the attenuation behaviour of gamma rays in materials. In addition, it also implies that the gradient of the data points contains information about the depth of the source and that the quantity of depth information in the gradient decreases as the gradient value tends to zero where a zero gradient value means no depth information. However, it must be noted that zero represents an absolute limit because the reliability of the depth estimates will become significantly reduced even before the gradient value becomes zero.

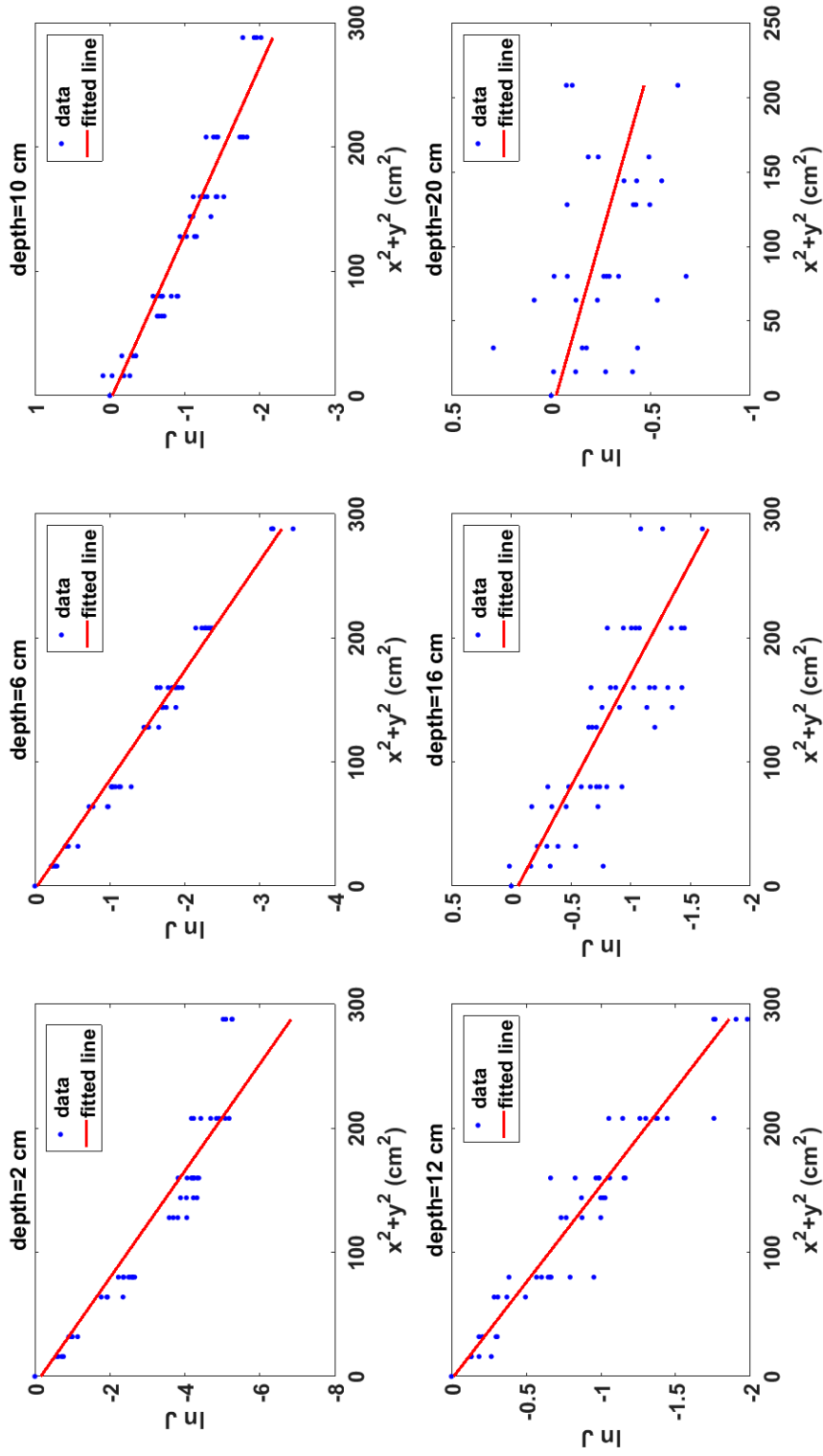


Figure 5.4.2: Graphs of the model for Cs-137 buried in sand for selected depths.  $(x, y)$  is the position of the detector on the surface of the sandbox, while  $J$  is the ratio of the intensity measured at each  $(x, y)$  to that measured at the centre of the sandbox surface.

The depths of the source estimated from the gradient of the model are shown in Figure 5.4.3a. The linear attenuation coefficient  $\mu$  at 662 keV for sand was calculated using the weight fractions in Table 5.3.1 and the mass attenuation coefficients published by the National Institute of Standards and Technology (Gaithersburg, MD, USA) [127]. It can be observed that the estimated depth approximates the real depth up to 6 cm well, after which the expected deviation from the real depth begins. As explained in [130], this deviation is a result of using only the first two terms of the binomial expansion in the derivation of the model. This deviation continues up to 16 cm, after which a slight upward jump can be observed at 18 cm. This slight jump at 18 cm indicates the depth at which the effects of attenuation begin to introduce errors to the estimate. This slight jump is followed by a complete divergence of the estimated depth from the real depth at 20 cm due to large errors in the estimate caused by significant attenuation of the gamma rays. This complete divergence in the estimated depth at 20 cm is corroborated by the complete defocussing of the radiation image at 20 cm (Figure 5.4.1) and the almost zero gradient of the fitted polynomial in the model graph also at 20 cm (Figure 5.4.2).

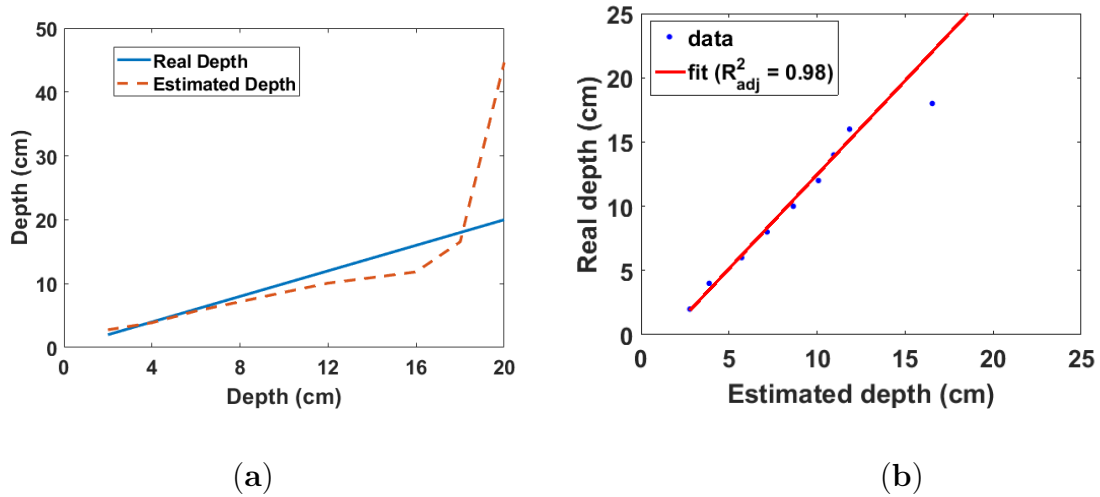


Figure 5.4.3: (a) Real and estimated depths for Cs-137 buried in sand. (b) Linear fit of real and estimated depth for Cs-137 buried in sand.

Figure 5.4.3b shows that there is a linear relationship from which the real depth can be predicted from the estimated depth up to 18 cm with an adjusted R-squared value of 0.98. A weighted linear regression was used for the polynomial fitting to limit the effect of the slight error in the estimate at 18 cm on the regression parameters. In addition, the estimate at 20 cm was not included in the polynomial fitting due to the large error in the estimate as already mentioned. The average corrected count rate obtained for this experiment was 14 cps due to the slow communication link between the PC and the oscilloscope. However, this result is a significant improvement compared to the result previously obtained using the EJ-301 scintillator [130], which achieved a maximum detectable depth of 12 cm with a significantly higher average count rate of 100 cps. In addition, this result also suggests that using the CZT detector with a commercial multichannel analyser rather than the improvised setup employed in this experiment, this depth estimation method can achieve a maximum detectable

depth greater than 18 cm using less than 25-min per  $x$ - $y$  position scanning time. This improved result is mainly due to the high atomic number of the CZT detector, which enabled the use of photon counts from the photo-peak in the depth estimation. Conversely, the experiment with the EJ-301 scintillator used photon counts from the Compton peak because the caesium-137 gamma spectrum from EJ-301 is limited to the Compton continuum due to the low atomic number of the scintillator. Finally, this result confirms that while photon counts from any part of the spectrum can be used with the model, photon counts from the photo-peak will yield the best results.

#### 5.4.1.1 Effect of scanning time

The estimated depths for different scanning times per  $x$ - $y$  position, namely 15, 20 and 25 min, are shown in Figure 5.4.4a. A gradual, but progressive improvement in the estimated depth at 16 cm and 18 cm can be observed as the scanning time increases (see the points indicated on the graph). This progressive improvement in the estimated depth results in the progressive restoration of the graph to the expected deviation pattern as the scanning time increases. The gradual rate at which the estimates improve with time indicates that this relationship is exponential. This is confirmed by Figure 5.4.4b, which is the graph of the absolute error in the estimate as a function of the count rate for the 20-min scanning time experiment. The decay rate of this graph indicates how quickly the error in the estimated depth decreases as the count rate increases, and it is independent of the scanning time. Furthermore, dividing this decay rate by the density of sand will make it also independent of the material in which the source is buried. This will result in a value that is dependent only on the efficiency of

the instrumentation (i.e. detector and related electronics) used. Therefore, this value can be used as a parameter for evaluating and selecting appropriate instrumentation for field application of this remote depth estimation method.

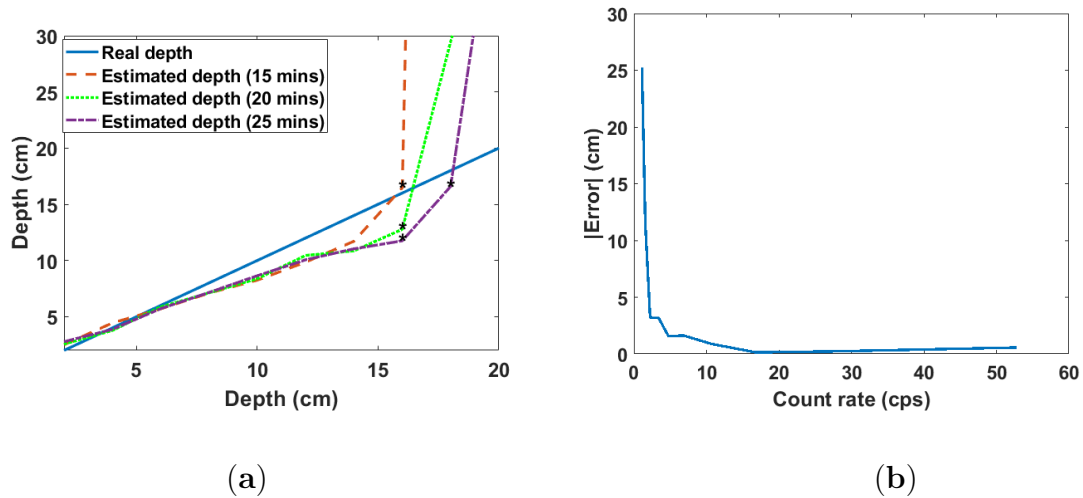


Figure 5.4.4: (a) Estimated depths for three different scanning times.; (b) Exponential decrease of the absolute error in the estimated depth with increasing count rate.

The gradients and intercepts for the linear fit between the real and estimated depths for the three scanning times and those from simulation (reported in [130]) are shown in Table 5.4.1. The “Depths” column in the table refers to the range of depths over which the parameters were estimated. It can be observed that the values of these parameters are relatively constant and do not vary significantly with depth. This means that the values of these parameters can be assumed to be constant for any given material and gamma energy. Therefore, this method can be used to investigate radioactive wastes buried at any depth in a given material without the need for calibration. This is not the case with the empirical model proposed in [123, 124], where new model parameters must be obtained in order to estimate depths

outside the range of depths used to develop the model.

Table 5.4.1: Parameters for the linear fit between the real and estimated depth from experiments and simulation.

	Depths (cm)	Gradient	Intercept
<b>Experiment</b>			
15 min	2–14	$1.4 \pm 0.1$	$-1.6 \pm 0.9$
20 min	2–16	$1.4 \pm 0.1$	$-1.5 \pm 1.2$
25 min	2–18	$1.5 \pm 0.2$	$-2.2 \pm 1.6$
<b>Simulation [130]</b>	2–40	$1.6 \pm 0.1$	$-2.0 \pm 0.6$

### 5.4.2 Results for cobalt-60

The experiment was also carried out using a 9-kBq Co-60 point source. Due to the low activity of the source, the scanning area was reduced to  $20 \times 20 \text{ cm}^2$ , while the scanning time was increased to 40 min per  $x$ - $y$  position. The results for both the 1.77-MeV and 1.33-MeV photo-peaks of the Co-60 gamma spectrum for depths from 1 cm to 4 cm at 1-cm intervals are shown in Figures 5.4.5a,b. The similarity in the estimated depths from both peaks can be observed up to 3 cm, after which both graphs differ dramatically. This is not expected because gamma rays from both energy peaks have similar mass attenuation coefficients, i.e. 0.059 for 1.17-MeV gamma rays and 0.0552 for 1.33-MeV gamma rays. In addition, gamma rays from both energy peaks have the same probability of being emitted from the Co-60 nucleus. Due to these reasons,

estimates after 3 cm were considered to be erroneous and were thus excluded from the linear fit between the real and estimated depths shown in Figure 5.4.5b. This maximum detectable depth of 3 cm achieved for 9-kBq Co-60 source buried in sand is a significant improvement over the technique reported in [120], which achieved a similar maximum depth limit for a 40-kBq Co-60 source also buried in sand. Finally, this result confirms that this method can be used both with other radionuclides and with low level buried wastes.

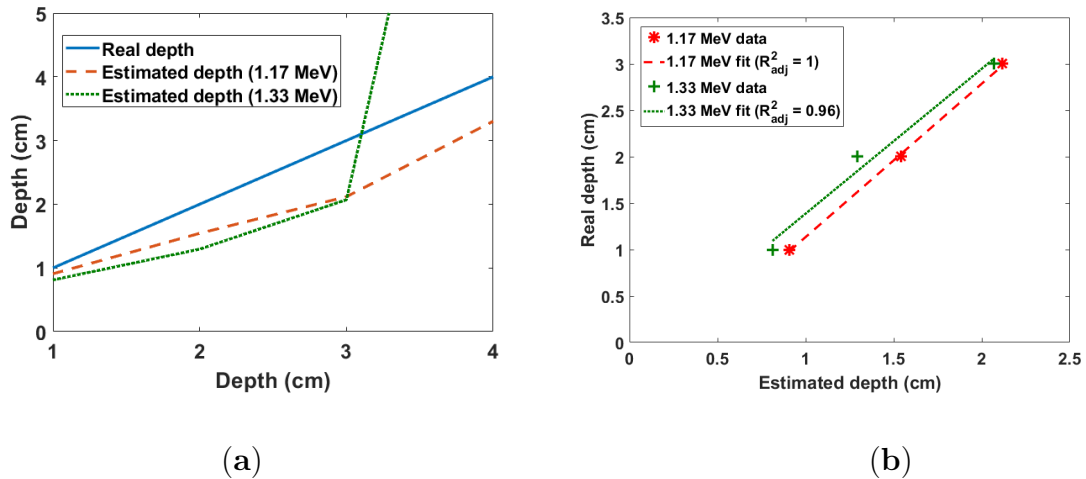


Figure 5.4.5: (a) Real and estimated depths for Co-60 buried in sand.; (b) Linear fit of real and estimated depths for Co-60 buried in sand.

## 5.5 Conclusion

Improvements in the depth estimation results of the approximate 3D attenuation model using a CZT detector have been presented. The results showed that the model was able to non-intrusively estimate the depth of a 329 kBq Cs-137 radioactive source buried up to 18 cm in sand with a significantly lower average count rate of 14 cps

compared to previous results of 12 cm with an average count rate of 100 cps. This will enable the rapid non-intrusive localisation of buried radioactive wastes. Furthermore, the results also confirmed that the depth limit depends on the data acquisition time. Therefore, increasing the data acquisition time will enable the estimation of the depth of wastes buried deeper in the sand. In addition, the result from the experiment using a 9-kBq Co-60 radioactive source confirmed that the model can be used with any gamma radiation source and is also capable of estimating the depth of buried sources with very weak activity. Furthermore, the explicit dependence of the model on the density of the material means that this method can be extended to any material, e.g., concrete, by substituting the material's density in the model. Consequently, the method will find wide application in nuclear decommissioning, land remediation, nuclear security and non-proliferation activities. Finally, areas of further research include investigation of the method's performance using non-point sources and multiple hot spots within the scanning area. These will further improve the robustness of this non-intrusive depth estimation method.

## **5.6 Acknowledgement**

This work was supported by the Engineering and Physical Sciences Research Council (EP/N509231/1) and Nuclear Decommissioning Authority, U.K. The authors would also like to thank Michael Aspinall for his suggestions during the preparation of the manuscript.

## Chapter 6

# Non-intrusive Depth Estimation of Buried Radioactive Wastes Using Ground-Penetrating Radar and a Gamma-Ray Detector

I. K. Ukaegbu, K. A. A. Gamage and M. D. Aspinall

*Remote Sensing*, 11(2):141, 2019. DOI: 10.3390/rs11020141

### 6.1 Abstract

This study reports on the combination of data from a GPR and a gamma-ray detector for non-intrusive depth estimation of buried radioactive sources. The use of GPR was to enable the estimation of the material density required for the calcula-

tion of the depth of the source from the radiation data. Four different models for bulk density estimation were analysed using three materials, namely: sand, gravel and soil. The results showed that the GPR was able to estimate the bulk density of the three materials with an average error of 4.5%. The density estimates were then used together with gamma ray measurements to successfully estimate the depth of a 658 kBq caesium-137 radioactive source buried in each of the three materials investigated. However, a linear correction factor needs to be applied to the depth estimates due to the deviation of the estimated depth from the measured depth as the depth increases. This new application of GPR will further extend the possible fields of application of this ubiquitous geophysical tool.

## 6.2 Introduction

Knowledge of the depth of penetration of radioactive contaminants is critical in characterising and decommissioning porous materials such as soil and concrete. This is because it determines the expected volume of wastes and subsequent choice of retrieval and disposal strategy [10]. This can have significant impact on the decommissioning cost because these materials are usually present in large volumes in contaminated sites [13]. Sources of contamination of this porous materials especially soil include fall out from nuclear weapons testing; nuclear accidents e.g., the Chernobyl and Fukushima accidents; and poor disposal of nuclear wastes [7, 119, 136]. In addition, the presence of these contaminants in the soil constitute a major public hazard due to their long half-life and chemical behaviour. For instance caesium-137 (Cs-137), which is one

of the most predominant anthropogenic radioactive contaminants, is highly soluble and easily taken up by plants as a substitute for potassium thereby contaminating the food chain [15]. Therefore, there is a need to continuously monitor the depth of penetration of these contaminants in suspected sites.

However, traditional methods of depth estimation such as core sampling and logging are slow and have limited spatial sampling extent because of their intrusive nature. Furthermore, the non-intrusive methods reported in [12, 121–124, 136–139] are either based on regression models whose parameters typically have no physical significance or are limited to specific radioactive sources. Also, other non-intrusive methods reported in [140, 141] use specialised shielding and collimator arrangements while those that employ machine learning [19, 142, 143] require significant amount of data to train the algorithms.

Therefore, a new non-intrusive depth estimation method based on an approximate three-dimensional (3D) attenuation model was recently developed [130]. The method is simple to setup and can be used to estimate the depth of any gamma emitting radioactive source. However, the method requires the density of the material in which the radioactive source is buried to be known before it can be used. This is usually not possible in practice without having recourse to intrusive density measurement methods [144]. Furthermore, the use of predefined or historical density values can result in misleading depth estimates because these values do not account for the changes undergone by the material over time due to environmental factors. Hence, there is the need for an in situ density estimation technique that is non-intrusive. GPR has been extensively used for the non-intrusive estimation of the soil moisture

content of materials such as concrete and soil [145–148]. Therefore, it can potentially be used as a complementary sensor to provide this density information to the depth estimation process.

Consequently, this study reports on the combined use of a GPR and a gamma ray detector to estimate the depth of a buried radioactive source. Four different models for the estimation of bulk density from GPR were investigated using three different materials. The results from the best model were then used together with the data from the gamma ray detector to estimate the depth of a Cs-137 radioactive source buried in each of the materials. The rest of this article is divided into four sections. The next section describes the theoretical framework of the research while Section three presents the material and methods adopted for the research. The results and discussions are presented in Sections 6.5 and 6.6 respectively and the conclusion is presented Section 6.7.

## 6.3 Theoretical framework

### 6.3.1 Approximate 3D linear attenuation model

Given a radioactive source  $S$  buried inside a material at depth  $z$  as shown in Figure 6.3.1, the ratio of the intensity  $I_{(x,y,z)}$  measured at any position  $(x, y)$  on the surface of the material to that measured from a reference position (i.e.  $(x, y) = (0, 0)$ ) on the same surface is given by [130]:

$$\log_e(J_{(x,y,z)}) \approx -\frac{\mu_m \rho_b}{2z}(x^2 + y^2) + \log_e(K_{(x,y,0)}) \quad (6.3.1)$$

where  $J_{(x,y,z)} = \frac{I_{(x,y,z)}}{I_{(0,0,z)}}$ ,  $\mu_m$  = mass attenuation coefficient,  $\rho_b$  = bulk density and  $K_{(x,y,0)} = \frac{I_{(x,y,0)}}{I_{(0,0,0)}}$ . Equation (6.3.1) is referred to as the approximate 3D attenuation model and can be used to estimate the depth of a buried gamma radiation source by fitting it to the data of intensities at a given gamma ray energy measured from discrete positions on the surface of the material volume. Both  $\mu_m$  and  $\rho$  are properties of the material in which the source is buried. However, while  $\mu_m$  is known to be relatively constant for different materials for a given photon energy,  $\rho_b$  must be estimated for the material under investigation before the attenuation model can be applied. Therefore, the use of GPR for non-intrusive estimation of  $\rho_b$  is the main aim of this study.

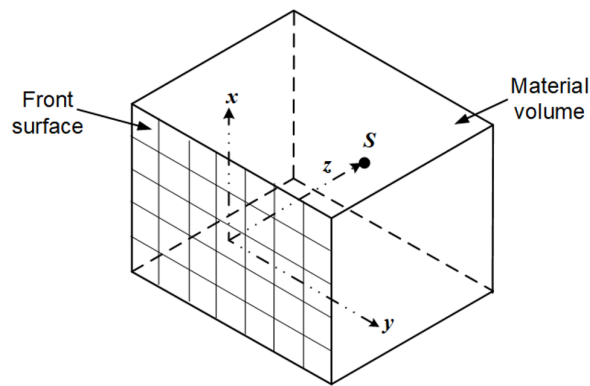


Figure 6.3.1: Radioactive point source  $S$  buried in a material volume.

### 6.3.2 Principles of GPR

GPR is a geophysical technique for non-intrusive investigation of a wide variety of structures and materials e.g., soil, concrete etc. It does this by exploiting the response of these materials to propagating electromagnetic waves as illustrated in Figure 6.3.2. Electromagnetic waves from the transmitting antenna propagates into the surrounding medium at a velocity which is dependent mainly on the permittivity of the medium.

The permittivity is a measure of the resistance offered by a material to the electric field induced by the waves. Furthermore, the measured permittivity of mixtures such as soil and concrete is referred to as the effective or bulk permittivity  $\epsilon_b$ . This is because the measured permittivity of these materials is a combination of the permittivities of their constituents. In addition, the permittivity of a material is typically given as a relative quantity, i.e. the ratio of the material's permittivity to that of free space. Therefore, all use of permittivity in this study refers to its relative value unless otherwise stated.

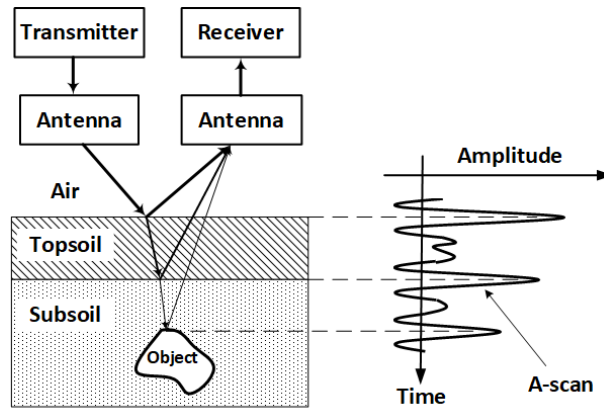


Figure 6.3.2: Principles of GPR. Reflected waves from boundaries are recorded by the receiver and displayed as a time varying signal called an A-scan.

When the propagating waves encounter a boundary or interface, i.e. a layer with a different permittivity, part of the waves is reflected while the remaining is transmitted through the second layer. The proportion of the reflected wave is determined by the layer's reflection coefficient  $R$  which is given by:

$$R = \frac{\sqrt{\epsilon_{b,0}} - \sqrt{\epsilon_{b,1}}}{\sqrt{\epsilon_{b,0}} + \sqrt{\epsilon_{b,1}}} \quad (6.3.2)$$

where the  $\epsilon_{b,0}$  and  $\epsilon_{b,1}$  are the bulk permittivities of the first and second layers respectively. However, it should be noted that total reflection of the waves can occur

if the second layer is a highly conductive material such as metal. The reflected waves are captured by the receiving antenna after which it is digitised by the receiver and displayed as a time varying signal commonly referred to as an A-scan (Figure 6.3.2). Interfaces encountered by the propagating waves are indicated by pulses in the A-scan while the time of arrival of each pulse is an indication of the distance of the interface from the antennas.

### 6.3.3 Bulk density estimation using GPR

The estimation of the bulk density of a material using GPR consists of two steps, namely: Estimation of the material's permittivity, and estimation of the bulk density from the permittivity using permittivity mixing formulas. These steps are further discussed in the following subsections.

#### 6.3.3.1 Estimation of the material's permittivity

If the medium of propagation is considered to be made up of layers with different permittivities, then the relative amplitude of the reflected pulse from the  $n$ th layer is given by [149]:

$$\frac{A_n}{A_{inc}} = \frac{\sqrt{\epsilon_{b,n}} - \sqrt{\epsilon_{b,n+1}}}{\sqrt{\epsilon_{b,n}} + \sqrt{\epsilon_{b,n+1}}} \left[ \prod_{i=0}^{n-1} (1 - R_i^2) \right] e^{-\eta_0 \sum_{i=0}^n \frac{\sigma_i d_i}{\sqrt{\epsilon_{b,i}}}}, \quad (6.3.3)$$

where  $A_n$  is the amplitude of the reflected pulse from the  $n$ th layer,  $\eta_0$  is the free space impedance,  $\sigma_i$  is the layer conductivity,  $d_i$  is the layer thickness, and  $A_{inc}$  is the amplitude of the incident pulse from the GPR system. The value of  $A_{inc}$  is usually obtained by measuring the reflection amplitude due to a flat metal surface placed at a

fixed distance from the GPR system. This is because the metal surface is considered to be perfect electrical conductor with a reflection coefficient of  $-1$ . Therefore, the reflected pulse from the metal surface is the same as the inverse of the incident pulse from the GPR system.

For a two layer medium where the first layer is made up of air which has a permittivity of 1, the permittivity of the second layer can be obtained from Equation (6.3.3) by substituting  $n = 0$ , i.e.

$$\epsilon_{b,1} = \left( \frac{1 + [A_0/A_{inc}]}{1 - [A_0/A_{inc}]} \right)^2 \quad (6.3.4)$$

where  $A_0$  is the reflection amplitude from the interface between the first and second layer. This formula is widely used as the surface reflection method for the estimation of the permittivity and other properties of soils [52, 150] and asphalt pavements [151–153]. Finally, Equation (6.3.3) can be used with a medium with any number of layers by iteratively applying it to all significant pulses in the A-scan to obtain the vertical variation of the medium's permittivity with depth.

### 6.3.3.2 Permittivity mixing formulas

Porous media such as soil and concrete can be considered as a mixture of several materials in different phases. For example, soil is typically modelled as a mixture of solid particles, water and air where the solid particles acts as a background material into which water and air are added as inclusions [154]. Permittivity mixing formulas express the bulk permittivity of these porous media as function of the permittivities of their constituents and the internal structure of the mixture. A number of permittivity

mixing formulas have been proposed in the literature and these can be broadly divided into two categories.

The first category of formulas are those derived from the relationship between the induced electric field and the flux density. Since these category of formulas are derived from the physical laws of electromagnetism, they incorporate the microstructural properties of the mixture albeit with some simplifications. The general expression for this category of formulas is given by [155]:

$$\frac{\epsilon_b - \epsilon_0}{\epsilon_b + 2\epsilon_0 + v(\epsilon_b - \epsilon_0)} = \sum_{i=1}^n f_i \frac{\epsilon_i - \epsilon_0}{\epsilon_i + 2\epsilon_0 + v(\epsilon_b - \epsilon_0)} \quad (6.3.5)$$

where  $\epsilon_0$  is the permittivity of the background material,  $\epsilon_i$  is the permittivity of other constituents of the mixture,  $f_i$  is the volume fraction of each constituent and  $v$  is a positive constant which indicates the effect of the polarisation induced in the medium as a result of the propagating electric field. Furthermore, it was proved in [155] that most of the mixing formulas proposed under this category can be obtained from Equation (6.3.5) by substituting appropriate values for  $v$ . The second category of mixing formulas are the exponential or power law formulas which have the general form:

$$\epsilon_b^\alpha = \sum_{i=1}^n f_i \epsilon_i^\alpha \quad (6.3.6)$$

where  $\alpha$  is a geometric parameter whose value is obtained by fitting the model to experimental data. The common reported values for  $\alpha$  are 0.5 [156–158] and 0.65 [159, 160]. Furthermore, Equation (6.3.6) with  $\alpha = 0.5$  is also referred to as the complex refractive index model (CRIM).

In estimating the density of asphalt pavements using GPR, Leng et al. [152]

used three permittivity mixing formulas namely: Rayleigh [161], Bottcher [162] and CRIM. Therefore, these three models were also adopted for this study. Both the Rayleigh and Bottcher formulas can be derived from Equation (6.3.5) using  $v = 0$  and  $v = 2$  respectively while the CRIM is obtained from Equation (6.3.6) with  $\alpha = 0.5$  as mentioned in the previous paragraph. In addition, Equation (6.3.6) with  $\alpha = 0.65$  was also included in this study and will henceforth be referred to as the Dobson mixing formula.

In summary, for a porous medium consisting of solid particles, air and water, the Rayleigh, Bottcher, CRIM and Dobson mixing formulas for the bulk permittivity are given by:

$$\frac{\epsilon_b - \epsilon_s}{\epsilon_b + 2\epsilon_s} = (\phi - W_c) \frac{\epsilon_a - \epsilon_s}{\epsilon_a + 2\epsilon_s} + W_c \frac{\epsilon_w - \epsilon_s}{\epsilon_w + 2\epsilon_s}, \quad (6.3.7)$$

$$\frac{\epsilon_b - \epsilon_s}{3\epsilon_b} = (\phi - W_c) \frac{\epsilon_a - \epsilon_s}{\epsilon_a + 2\epsilon_b} + W_c \frac{\epsilon_w - \epsilon_s}{\epsilon_w + 2\epsilon_b}, \quad (6.3.8)$$

$$\epsilon_b^{0.5} = (1 - \phi)\epsilon_s^{0.5} + (\phi - W_c)\epsilon_a^{0.5} + W_c\epsilon_w^{0.5}, \quad (6.3.9)$$

$$\epsilon_b^{0.65} = (1 - \phi)\epsilon_s^{0.65} + (\phi - W_c)\epsilon_a^{0.65} + W_c\epsilon_w^{0.65}, \quad (6.3.10)$$

respectively where  $\epsilon_s, \epsilon_w, \epsilon_a$  are the permittivities of solid particles, water and air respectively,  $\theta$  is the water content of the medium and  $\phi$  is the porosity of the medium which is related to the bulk density by:

$$\phi = 1 - \frac{\rho_b - W_c}{\rho_s} \quad (6.3.11)$$

where  $\rho_s$  is the specific density of the solid particles. It should be noted that the volume fractions  $f$  of the air, water and solid particle depend on the porosity and water content of the medium consequently, they were replaced in Equations (6.3.7)–(6.3.10) with their respective expressions from [157].

## 6.4 Materials and methods

The three materials investigated in this study are shown in Table 6.4.1. The bulk densities of each of the material was measured using three different subsamples and the average value recorded. The elemental composition of the sand and soil samples were obtained using Scanning Electron Microscopy while that of the gravel sample was obtained from [125]. Furthermore, the mass attenuation coefficients of all the elements in the three sample were obtained from tables published by the National Institute of Standards [127]. These were then used together with the elemental compositions to calculate the mass attenuation coefficients of the three materials at 662 keV, which is the gamma ray energy at the photo peak of the Cs-137 radioisotope used in this study. It can be observed from Table 6.4.1 that the mass attenuation coefficient is relatively constant for all three materials therefore, an average value of 0.0775 was used in this study. The solid permittivity of soil and sand were obtained from [159], while that of gravel was obtained from [163]. In addition, a specific density of 2.65 g cm<sup>-3</sup> [164] was adopted for all three materials. Finally, both the sand and gravel were dry samples while the water content of the soil was measured using the oven drying method.

Table 6.4.1: Properties of the materials used in the study.

	Sand	10 mm Gravel	Soil
Bulk density ( $\rho_b$ ) ( $\text{g cm}^{-3}$ )	1.52	1.54	1.26
Mass attenuation coefficient ( $\mu_m$ ) at 662 keV	0.0776	0.0775	0.0773
Solid permittivity ( $\epsilon_s$ )	4.7	6.5	4.7
Specific density ( $\rho_s$ ) ( $\text{g cm}^{-3}$ )	2.65	2.65	2.65
Water content ( $W_c$ ) (%)	0.0	0.0	6.0

### 6.4.1 Gamma-ray data acquisition and processing

The experiment setup for the acquisition of the gamma ray intensity data is as shown in Figure 6.4.1. The material volume is represented by a box in which the different materials were placed. The dimension of the box is 40 cm  $\times$  50 cm  $\times$  40 cm (length  $\times$  width  $\times$  height) and it was constructed with acrylic sheets with a thickness of 0.8 cm. Acrylic sheet was used because it is relatively transparent to gamma rays. The front of the box was divided into 4  $\times$  4 cm<sup>2</sup> grids in order to identify each measurement position. The gamma-ray detector used in the experiment was the CZT/500(s) detector from Ritec (Riga, Latvia). This is a cadmium zinc telluride detector which has a sensing volume of 0.5 cm<sup>3</sup> and is sealed in a casing with a diameter of 2.2 cm. Furthermore, the detector was placed inside a hollow cylindrical tungsten shield opened at both ends in order to eliminate background radiation from the laboratory environment.

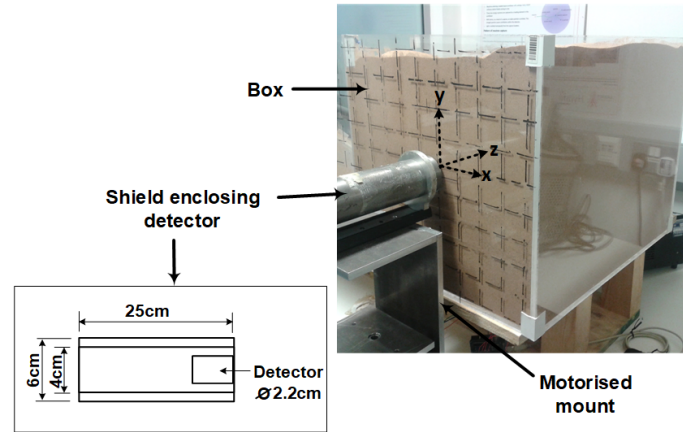


Figure 6.4.1: Setup for the gamma ray measurements. The Cs-137 point source was placed at varying position along the  $z$ -axis using a pipe that protruded behind the box, while the intensity was measured at the desired positions on the surface of the box.

During the experiment, the box was filled with one of the materials and a 658 kBq Cs-137 radioactive point source was buried at varying depths from 2 cm to 22 cm at 4 cm intervals along the  $z$ -axis starting from the origin. This procedure was repeated for each of the materials. At each depth, the pulses from the detector were acquired using an oscilloscope (sampling rate = 500 kSa/s) from the desired number of grids. An acquisition time of 25 min per grid was used throughout the experiment. The acquired pulses were then stored and processed in a personal computer using the pulse height analysis algorithm described in [165] to generate the spectrum of the source at each grid. Therefore, a total of  $n$  spectra was acquired per depth where  $n$  is the number of grids. In addition, the background spectra for each of the three materials were also measured and subtracted from each of the generated spectrum. Finally, the photo peak function described in [135] was used to extract the number of

gamma ray photons (i.e. intensity) at 662 keV from each of the generated spectrum.

### 6.4.2 GPR data acquisition and processing

As mentioned in Subsection 6.3.3, the first step in bulk density estimation using GPR is the estimation of the bulk permittivity using Equation (6.3.4). This will require the measurement of the amplitudes of the reflected pulses from each of the material and that from a metallic surface. The setup for the acquisition of the reflected pulses is shown in Figure 6.4.2. The orientation of the setup was kept the same with that of the gamma ray data acquisition to ensure consistency between the data from both experiments. The GPR system used is the MALA CX12 from GuidelineGeo (Sundbyberg, Sweden) with a central frequency of 1.2 GHz. In addition, a sampling frequency of 37 GHz and time window of 8.4 ns was used throughout the experiment.

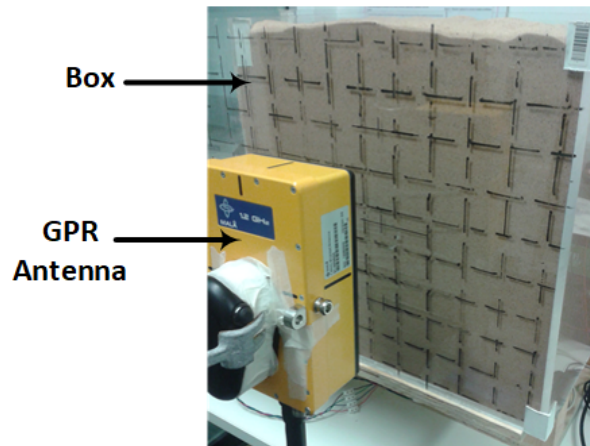


Figure 6.4.2: Setup for the GPR reflected pulse measurements. The antenna was placed 15 cm from the surface of the box.

During the experiment, the GPR antenna was centrally positioned fifteen centimetres (15 cm) away from the front of the box while the reflected pulse was measured.

This was repeated each time the box was filled with a different material. Furthermore, since the bulk permittivity was assumed to be uniform throughout the material volume, all the pulses were measured from this fixed position. In addition, the reflected pulse when the box was empty was also measured and subtracted from the reflected pulses measured when the box was filled with each of the material. This procedure removed the contributions of both the direct wave and box to the measured reflected pulses from the materials. Finally, the reflected pulse from a flat metal sheet was also measured in order to complete the data required to estimate the bulk permittivities of the materials.

After acquisition, the pulses were filtered using a finite impulse response bandpass filter with lower and upper frequencies of 0.5 GHz and 2.5 GHz respectively to remove unwanted frequency components. The filtered pulses from both the soil and metal sheet are shown in Figure 6.4.3a. The amplitude values of the pulses were obtained from the peak of the envelope of the Hilbert transform of the pulses. This is also shown in Figure 6.4.3b for the pulses from the soil and the metal sheet. Having obtained the required amplitude values, the bulk permittivities of the three materials were then estimated using Equation (6.3.4) and are shown in Table 6.4.2. The bulk permittivities of both the sand and gravel are consistent with the values reported in [163, 166], while that of the soil is higher than both materials because of the water content. Also, note that the bulk permittivity of the gravel is higher than that of the sand despite both materials having approximately the same measured bulk densities. This difference is due to the solid permittivity of gravel which is higher than that of sand. Finally, using the estimated bulk permittivities, the bulk densities of each of the materials were then

estimated using the four permittivity mixing formulas, i.e. Equations (6.3.7)–(6.3.11) where the permittivities of water and air were taken to be 80.1 and 1 respectively. These results are presented and discussed in the next section.

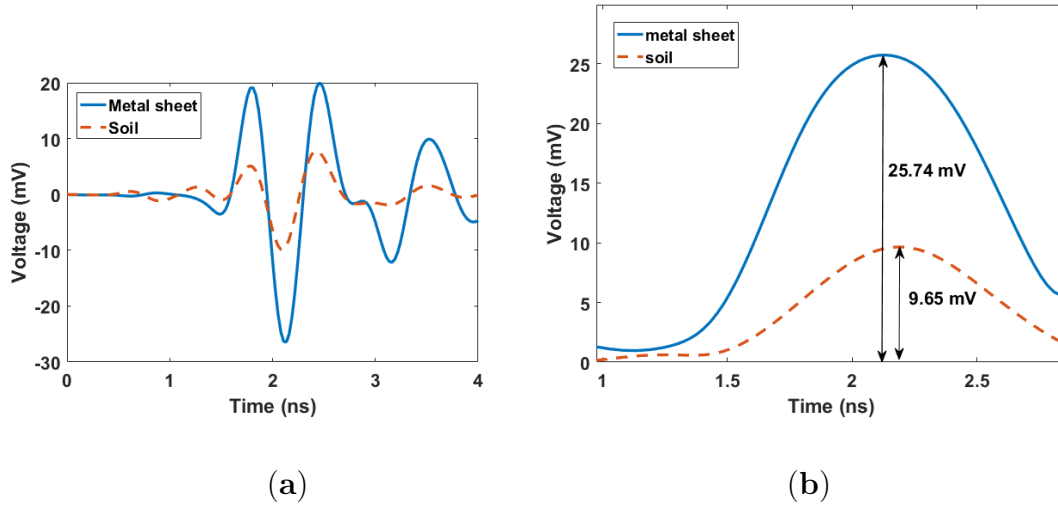


Figure 6.4.3: (a) Measured reflected pulses from the air-soil and air-metal interfaces without time-offset correction. Both pulses can be seen to arrive between 1.4–2.6 ns; (b) Envelope of the Hilbert transform of both pulses.

Table 6.4.2: Estimated bulk permittivity for the three materials using Equation (6.3.4).

	Sand	Gravel	Soil
Bulk permittivity ( $\epsilon_b$ )	2.93	3.57	4.84

## 6.5 Results

### 6.5.1 Bulk density estimation

The error in the estimated bulk densities for the four mixing formulas are shown in Figure 6.5.1. It can be observed that all the formulas yielded reasonably good estimates for both sand and gravel with an average error of 5% and 3.75%, respectively. However, the Rayleigh and Dobson formulas had the best performance for sand with an error of 3% and 2%, respectively. Conversely, the Bottcher and CRIM formulas had the best performance for the gravel with an error of 3% and  $-1\%$  (negative errors means that the bulk density was underestimated). However, the significant difference in the performance of the formulas can be observed in the result for soil where all the formulas except the Dobson formula performed very poorly. The overestimation of the bulk density of soil by over 70% by both the Rayleigh and Bottcher formulas can be attributed to the fact that both formulas assume that the mixture is homogeneous [155] which is relatively true for both the sand and gravel samples. Conversely, soil is typically a complex mixture of sand, clay, silt, water, organic matter and other inorganic minerals consequently, the assumption of homogeneity is not valid.

The very good performance of the Dobson formula for soil compared to the poor performance of the CRIM formula is likely due to the inclusion of the effect of bound water by Dobson et al. [159] in their estimation of the value of  $\alpha$  in Equation (6.3.6). This is because at low water content (as is with the case of the soil used in this study), the water in the soil exists predominantly as bound water [159], i.e. as a thin

film around the solid soil particles. Due to their restricted molecular motion, these bound water have a lower permittivity compared to free water in the pore of the soil matrix [157]. Therefore, the assumption that all the water in the soil behaves as free water (see [158]) which is the basis for arriving at a value of 0.5 for  $\alpha$  is not correct. However, this assumption can be valid at high water content where the behaviour of free water dominates. This was further confirmed by [154] who observed that an  $\alpha$  value of 0.5 seems to be appropriate for fully water-saturated porous media. Finally, since the Dobson formula had the least average error of 4.5% for all materials, its bulk density estimates were used in the subsequent sections to calculate the depth of the buried Cs-137 source.

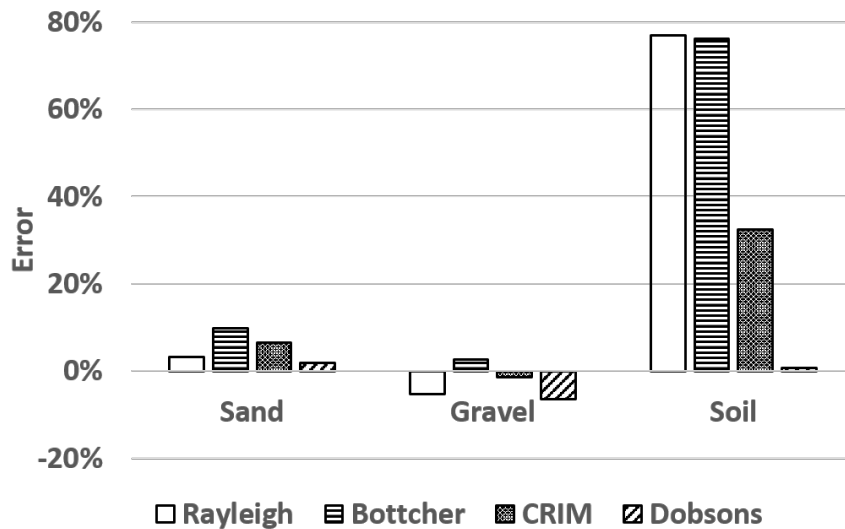


Figure 6.5.1: Error in the estimated bulk densities of the three materials under investigation.

### 6.5.2 Depth estimation of the buried Cs-137 radioisotope

The measured gamma ray intensities when the source was buried at 14 cm in the

three materials are shown in the top row of Figure 6.5.2 as normalised raster images. The intensities were measured from a total of  $7 \times 7$  grids covering a total scan area of  $28 \times 28 \text{ cm}^2$ . Furthermore, each pixel value of the image represents the number of gamma ray photons at 662 keV recorded by the detector at that position. The fitting of the attenuation model (i.e. Equation (6.3.1)) to the data from each of raster images using the density estimates from the Dobson mixing formula are shown in the corresponding bottom row of Figure 6.5.2. A good model fit can be observed for all three materials as indicated by the high adjusted r-squared values.

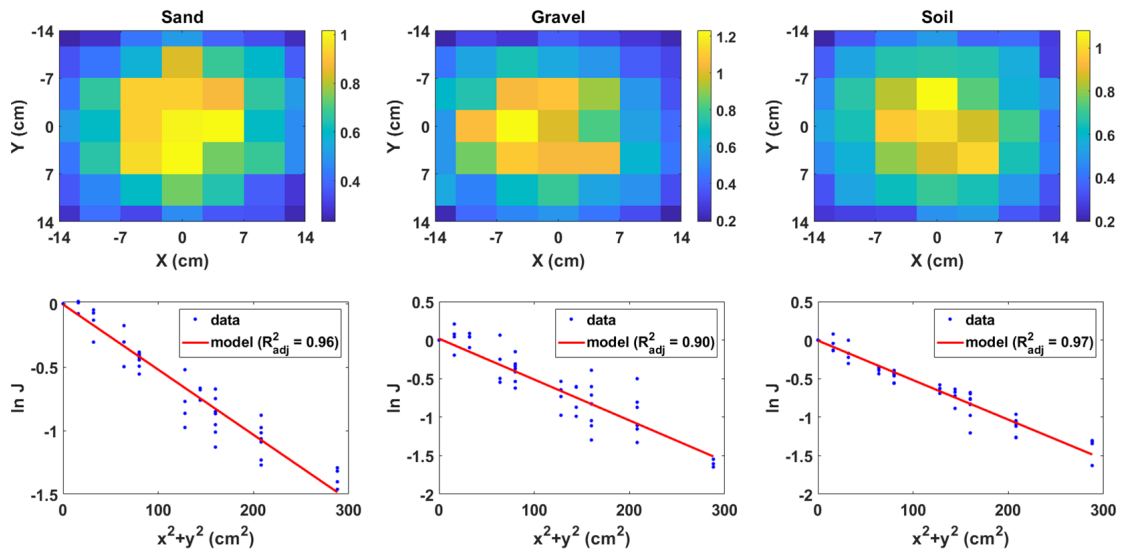


Figure 6.5.2: Normalised raster images of the Cs-137 source buried at a depth of 14 cm for each of the material (top row). Corresponding fit of the attenuation model for each of the depth images (bottom row).

The estimated depths of the buried Cs-137 radioisotope from the fitted attenuation model are shown in Figure 6.5.3 for all three materials. A consistent linear deviation of the estimated depth from the measured depth as the depth increases can be observed

in all three materials. This deviation can be attributed to the fact that the attenuation model does not account for the inverse square reduction in the gamma ray intensity as the depth increases. However, a linear correlation between the estimated and measured depths can be visually observed in the figure for all three materials. This means that the measured depth can be predicted from the estimated depth by fitting a linear polynomial to the scatter graph. The fitted linear polynomials for the three materials are given in Table 6.5.1. The high adjusted r-squared values is indicative of the good linear correlation between the estimated and measured depths. Finally, it was shown in [165] that the parameters of these linear polynomials i.e., the gradient and intercept can be obtained using simulation tools such as MCNPX[114] and then used to correct estimated depths measured from field data.

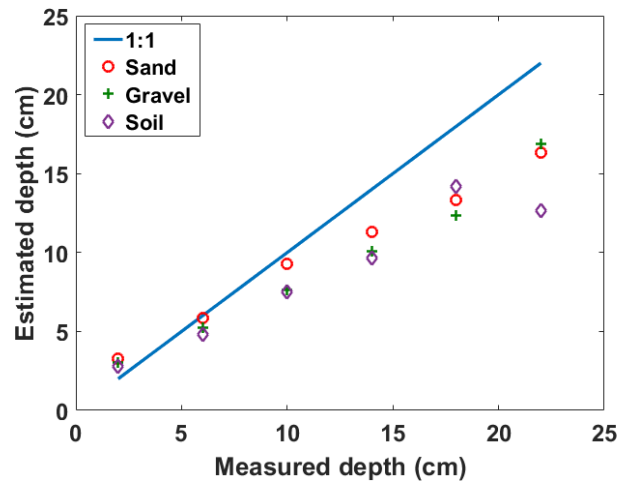


Figure 6.5.3: Estimated depths of the buried Cs-137 source for the three materials.

Table 6.5.1: Linear polynomials fitted to the scatter graph of Figure 6.5.3 where  $z_{est}$  is the estimated depth and  $z_{mea}$  is the measured depth. This can be used as calibration equations to correct for the deviation of the estimated depth from the measured depth.

Material	$y = ax + b$	$\pm error$	$R_{adj}^2$
Sand	$z_{est} = 0.64z_{mea} + 2.2$	$\pm 1.1$	0.99
Gravel	$z_{est} = 0.63z_{mea} + 1.9$	$\pm 1.2$	0.99
Soil	$z_{est} = 0.59z_{mea} + 1.5$	$\pm 1.9$	0.95

## 6.6 Discussion

The results presented in the previous section has proven the potential of GPR as a tool for estimating the material bulk density required for non-intrusive estimation of the depth of buried radioactive sources. This in situ density estimation will improve the accuracy in determining the depth of penetration of radioactive contaminants in materials such as soil and concrete compared to the use of historical density values. Furthermore, the non-intrusive nature of GPR will ensure that the contaminated material subsurface is not disturbed thereby preventing further spreading of the contamination.

However, one of the potential challenges in applying this depth estimation technique in the field is the time required to move a single gamma detector across the scan area. This can be eliminated by using a square array of gamma detectors since each detector and its shielding covers only a relatively small area of  $4 \times 4 \text{ cm}^2$ . The

detector array can then be mounted on a trolley to scan the ground surface of the contaminated area. It should also be noted that the 25 min per grid measurement time taken to measure the gamma rays is due to the fact that each signal from the detector was first digitised by an oscilloscope and then transferred to a computer for processing. This time will be substantially reduced by using commercial multichannel analysers. These are dedicated high-speed electronics that process the output from a gamma detector and generate the spectrum of the radioactive source in real-time.

Another difficulty that maybe encountered in the field is the fact that Equation (6.3.4) depends only on the change in permittivity at the air-material interface. Consequently, it is unable to measure the vertical variation in the bulk permittivity inside the material which can occur when investigating at greater depths, e.g., up to 1 m. This difficulty can be resolved by iteratively applying Equation (6.3.3) to every significant pulse identified in the measure A-scan. This will yield the vertical variation of the permittivity inside the material from which the variation in density can be obtained using the Dobson mixing formula.

## 6.7 Conclusion

The use of GPR as a complementary sensor to provide in situ material density data required for the non-intrusive estimation of the depth of buried radioactive sources from radiation data has been demonstrated using three different materials. The results showed that the Dobson permittivity mixing formula provided the best bulk density estimates across the range of materials investigated. Therefore, its results were used

with the radiation data to estimate the depth of a buried Cs-137 source using an approximate 3D attenuation model. However, a linear correction factor needs to be applied to the depth estimates to account for deviation of the estimated depth from the measured depth as the depth increases. This limitation will be further investigated in order to make the attenuation model more robust.

Finally, the benefits of combining GPR and radiation detectors are not limited to material density estimation. It also opens the possibility of non-intrusive three dimensional reconstruction of the contaminated subsurface by fusing GPR and radiation images. This will enhance visual monitoring of these type of contaminated environments and provide guidance for autonomous decommissioning systems.

## **6.8 Acknowledgement**

The authors would like to thank Douglas Offin (National Nuclear Laboratory, UK) for industrial supervision of the project and Richard Wilbraham (Engineering department, Lancaster University, UK) for assistance with the scanning electron microscopy measurements.

## Chapter 7

# Integration of Ground-Penetrating Radar and Gamma-Ray Detectors for Non-intrusive Characterisation of Buried Radioactive Objects

I. K. Ukaegbu, K. A. A. Gamage and M. D. Aspinall

*Sensors*, 19(12):2743, 2019. DOI: 10.3390/s19122743

### 7.1 Abstract

The characterisation of buried radioactive wastes is challenging because they are not readily accessible. Therefore, this study reports on the development of a method for integrating GPR and gamma-ray detector measurements for non-intrusive characteri-

sation of buried radioactive objects. The method makes use of the density relationship between soil permittivity models and the flux measured by gamma-ray detectors to estimate the soil density, depth and radius of a disk-shaped buried radioactive object simultaneously. The method was validated using numerical simulations with experimentally-validated gamma-ray detector and GPR antenna models. The results showed that the method can simultaneously retrieve the soil density, depth and radius of disk-shaped radioactive objects buried in soil of varying conditions with a relative error of less than 10%. This result will enable the development of an integrated GPR and gamma-ray detector tool for rapid characterisation of buried radioactive objects encountered during monitoring and decontamination of nuclear sites and facilities.

## 7.2 Introduction

The presence of radioactive objects in the shallow subsurface is a major public health risk because these objects can induce high levels of radiation above the ground. For example, a cobalt-60 source found buried at a depth of about 32 cm in a Cambodian hospital induced radiation levels of up to  $60 \text{ mSv h}^{-1}$  above the ground [7]. This is about 26,000-times the stipulated effective dose limit of 20 mSv per year [14]. Furthermore, chemical reactions in the soil can lead to the dissolution of these objects and subsequent contamination of groundwater. For example, the high energy penetrators used in ammunition are usually made from depleted uranium, which is a by-product of the nuclear fuel enrichment process. Many of these penetrators get lodged in the ground during military operations and become potential sources of groundwater con-

tamination because of their high solubility in sand and other volcanic rock [167]. Therefore, it is important to promptly detect, and safely dispose these objects.

The first stage in the disposal of these buried radioactive objects is their characterisation. However, this process is challenging because of the difficulty in estimating the depth of these objects using traditional intrusive methods such as logging and core sampling [19, 20]. Therefore, a number of non-intrusive depth estimation methods have been developed. These can be broadly divided into three categories, namely: empirical model methods; multiple photo peak methods; and shielding and collimator methods. The empirical model methods are based on establishing correlations between distinguishable features in part or all of the gamma spectrum and the depth of the buried radioisotope. They include: peak-to-valley ratio [136, 139], peak-to-scatter ratio [121, 138], principal component analysis [122–124], and machine learning [19, 142, 143] methods. However, these methods result in models whose parameters typically have no physical significance. Furthermore, the use of machine learning requires a significant amount of data for training. The multiple photo peak methods [12, 120, 137] exploit the difference in the attenuation of two energy peaks in the gamma spectrum in order to estimate the depth of the source. Consequently, they are limited to radioisotopes with two or more photo peaks that are sufficiently separated in the gamma spectrum.

The shielding and collimator methods [140, 141, 168] use different shielding and collimator configurations to obtain multiple measurements from which the depth of the radioactive source can be estimated. These methods have been shown to yield more accurate results compared to other methods [168] and can be used with any

radioisotope. However, the required multiple measurements can only be acquired sequentially. This can significantly increase the data acquisition time because the acquisition of the spectrum of a buried source usually requires a long dwell time due to significant attenuation. In addition, in order to limit the minimum number of measurements required to estimate the depth to only two, the value of the bulk density of the soil is typically assumed to be known. However, the bulk density of soil depends on the current condition of the soil, and this varies from one location to another. Therefore, assuming a constant or generic value will result in errors in the estimated quantities. Furthermore, the use of historical values will not account for the changes in the soil density that would have occurred over time due to environmental factors such as rain fall and temperature changes.

Therefore, this work presents the development of a method for integrating gamma-ray detectors and GPR for the retrieval of the soil density, depth and radius of a buried radioactive object. This eliminates the need for the soil density value to be known a priori. The method also used two horizontally-separated detectors to enable simultaneous acquisition of the required measurements, thereby solving the problem of sequential data acquisition. This will improve the rapid characterisation of buried radioactive wastes.

### 7.3 Theoretical framework

For a radioactive point source buried in an air-soil half-space as shown in Figure 7.3.1, the flux  $F_p$  measured by the detector placed above the ground is given by [169]:

$$F_p = \frac{S_p A_r(\mathcal{E}, \theta) C_e(\mathcal{E})}{4\pi \left(\frac{h+d}{\cos \theta}\right)^2} e^{-\mu_m(\mathcal{E})\rho_a \frac{h}{\cos \theta}} e^{-\mu_m(\mathcal{E})\rho_b \frac{d}{\cos \theta}} \quad (7.3.1)$$

where  $\mathcal{E}$  is the energy of the point source (eV),  $\theta$  is the angle of incidence of the source with the detector (radians),  $d$  is the depth of the source in the soil (cm),  $S_p$  is the activity of the source (Bq) and  $A_r(\mathcal{E}, \theta)$  is the angular response of the detector to a point source of energy  $E$  incident at angle  $\theta$ . This is a dimensionless quantity and is obtained by measuring the response of the detector to a point source at angles varying from  $0-\pi/2$ . This calibration should be done with the collimator in place if the detector is to be used with a collimator.  $C_e(\mathcal{E})$  is the detector's centreline efficiency (cps cm<sup>2</sup> Bq<sup>-1</sup>) and is calculated from the flux due to a source of known activity placed at a known distance  $z$  along the centreline, i.e.

$$C_e = \frac{F_p 4\pi z^2}{S_p} \quad (7.3.2)$$

$\mu_m$  is the mass attenuation coefficient of the point source at energy  $E$  (cm<sup>2</sup> g<sup>-1</sup>),  $\rho_a$  is the density of air (g cm<sup>-3</sup>),  $h$  is the distance from the ground surface to the centre of the detector and  $\rho_b$  is the bulk density of soil (g cm<sup>-3</sup>).

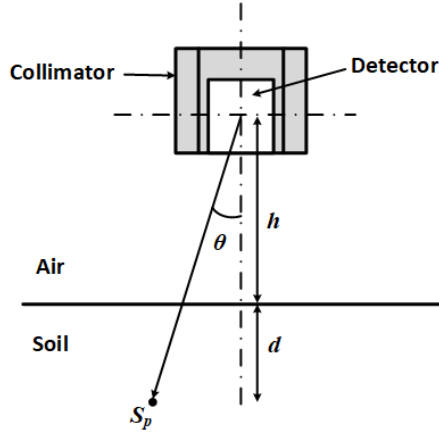


Figure 7.3.1: Geometry and parameters for estimating the flux (measured by the detector) due to the point source  $S_p$  in the soil.

If the buried object is assumed to be disk-shaped and the contamination is at most 1–2 mm below the object's surface, then it can be approximated as a planar disk source, and the flux  $F_a$  measured by the detector is obtained by integrating Equation (7.3.1) over the area of the disk, i.e.

$$F_a = \int_0^{2\pi} \int_0^r \frac{S_a A_r(\mathcal{E}, \theta) C_e(\mathcal{E})}{4\pi \left(\frac{h+d}{\cos\theta}\right)^2} e^{-\mu_m(\mathcal{E})\rho_a \frac{h}{\cos\theta}} e^{-\mu_m(\mathcal{E})\rho_b \frac{d}{\cos\theta}} r \, dr d\varphi \quad (7.3.3)$$

where  $r$  and  $\varphi$  are the radius (cm) and angle (radians) of the disk source in polar coordinates and  $S_a$  is activity per unit area ( $\text{Bq cm}^{-2}$ ).

In most buried radioactive source surveys, the quantities of interest are the activity and depth of the source of the radiation; both of which are estimated from the ratio of two measurements [141]. In other words, the ratio of two measured fluxes  $F_1$  and  $F_2$  acquired using different detector configurations is a function that depends only on the source depth, i.e.

$$\frac{F_2}{F_1} = \text{ratio}(d) \quad (7.3.4)$$

The depth estimated from Equation (7.3.4) can then be used to estimate the source activity using Equation (7.3.1) or (7.3.3) for a point or planar source. However, this two-measurement procedure assumes that the bulk density of the soil is known. This requirement can be eliminated by acquiring a third measurement [141]; however, this will increase the data acquisition time.

GPR has the potential of solving this density-dependency dilemma. A GPR system operates by sending electromagnetic signals into the ground and measuring any portion of the signal that is reflected by interfaces or objects in the signal propagation path. Using the illustration in Figure 7.3.2, the time  $t$  between the reception of the reflection from the ground and that from the disk source is given by:

$$t = \frac{2d}{v} = \frac{2d}{\frac{c}{\sqrt{\epsilon_b}}} \quad (7.3.5)$$

where  $v$  is the speed of the signal in the soil ( $\text{m s}^{-1}$ ),  $c$  is the speed of light ( $299,792,458 \text{ m s}^{-1}$ ) and  $\epsilon_b$  is the relative bulk permittivity of the soil (unitless). It should be noted that Equation (7.3.5) assumes that both the transmitting (Tx) and receiving (Rx) antennas are close to each other.

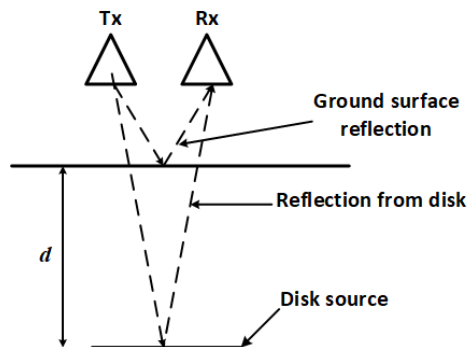


Figure 7.3.2: Operation of a GPR system. Signals from the transmitter (Tx) are reflected by objects and detected by the receiver (Rx).

Porous materials such as soil can be considered as a three-phase mixture of air, water and solid particles [154]. Therefore, their bulk permittivity is a function of the permittivities of these phases and their proportional composition in the material. Various formulas have been proposed to express this relationship; however, in a comparative study [170], it was shown that the formula based on the exponential mixing rule [154] with the exponent value of 0.65 gave the best result across a variety of materials. This formula is given by:

$$\epsilon_b^{0.65} = \left( \frac{\rho_b - W_c}{\rho_s} \right) \epsilon_s^{0.65} + \left( 1 - \frac{\rho_b - W_c}{\rho_s} - W_c \right) \epsilon_a^{0.65} + W_c \epsilon_w^{0.65} \quad (7.3.6)$$

where the exponent value of 0.65 was obtained from the work of Dobson et al. [159],  $\rho_s = 2.65 \text{ g cm}^{-3}$  is the solid particle density for soils,  $W_c$  is the volumetric water content (%),  $\epsilon_s = 4.7$  is the solid particle relative permittivity for soils [159, 160],  $\epsilon_a = 1$  is the relative permittivity of air and  $\epsilon_w$  is the relative permittivity of water, which is given by the real part of the modified Debye's equation [160], i.e.

$$\epsilon_w = \epsilon_{w,\infty} + \frac{\epsilon_{w,0} - \epsilon_{w,\infty}}{1 + (2\pi f \tau_w)^2} \quad (7.3.7)$$

where  $\epsilon_{w,\infty} = 4.9$  is the relative permittivity of water at infinity,  $\epsilon_{w,0}$  is the static relative permittivity of water,  $f$  is the frequency of the GPR (Hz) and  $\tau_w$  is the water relaxation time (s). Both  $\epsilon_{w,0}$  and  $\tau_w$  depend on temperature  $T$  ( $^{\circ}\text{C}$ ) and are given by Equations (7.3.8) and (7.3.9), respectively [171, 172].

$$\epsilon_{w,0} = 88.045 - 0.4147 \times T + 6.295 \times 10^{-4} \times T^2 + 1.075 \times 10^{-5} \times T^3 \quad (7.3.8)$$

$$\tau_w = \frac{1}{2\pi} (1.1109 \times 10^{-10} - 3.824 \times 10^{-12} \times T + 6.938 \times 10^{-14} \times T^2 - 5.096 \times 10^{-16} \times T^3) \quad (7.3.9)$$

Combining Equations (7.3.5) and (7.3.6) will yield Equation (7.3.10), which can be solved simultaneously with Equation (7.3.4) to estimate both the soil bulk density and the depth of the source. This integration of the data from the GPR and gamma-ray detectors can be considered as a type of low-level multi-sensor data fusion where data from different sensors are combined using physical models to enable or improve the estimation of physical parameters [129].

$$\left(\frac{2d}{ct}\right)^{1.3} = \left(\frac{\rho_b - W_c}{\rho_s}\right) \epsilon_s^{0.65} + \left(1 - \frac{\rho_b - W_c}{\rho_s} - W_c\right) \epsilon_a^{0.65} + W_c \epsilon_w^{0.65} \quad (7.3.10)$$

Another important consideration is how to arrange the sensors (i.e. the gamma-ray detectors and GPR antenna) for efficient data acquisition. Preferably, the arrangement should be such that the sensors can operate simultaneously. Two ways of positioning two gamma-ray detectors for the measurement of the radiation fluxes are illustrated in Figure 7.3.3. In the first arrangement, both detectors are vertically displaced by a fixed distance. However, this configuration makes it difficult to simultaneously measure the fluxes from both detectors because the field of view of the upper detector is completely or significantly occluded by the lower detector for small objects. This problem does not occur in the second arrangement where the second detector is horizontally displaced from the reference detector. This arrangement also has the additional advantage of allowing the GPR antenna to be mounted between both gamma-ray detectors thereby creating a more compact sensor arrangement. However, the calculation of the angle of incidence ( $\theta$  in Equation (7.3.3)) for the second detector needs to be modified to account for the horizontal separation.

The modified expression is given by:

$$\theta = \arctan \left( \frac{a}{h+d} \right)$$

$$\text{where } a = \sqrt{(x+r \cos \varphi)^2 + (r \sin \varphi)^2} \quad (7.3.11)$$

and  $x$  is the horizontal separation.

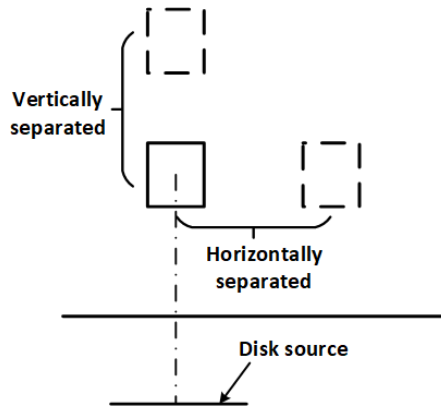


Figure 7.3.3: Two ways of arranging two detectors to measure the flux from the disk source. The horizontally-separated arrangement allows both fluxes to be measured simultaneously because none of the detectors is obstructed.

## 7.4 Materials and methods

The numerical modelling and simulation tools used were Monte Carlo N-Particle Version 5 (MCNP5) [114] and gprMax Version 3.1.4 [115]. MCNP5 is a collection of software codes that is used to simulate the transportation of subatomic particles, e.g., gammas, neutrons, etc., and their interaction with materials using Monte Carlo statistical techniques. It is widely used in the modelling and analysis of nuclear radiation structures and systems and has been extensively proven to have good agreement

with experimental results. `gprMax` is an open source software code used to simulate the propagation of GPR signals. At its core, `gprMax` is a finite-difference time-domain electromagnetic wave solver that uses Yee's algorithm to solve the three-dimensional Maxwell's equations. Its results have also been extensively validated with experiments [173].

### 7.4.1 Selection and modelling of sensors

The gamma-ray detector used in the study was the CZT/500S from Ritec (Riga, Latvia). It is a hemispherical CZT semiconductor detector with a sensitive volume of  $0.5 \text{ cm}^3$  (Figure 7.4.1a). The detector was chosen because of its size and good spectroscopic properties. In addition, unlike HPGe detectors, CZT detectors do not require a cooling system; therefore, they are very portable and easy to integrate with other systems. Figure 7.4.1b shows the simulated and experimental Cs-137 spectrum from the model and real detectors, respectively. A very good alignment of the spectrum key features can be observed. The tailing effect in the Compton valley of the spectrum from the experiment was due to incomplete charge collection caused by poor electron-hole mobility. This is a characteristic feature of CZT detectors. This feature was not modelled because of the additional complexity required. However, this will not affect the results of the study because the ratio of the area under the photo peak for two simulated spectra will be the same as that for two experimental spectra. The difference in the position of the Compton peak was likely due to nonlinearity in the real detector, while the higher background below 300 keV in the spectrum from the experiment can be attributed to backscatter from surrounding objects.

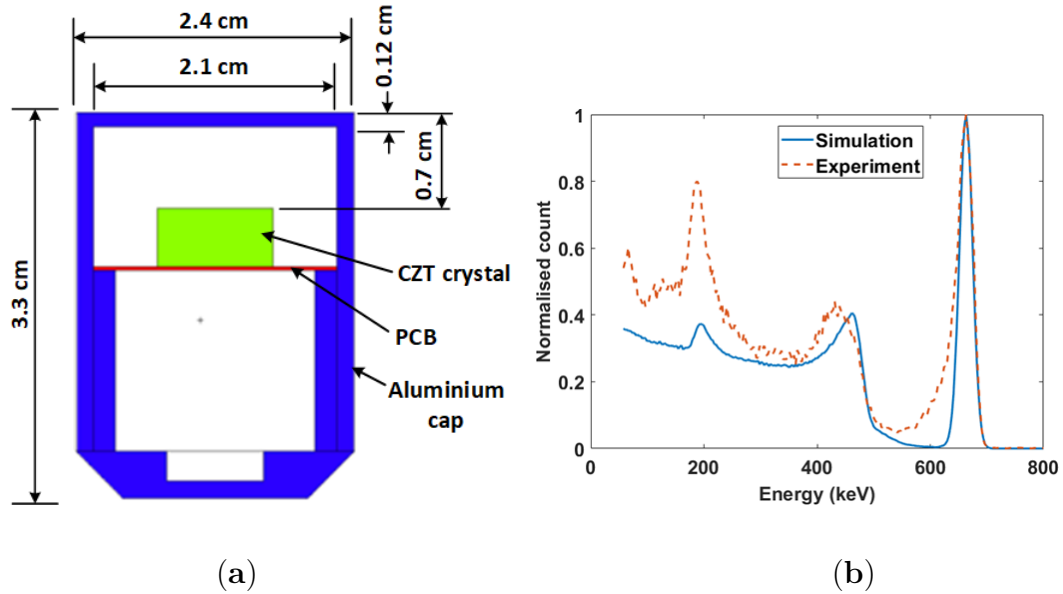


Figure 7.4.1: (a) MCNP5 model of the gamma-ray detector. The crystal volume is  $1 \text{ cm} \times 1 \text{ cm} \times 0.5 \text{ cm}$ ; (b) Experimental and simulated Cs-137 spectrum from the model and real detector.

The selected GPR antenna for the study was the 1.5-GHz antenna (Model 5100) from GSSI Inc. (Nashua, NH, USA). The gprMax model of this antenna is shown in Figure 7.4.2. The antenna consists of a pair of transmitter and receiver bow-tie antennas printed on a circuit board. The antennas are surrounded by microwave absorbers, which in turn are surrounded by a metallic shield. The entire assembly is enclosed in a polypropylene case. The development and experimental validation of the model can be found in [60, 173]. It should be noted that the actual centre frequency of the antenna model was 1.71 GHz with a fractional bandwidth of 103%.

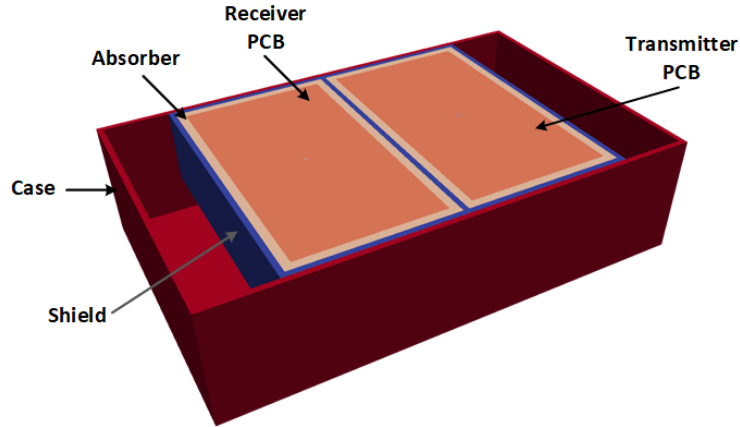


Figure 7.4.2: gprMax model of the 1.5-GHz antenna from GSSI Inc. The antenna dimensions are 17 cm  $\times$  10.8 cm  $\times$  4.3 cm (L $\times$ W $\times$ H). The skid plate underneath the casing has been removed to show the inside of the antenna.

### 7.4.2 Measurement scenario modelling

The measurement scenario was modelled both in MCNP5 and gprMax. The MCNP5 model of the measurement scenario is shown in Figure 7.4.3a. The radioactive object was modelled as a planar disk source with uniform activity. This is typical of stainless steel objects whose surfaces become activated by neutron flux in nuclear reactors [174]. The radioisotope used was Cs-137 with a photo peak energy of 662 keV. Each gamma-ray detector was placed in a cylindrical collimator with inner radius, thickness and height of 2.4 cm, 1.0 cm and 3.3 cm, respectively. The collimator was modelled as an alloy of tungsten (95% W, 3.5% Ni and 1.5% Fe) with a density of 18 g cm<sup>-3</sup> [175]. The horizontal distance between the gamma-ray detectors was selected such that it can fit the width of the GPR antenna. The antenna was modelled as a propylene box since it was not an active component in the MCNP5 simulation. The soil used in the

model was a typical soil (51.4% O, 0.6% Na, 1.3% Mg, 6.8% Al, 27% Si, 1.4% K, 5.1% Ca, 0.5% Ti, 0.07% Mn and 5.6% Fe) with a dry density of  $1.52 \text{ g cm}^{-3}$  [125].

The gprMax model of the measurement scenario is shown in Figure 7.4.3b. This is a replication of the MCNP5 model using the gprMax antenna model described in Section 7.4.1. The detectors were modelled as metallic cylinders since only the lead collimator part of the gamma-ray detectors will affect the GPR signals. The radioactive object was modelled as a metallic disk of thickness 0.5 cm. The two properties required to replicate the soil in gprMax were the bulk permittivity and the bulk conductivity. The bulk permittivity was calculated using Equations (7.3.6)–(7.3.9) at a temperature of 20 °C. The bulk conductivity was calculated using [176]:

$$\sigma_b = \frac{\sigma_w(\epsilon_b - 4.1)}{\epsilon_w} \quad (7.4.1)$$

where  $\sigma_b$  is the soil bulk conductivity ( $\text{Sm}^{-1}$ ) and  $\sigma_w$  is the conductivity of pore water ( $0.05 \text{ Sm}^{-1}$  [177]).

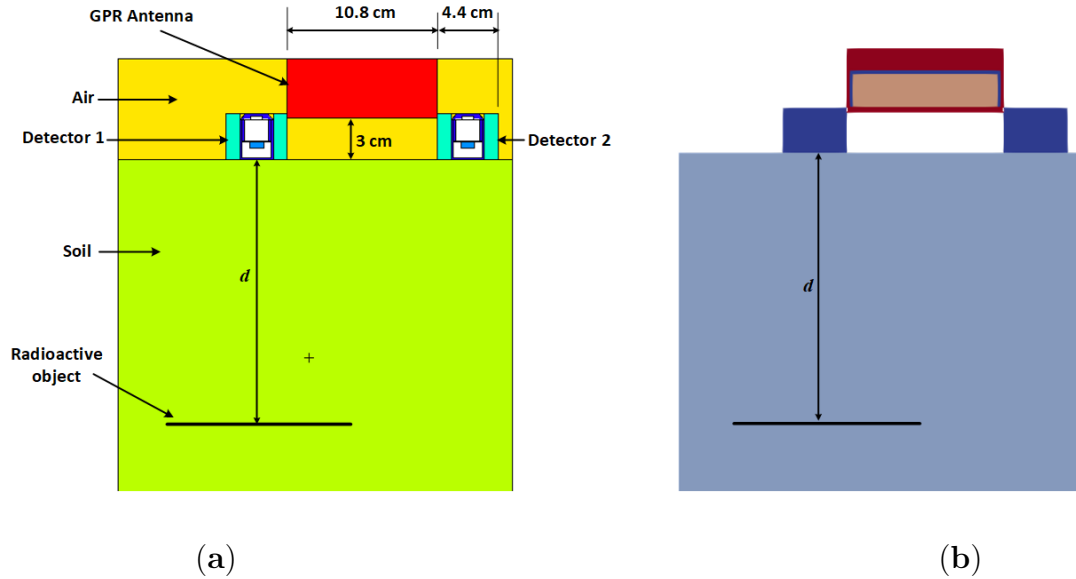


Figure 7.4.3: Model of the measurement scenario. The radioactive object is a metallic disk with Cs-137 radioactive contamination. (a) MCNP5 model of the measurement scenario. The gamma-ray detectors are surrounded by 1 cm-thick lead collimators with an inner radius of 2.4 cm and height of 3.3 cm; (b) gprMax model of the measurement scenario. All labels and dimensions are the same as (a).

### 7.4.3 Simulation and data processing

Two sets of simulations were performed: MCNP5 simulations to measure the gamma fluxes due to the buried radioactive object and gprMax simulations to measure the time of flight (signal travel time) of the GPR signal to the buried radioactive object.

In the MCNP5 simulations, disk sources of radii of 3 cm, 9 cm and 15 cm were separately buried in the soil at depths varying from 12 cm–28 cm at 4-cm intervals. All the activities of the sources were normalised to  $1 \text{ Bq cm}^{-2}$ , unless otherwise stated. After simulation, a Gaussian function was fitted to the spectra from the gamma-ray

detectors in order to estimate the number of full energy photons detected. This is the required flux due to the buried radioactive object. The energy range used for the estimation was from 655–672 keV.

In the gprMax simulations, the radioactive object was also buried in the soil at depths varying from 12 cm–28 cm at 4-cm intervals. The GPR signal was then transmitted and the reflected signals recorded for processing. The first step in processing the GPR data was the subtraction of the antenna’s system response from that acquired from the measurement scenario. The antenna’s systems response is the measured response when the antenna is in air or free space. This subtraction process decoupled the reflection due to the ground surface from the direct signal from the transmitter to the receiver. This made the reflected signal from the ground surface to be easily identified. The required signal travel time was then the time between the ground reflection and the reflection due to the metallic disk. This process is illustrated in Figure 7.4.4a,b. Using the estimated gamma fluxes and the signal travel times, Equations (7.3.4) and (7.3.10) were simultaneously solved to obtain the soil density, depth and radius of the buried radioactive object. These results are presented and discussed in the following section.

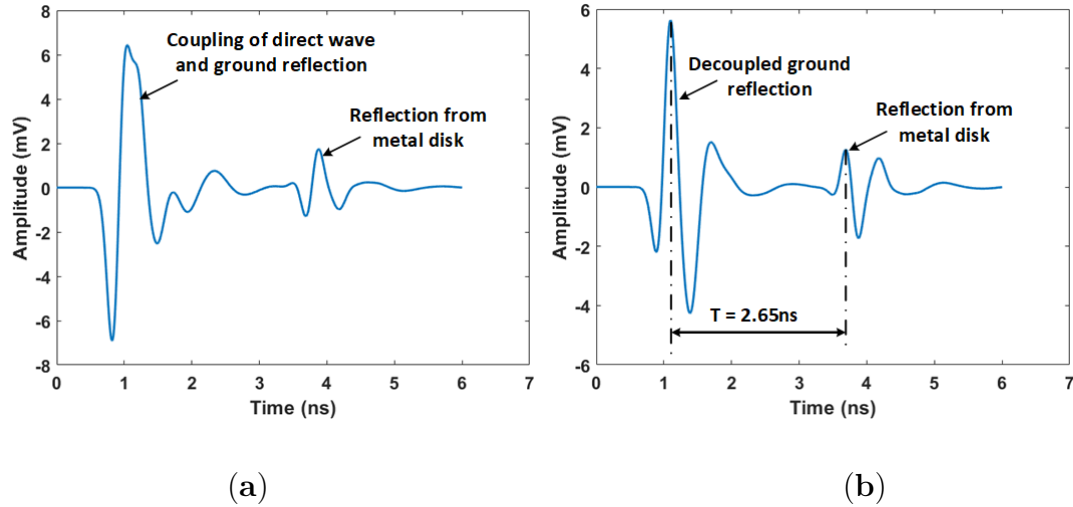


Figure 7.4.4: GPR signal for metal disk of a radius of 3 cm buried at 24 cm in dry soil, (a) Raw GPR signal with coupled direct wave and ground reflection; (b) GPR signal after subtraction of the GPR antenna's system response.

## 7.5 Results and discussion

The calculated (solid lines) and simulated (markers) ratios of the fluxes (i.e. Equation (7.3.4)) from the gamma-ray detectors for disk sources of different radii buried at different depths in the dry soil are shown in Figure 7.5.1. The uncertainty in the flux ratio was calculated using Equation (7.5.1), where  $\delta F_1$  and  $\delta F_2$  are the uncertainties in the fluxes from Detectors 1 and 2 as calculated by MCNP5. A decreasing dependency of the ratios on depth can be observed as the depth increased. This is indicated by the plateauing of the curves and the increasing error bars as the depth increased. This is caused by the exponential attenuation of the gamma rays as the depth of the source increased. This effect can be mitigated in practice by increasing the measurement time or by using a detector with higher efficiency. A decrease in the dependency

of the ratios on depth can also be observed as the source radius increases. This is because the part of the source in the field of view of Detector 2 increases as its radius increases. Therefore, its measured flux will become increasingly the same as that measured by Detector 1 since the source has uniform activity.

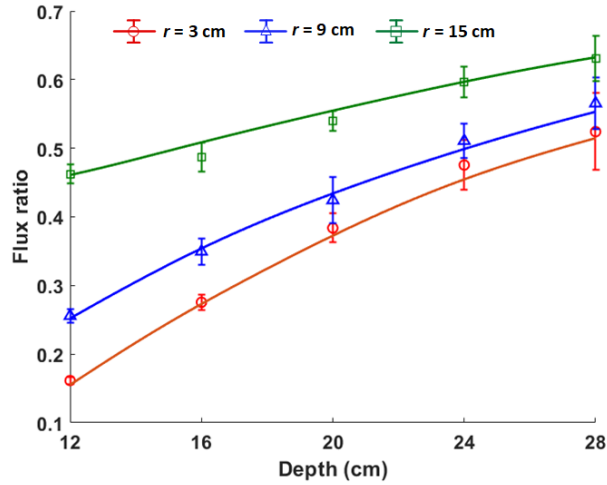


Figure 7.5.1: Flux ratio (i.e.  $F_2/F_1$ ) for sources of radii of 3 cm, 9 cm and 15 cm buried at various depths in dry soil ( $\rho_b = 1.52 \text{ g cm}^{-3}$ ). The solid lines are calculated values, while the markers are the values from the simulation.

$$\text{Flux ratio uncertainty} = \left| \frac{F_2}{F_1} \right| \sqrt{\left( \frac{\delta F_2}{F_2} \right)^2 + \left( \frac{\delta F_1}{F_1} \right)^2} \quad (7.5.1)$$

The depths and densities obtained by simultaneously solving Equations (7.3.4) and (7.3.10) using the flux ratios in Figure 7.5.1 and the signal travel time from GPR measurements are shown in Table 7.5.1. The values in parentheses are the relative error in percentage. It can be observed that the estimated depths are within 5% of their actual values while most of the estimated densities are within 9% of their actual values. The density estimates with high errors are those obtained when the sources

were buried at 12 cm. This is likely caused by the fact that the sources have a large incident angle with respect to Detector 2 when buried at shallow depths. This results in the reduction of the geometric efficiency of Detector 2.

Actual Values	Estimated Values						
	$r = 3$ cm		$r = 9$ cm		$r = 15$ cm		
$d$ (cm)	$\rho_b$ ( $\text{g cm}^{-3}$ )	$d$ (cm)	$\rho_b$ ( $\text{g cm}^{-3}$ )	$d$ (cm)	$\rho_b$ ( $\text{g cm}^{-3}$ )	$d$ (cm)	$\rho_b$ ( $\text{g cm}^{-3}$ )
12	1.52	11.8 (2)	1.36 (11)	11.9 (1)	1.34 (12)	12.2 (1)	1.25 (18)
16	1.52	15.7 (2)	1.42 (7)	15.7 (2)	1.43 (6)	15.2 (5)	1.54 (1)
20	1.52	19.8 (1)	1.41 (7)	19.6 (2)	1.45 (5)	19.0 (5)	1.57 (3)
24	1.52	24.0 (0)	1.38 (9)	23.1 (4)	1.52 (0)	23.5 (2)	1.46 (4)
28	1.52	27.7 (1)	1.43 (6)	27.9 (0)	1.41 (7)	27.3 (2)	1.48 (3)

Table 7.5.1: Simultaneously-estimated depths and soil densities for disk sources of different radii buried at different depths in dry soil. The values in parentheses are the relative error in percentage.

Table 7.5.2 shows the depth and density estimates for a disk source ( $3 \text{ Bq cm}^{-2}$ ) of a radius of 3 cm buried at a depth of 20 cm in soil of different densities and volumetric water contents. The estimates in the first row were obtained using the proposed integrated GPR and gamma-ray detectors approach. The values in the second row were obtained using the measurements from only the two gamma-ray detectors by minimising the following function:

$$\text{minimise: } \frac{(R_{calc} - R_{sim})^2}{R_{sim}} \quad (7.5.2)$$

where  $R_{calc}$  and  $R_{sim}$  are the calculated and simulated flux ratios respectively. It can be observed that the combination of the gamma-ray detector and GPR measurements significantly improved the depth and density estimates especially at high densities and water contents. This is because the additional measurement from the GPR constrained the solution space to the correct values. The solution space can also be constrained by using a third gamma-ray detector measurement; however, this will either increase the data acquisition time if the measurements are acquired sequentially or require the design of a complicated measurement geometry for simultaneous measurement of all three fluxes. Conversely, this GPR integration approach is fast, simple, and produces good results.

Soil 1 ( $\rho_b = 1.67 \text{ g cm}^{-3}$ , $W_c = 15\%$ ), Soil 2 ( $\rho_b = 1.82 \text{ g cm}^{-3}$ , $W_c = 30\%$ ), Soil 3 ( $\rho_b = 1.97 \text{ g cm}^{-3}$ , $W_c = 45\%$ )						
Estimation Method	$d$ (cm)	$\rho_b$ ( $\text{g cm}^{-3}$ )	$d$ (cm)	$\rho_b$ ( $\text{g cm}^{-3}$ )	$d$ (cm)	$\rho_b$ ( $\text{g cm}^{-3}$ )
gamma detector and GPR	19.8 (1)	1.61 (4)	19.7 (2)	1.93 (6)	19.8 (1)	2.12 (8)
gamma detector only	19.17 (4)	1.48 (11)	17.6 (12)	1.5 (18)	16.83 (16)	1.5 (18)

Table 7.5.2: Depth and density estimates for a disk source of radius 3 cm buried at a depth of 20 cm in three different soil conditions. The values in parentheses are the relative error in percentage.

Finally, the results presented so far assumed that the size (i.e. radius) of the disk source is known. However, this is typically not the case in practice. Therefore, the retrieval of the radius of the disk source was also investigated. Since this would require the estimation of three unknowns using two equations, the problem was reformulated as a constrained minimisation problem where Equations (7.3.10) and (7.3.7) are the objective and constraint functions, respectively. The results for disk sources of different radii buried in the soil at a depth of 12 cm are shown in Table 7.5.3. Good estimates can be observed as all of the estimated values had relative errors of less than 10% except the density and radius estimates for the disk source of radius of 3 cm. This large error in the estimates for the disk source of radius 3 cm is likely due to the large incident angle for Detector 2 at shallow depths, which reduced the number of gamma rays reaching the detector. This reduction in the flux measured by Detector 2 at shallow depths is more pronounced if the radius of the disk source is small. However, the results confirmed the ability of the integrated gamma-ray detector and GPR method to estimate the key parameters of soil density, depth and radius of buried disk sources, simultaneously. Furthermore, this technique can also be used with other radioisotopes (e.g., Co-60) by substituting the mass attenuation coefficient at the photo peak energy of the radioisotope in Equation (7.3.3).

Table 7.5.3: Estimated depths, densities and radii values for disk sources of varying radii buried in the dry soil at a fixed depth of 12 cm. The values in parentheses are the relative error in percentage.

Actual Values			Estimated Values		
$d$ (cm)	$\rho_b$ (g cm <sup>-3</sup> )	$r$ (cm)	$d$ (cm)	$\rho_b$ (g cm <sup>-3</sup> )	$r$ (cm)
12	1.52	3	10.9 (9)	1.64 (8)	6.6 (120)
12	1.52	9	11.5 (4)	1.47 (3)	9.6 (7)
12	1.52	15	11.6 (3)	1.43 (6)	15.1 (1)

## 7.6 Conclusion

The integration of gamma-ray detectors and GPR for non-intrusive characterisation of buried radioactive objects has been presented. The results showed that this integrated approach is able to retrieve the key parameters of soil density, depth and radius of disk-shaped radioactive objects buried in soil of varying conditions simultaneously. It also showed that by using two horizontally-separated gamma-ray detectors, all the measurements required for the estimation process can be acquired simultaneously, thereby reducing the time associated with sequential data acquisition. However, the method is currently limited to objects having surface radioactive contamination that can be approximated by a disk. Therefore, there is a need to develop the method further to account for objects of different shapes. Finally, this study will form the

basis for the development an integrated gamma-ray detector and GPR system. Such a system will enable the rapid characterisation of buried wastes encountered during the decommissioning of nuclear sites and facilities.

## **7.7 Acknowledgement**

The authors would like to thank Dr. Douglas Offin (National Nuclear Laboratory, U.K.) for industrial supervision of the project.

# Chapter 8

## Conclusion

### 8.1 Summary

The integration of gamma-ray detectors and visual sensors (e.g., LiDAR and video cameras) have been used to solve some of the challenges in the detection and localisation of radioactive sources encountered during nuclear decommissioning. The literature review in Chapter 3 identified that the main function of the visual sensors was to provide the contextual information (e.g., velocity of the moving radioactive source) needed to complement the measurements from the gamma-ray detectors to enable detection and localisation of radioactive sources in these challenging scenarios. However visual sensors are not useful if the radioactive source is buried in opaque materials such as soil and concrete hence the need for GPR. Chapter 3 also identified the properties (e.g. density) of the embedding material as one of the key contextual information associated with buried radioactive sources obtainable from GPR.

In Chapters 4 and 5, a new non-intrusive depth estimation method for buried

radioactive sources from 2D raster radiation images was developed. The 2D radiation images were obtained by moving a gamma-ray detector in discrete steps across the surface of the embedding material volume and measuring the gamma-ray spectrum at each step. Accurate movement and positioning of the detector was achieved using the bespoke motorised mount described in Appendix A. The depth of the source was then estimated by fitting the intensity values from these spectra to an approximate 3D gamma-ray attenuation model. However, the depth estimates showed an increasing linear deviation from the actual depth as the depth of the source increases. Consequently, an initial calibration is required to obtain the linear equation required to correct this linear deviation. This new method was tested and validated using both Monte Carlo simulations and experiments using caesium-137 and cobalt-60 sources buried in sand and concrete.

Chapter 6 investigated four models for non-intrusive density estimation using GPR. The aim was to find the best density model for integration with the data from the gamma-ray detectors. The models were analysed using the reflected GPR signal from three materials namely sand, gravel and soil. The results showed that the exponential model with an exponent value of 0.65 gave the best density estimates with an average relative error of 4.5% across the three materials. This density estimation method was then combined with the depth estimation method previously developed to successfully estimate the depth of a 658 kBq caesium-137 radioactive source buried up to 18 cm in each of sand, gravel and soil.

The linearly increasing error in the result of the developed depth estimation method was initially thought to be as a result of using only the first two terms of

the binomial expansion during the derivation of the approximate 3D gamma-ray attenuation model. However, it was later discovered that this error was caused by the fact that the attenuation model did not account for the effect of the geometric efficiency. The geometric efficiency is the fraction of the gamma ray emitted by the source that is incident on the detector [26]. This depends on the angle subtended by the detector with respect to the source and the distance of the detector from the source. Consequently, the geometric efficiency is different for each position of the detector during the acquisition of the raster image. Also, the multiple measurements required to obtain a suitable raster image can result in long acquisition times especially if the buried source has low activity.

To overcome these limitations, an integrated gamma-ray detector and GPR method, which accounts for the effects of geometric efficiency and requires only two gamma-ray measurements was developed in Chapter 7. This new method makes use of the density relationship between the density model identified in Chapter 6, and the flux measured by gamma-ray detectors to simultaneously estimate the density of the embedding material, and the depth and radius of disk-shaped buried radioactive objects. The results from numerical simulations showed that this new method can simultaneously retrieve the soil density and the depth and radius of disk-shaped radioactive objects buried up to 20 cm in soil of varying conditions with a relative error of less than 10%. The results also showed that this new integration method solved the problem of increasing linear error in the estimated depth in addition to eliminating the need for prior knowledge of the density of the embedding material.

## 8.2 Significance of the research outputs

As discussed in Chapter 1, a significant amount of radioactive wastes still remain buried both in the soil and inside the walls and floors of structures in nuclear sites. These buried radioactive wastes constitute a major environmental and nuclear decommissioning challenge. Therefore, there is need for new and improved methods to effectively characterise these wastes to ensure their prompt and safe disposal.

The non-intrusive depth estimation methods developed in this thesis are a significant contribution to this need for improved characterisation methods for buried radioactive wastes. Firstly, the non-intrusive nature of the methods will make them faster to deploy thereby enabling rapid characterisation of large contaminated areas. In addition, it will also prevent secondary contamination of the deployed equipment and minimise the generation of secondary wastes associated with intrusive depth estimation methods.

Furthermore, the developed methods also have significant advantages compared to other non-intrusive methods. For instance, unlike the multiple photo peak methods [12, 120, 137], these new methods are not limited to radioisotopes with multiple photo peaks in their gamma spectra. Consequently, they can be used to investigate the entire range of possible gamma-ray emitting radioisotopes encountered during decommissioning. Also, the method developed in Chapter 7 do not require initial calibration to obtain model parameters. The derivation of depth estimation models from existing gamma radiation data is a one of the main limitations of empirical model depth estimation methods [123, 138, 139, 143]. This is because these empirical

models can only be applied to radiation data with the same characteristics as the one from which the model was derived.

Finally, the solution to the density dependency problem associated with non-intrusive radioactive source depth estimation methods is another significant benefit of the methods developed in this research. This will improve the accuracy of the depth estimates in practice because the estimated depths will be based on the current state of the embedding material and not on assumed or historical density values.

## **8.3 Future Work**

The techniques developed in this thesis represents the first time gamma-ray detectors and GPR will be integrated for the detection and localisation of buried radioactive wastes. While the results are promising, there still remain potential areas of improvement that need to be further explored. These are:

### **8.3.1 Different source geometries**

The geometry of the radioactive sources investigated in this thesis were point and planar source geometries with uniform activity. However, radioactive sources can be of any shape and size therefore, there is need to extend the depth estimation methods developed in this thesis so that they can be applied to sources that have a volume and other simple geometries. Extension to arbitrary source geometries may result in equations with intractable solutions. Therefore, it is suggested that complex geometries be approximated to the nearest simple geometry.

### 8.3.2 Multiple sources within the investigated area

The raster image method developed in Chapter 4 assumes only one radioactive source in the raster image. However, multiple radioactive sources could be located within the imaged area resulting in multiple hot spots in the acquired raster image. Therefore, there is need to extend the method to account for this scenario. A suggested solution is to use 2D Gaussian fitting techniques to isolate each hot spot in the image and then apply the depth estimation method to each isolated hot spot in the image.

### 8.3.3 Estimation of water content

The results in Chapters 6 and 7 showed that the GPR signal is affected by the presence of water in the embedding material. This can result in errors in the estimated density and depth of the embedding material and buried radioactive source respectively. Therefore, there is need to estimate the water content of the embedding material to prevent the breakdown of the methods for materials with significant water content. A potential solution is to use GPR inversion techniques [145, 178] instead of the GPR methods used in Chapters 6 and 7. GPR inversion have been shown to be able to simultaneously retrieve multiple material properties therefore, it has the potential to obtain both the density and water content of the embedding material. This will enable the developed integration methods to be extended to account for the effect of water in the embedding material thereby extending their application to radioactive sources buried in wet materials.

### 8.3.4 Design and fabrication of an integrated gamma-ray detector and GPR system

The gamma-ray and GPR data used in this thesis were acquired non-simultaneously using separate gamma-ray detector and GPR systems. This arrangement will not enable real-time implementation of the methods developed in this thesis. Therefore an integrated gamma-ray detector and GPR system needs to be developed. A suggested starting point is the system configuration used in Chapter 7 which consists of the GPR antenna placed between two gamma-ray detectors. Some of the parameters that would need to be optimised include the antenna size and shielding, the gamma-ray detector sizes, the collimator sizes and material and the gamma-ray detectors separation. The developed integrated system will find useful applications in nuclear decommissioning and land remediation.

# Appendix A

## Bespoke motorised mount

The motorised mount shown in Figure A.0.1 was designed and fabricated in order to automate the position of the detector during the experiments. The vertical and horizontal motions are controlled by the respective threaded shafts which are connected to servo motors. The horizontal and vertical resolutions are 3,237 and 3,125 steps per cm respectively. The operation of the mount was controlled via an arduino micro-controller by a custom data acquisition programme developed in MATLAB.

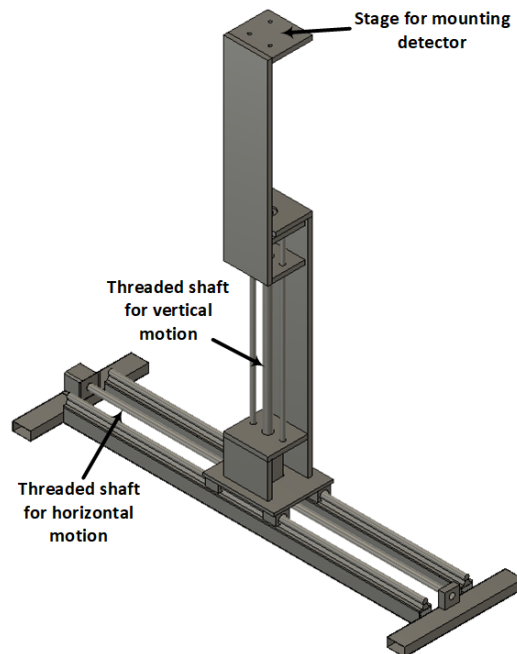


Figure A.0.1: CAD of bespoke motorised mount used in data acquisition

# Appendix B

## Data acquisition programme

The GUI of the custom MATLAB programme developed to automate the data acquisition process is shown in Figure B.0.1. The programme is also able to work with mixed field detectors to acquire both gamma and neutron radiation images.

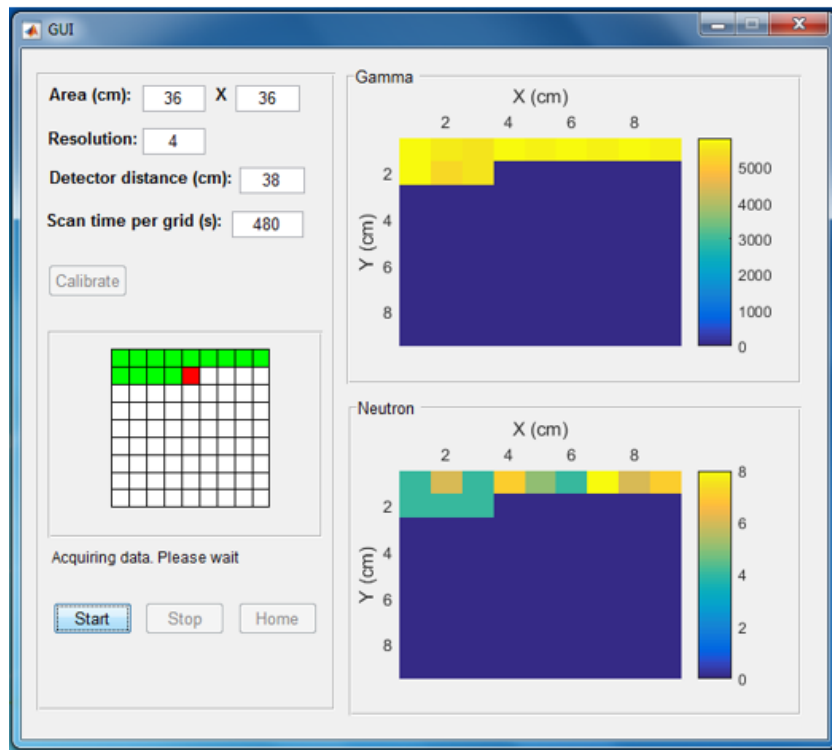


Figure B.0.1: GUI of the custom MATLAB data acquisition programme

# Appendix C

## Pulse height analysis code

```
1 %%%%%%%%%%%%%%%%%%%%%%%%%%%%%%%%%%%%%%%%%%%%%%%%%%%%%%%%%%%%%%%%%%%%%%%%%%
2 % Pulse height analysis MATLAB function by Ikechukwu Ukaegbu
3 %
4 % pulseFile: input file containing the pulses from oscilloscope
5 % thresh:    voltage thresh (mV)
6 % channels:  number of channels
7 % samples:   number of samples per pulse
8 % output:    histogram output
9 %%%%%%%%%%%%%%%%%%%%%%%%%%%%%%%%%%%%%%%%%%%%%%%%%%%%%%%%%%%%%%%%%%%%%%%%%%
10 function output = pha(pulseFile,thresh,samples,channels)
11 % Note: All constant values are specific to the experiment
12 % conditions used in the research in this thesis
13
14 % MWD (M) and MAF (L) windows for slow filter (in samples)
15 slow_M = 50; slow_L = slow_M-20;
16 slow_co = ones(1,slow_L)/slow_L; % coeffs for slow MAF
17 % MWD (M) and MAF (L) windows for fast filter (in samples)
18 fast_M = floor(slow_M/2); fast_L = fast_M-20;
19 fast_co = ones(1,fast_L)/fast_L; % coeffs for fast MAF
```

```
20 pz = 205; % pole zero (in samples)
21 mpd = pz*100/37; % minimum peak distance for findpeaks function
22 histData = []; % histogram data
23 histDataCnt = 0; % count of pulses processed
24 % open pulse file
25 fid = fopen(pulseFile);
26 % read pulse
27 data = fread(fid,samples,'double');
28 while ~isempty(data)
29     % perform slow filter
30     slow = filter(slow_co,1,mwd(data,slow_M,pz));
31     % perform fast filter
32     fast = filter(fast_co,1,mwd(data,fast_M,pz));
33     % find voltage peaks above threshold
34     pk = findpeaks(slow,'SortStr','descend','NPeaks',1,'MinPeakHeight',
35         thresh);
36     % perform pile-up rejection and return valid peaks
37     [V,~,status] = pileupreject(slow,fast,mpd,fast_M-fast_L,thresh);
38     % process return peaks
39     for i=1:length(V)
40         if status(i) == 1 % if peak is valid
41             % increment number of processed pulse
42             histDataCnt = histDataCnt+1;
43             % store peak's voltage value in histogram data
44             histData(histDataCnt) = V(i);
45         end
46     end
47 end
```

```

46     end
47     end
48     % read next pulse
49     data = fread(fid,samples,'double');
50     end
51     fclose(fid);
52     % return histogram
53     output = histcounts(histData,channels);

1  %%%%%%%%%%%%%%%%%%%%%%%%%%%%%%%%%%%%%%%%%%%%%%%%%%%%%%%%%%%%%%%%%%%%%%%%%
2  % Moving Window Deconvolution (MWD) MATLAB function
3  % by Ikechukwu Ukaegbu
4  %
5  % x:   signal
6  % win: Deconvolution window
7  % pz:  pole zero
8  % output: Deconvoluted signal
9  %%%%%%%%%%%%%%%%%%%%%%%%%%%%%%%%%%%%%%%%%%%%%%%%%%%%%%%%%%%%%%%%%%%%%%%%%
10 function output = mwd(x,win,pz)
11 n = length(x);
12 m = win;
13 output = zeros(1,n);
14 for i=m:n
15     d_m = x(i)-x(i-(m-1));
16     ma_m = 0;
17     for j=(i-(m-1)):i
18         ma_m = ma_m+x(j);
19     end

```

```

20   output(i) = d_m+ma_m/pz;
21   end

1  %%%%%%%%%%%%%%%%%%%%%%%%%%%%%%%%%%%%%%%%%%%%%%%%%%%%%%%%%%%%%%%%%%%%%%%%%
2  % Pile-up rejection MATLAB function by Ikechukwu Ukaegbu
3  %
4  % slow:    slow filtered signal
5  % fast:    fast filtered signal
6  % slow_ft: slow filtered signal flat top
7  % fast_ft: fast filtered signal flat top
8  % amp:     amplitude of peaks in slow signal
9  % status:  pile of status of peaks in amp
10 %         -1 for pile up and 1 for no pile up
11 %%%%%%%%%%%%%%%%%%%%%%%%%%%%%%%%%%%%%%%%%%%%%%%%%%%%%%%%%%%%%%%%%%%%%%%%%
12 function [amp,status] = pileupreject(slow,fast,slow_ft,fast_ft,thresh)
13 % Note: All constant values are specific to the experiment
14 % conditions used in the research in this thesis
15
16 % get lowest peak above threshold
17 pk = findpeaks(slow,'MinPeakHeight',thresh,'MinPeakDistance',slow_ft,'
    SortStr','ascend','NPeaks',1);
18 % get start and stop times (in samples) of
19 % peaks in the slow filtered signal
20 [x1,x2] = peakWidthCrossing(slow,1:length(slow),15,10,[0 pk]);
21 % initialise output variables
22 amp = zeros(size(x1));
23 status = ones(size(amp))*-1;
24 for i=1:length(x1)

```

```

25 X1 = floor(x1(i));
26 X2 = ceil(x2(i));
27 % get slow peaks' value
28 amp(i) = max(slow(X1:X2));
29 % find number of peaks in the fast filtered
30 % signal that are within the duration of a
31 % peak in the slow filtered signal
32     pks = findpeaks(fast(X1:X2), 'MinPeakHeight', thresh, '
33     MinPeakDistance', fast_ft);
34 % if number of peak in the fast filtered signal
35 % that are within the duration of a peak in the
36 % slow filtered signal is less than two, set slow
37 % peak's status to 1 (i.e. no pile-up)
38 if length(pks) < 2
39     status(i) = 1;
40 end
end

1 %%%%%%%%%%%%%%%%%%%%%%%%%%%%%%%%%%%%%%%%%%%%%%%%%%%%%%%%%%%%%%%%%%%%%%%%%
2 % Peak width crossing MATLAB function by Ikechukwu Ukaegbu
3 %
4 % y:    signal
5 % x:    time (in samples)
6 % pctRefLevel: percentage reference level
7 % tolerance:  tolerance
8 % stateLevel:  state level
9 %
10 % Note: see MATLAB pulswidth function documentation for

```

```
11 % more explanation
12 %%%%%%%%%%%%%%%%%%%%%%%%%%%%%%%%%%%%%%%%%%%%%%%%%%%%%%%%%%%%%%%%%%%%%%%%%
13 function [initCross,finalCross] = pulseWidthCrossing(y,x,pctRefLevel,
    tolerance,stateLevel)
14 % extract (absolute) reference levels
15 % from percent reference levels
16 amp = diff(stateLevel)/100;
17 low = stateLevel(1);
18 lwrBnd = low + tolerance * amp;
19 uprBnd = low + (100-tolerance) * amp;
20 refLevel = low + pctRefLevel*amp;
21 % extract the mid-crossings and polarities with the
22 % specified state boundaries and reference levels
23 [midCross, polarity] = signal.internal.getMidCross(y, x, uprBnd, lwrBnd
    , refLevel);
24 % find the first transition that matches
25 % the specified input polarity
26 iStart = find(polarity==1, 1, 'first');
27 idx = iStart:numel(polarity);
28 initCross = midCross(idx(1:2:end-1));
29 finalCross = midCross(idx(2:2:end));
```

# Bibliography

- [1] ONR. A guide to Nuclear Regulation in the UK. Technical report, Office for Nuclear Regulation, Merseyside, UK, 2016.
- [2] J. A. Garland and R. Wakeford. Atmospheric emissions from the Windscale accident of October 1957. *Atmospheric Environment*, 41(18):3904–3920, 2007. ISSN 13522310. doi: 10.1016/j.atmosenv.2006.12.049.
- [3] Georg Steinhauser, Alexander Brandl, and Thomas E. Johnson. Comparison of the Chernobyl and Fukushima nuclear accidents: A review of the environmental impacts. *Science of the Total Environment*, 470-471:800–817, 2014. ISSN 18791026. doi: 10.1016/j.scitotenv.2013.10.029.
- [4] UNSCEAR. Sources and Effects of Ionising Radiation. Technical report, United Nations, New York, USA, 2000.
- [5] B T Wilkins, J D Harrison, K R Smith, A W Phipps, P Bedwell, G Etherington, M Youngman, T P Fell, M W Charles, and P J Darley. Health implications of fragments of irradiated fuel at the beach at Sandside Bay Module 6 : Overall results. Technical report, Health Protection Agency, Oxfordshire, UK, 2006.

- [6] M Charles, J Harrison, P Darley, and T Fell. Health implications of Dounreay fuel fragments: Estimates of doses and risks. In *Proceedings of the Seventh International Symposium of the Society for Radiological Protection*, pages 23–29, Cardiff, UK, 2005. Society for Radiological Protection.
- [7] Andrew Popp, Cris Ardouin, Mark Alexander, Robert Blackley, and Allan Murray. Improvement of a high risk category source buried in the grounds of a hospital in Cambodia. In *13th International Congress of the International Radiation Protection Association*, pages 1–10, Glasgow, UK, 2012.
- [8] Bill Miller, Amec Foster, Mike Davies Nuvia, Marcus Hill, and Amec Foster. Pipeline Characterisation and Decommissioning within the Nuclear Industry : Technology Review and Site Experience. Technical Report 2, Nuclear Decommissioning Authority, Cumbria, UK, 2016.
- [9] Bill Miller, Amec Foster, Pete Burgess, Radiation Metrology, Marcus Hill, and Amec Foster. Pipeline Characterisation and Decommissioning within the Nuclear Industry : Good Practice Guide. Technical Report 2, Nuclear Decommissioning Authority, Cumbria, UK, 2016.
- [10] Michele Laraia, editor. *Nuclear decommissioning: Planning, execution and international experience*. Woodhead Publishing Limited, Cambridge, UK, 2012. ISBN 9780857091154.
- [11] W. E Norris, D. J Naus, and H. L Graves. Inspection of nuclear power plant

- containment structures. *Nuclear Engineering and Design*, 192(2-3):303–329, 1999. ISSN 00295493. doi: 10.1016/S0029-5493(99)00125-9.
- [12] Alan Shippen and Malcolm J. Joyce. Profiling the depth of caesium-137 contamination in concrete via a relative linear attenuation model. *Applied Radiation and Isotopes*, 68(4-5):631–634, 2010. ISSN 09698043. doi: 10.1016/j.apradiso.2009.09.046.
- [13] P O Sullivan, J G Nokhamzon, and E Cantrel. Decontamination and dismantling of radioactive concrete structures, 2010.
- [14] IAEA. Radiation protection and safety of radiation sources: International basic safety standards. Technical Report GSR Part 3, International Atomic Energy Agency, Vienna, Austria, 2014.
- [15] B. Penrose, K. A. Johnson née Payne, A. Arkhipov, A. Maksimenko, S. Gaschak, M. C. Meacham, N. J.M. Crout, P. J. White, N. A. Beresford, and M. R. Broadley. Inter-cultivar variation in soil-to-plant transfer of radiocaesium and radiostrontium in Brassica oleracea. *Journal of Environmental Radioactivity*, 155-156:112–121, 2016. ISSN 18791700. doi: 10.1016/j.jenvrad.2016.02.020.
- [16] NAO. Progress on the Sellafield site: an update. Technical report, National Audit Office, London, UK, 2015.
- [17] A Baberdin, A Dutova, A Fedorov, M. Korzhik, V. Ligoun, O. Missevitch, V. Kazak, A. Vinokurov, and S. Zagumenov. (Lu-Y)AlO<sub>3</sub>:Ce Scintillator for

- Well Logging. *IEEE Transactions on Nuclear Science*, 55(3):1170–1173, jun 2008. ISSN 0018-9499. doi: 10.1109/TNS.2008.919261.
- [18] C. Carasco, B. Perot, J. L. Ma, H. Toubon, and A. Dubille-Auchere. Improving gross count gamma-ray logging in uranium mining with the NGRS probe. *IEEE Transactions on Nuclear Science*, 65(3):919–923, 2018. ISSN 00189499. doi: 10.1109/TNS.2018.2800909.
- [19] Adam Varley, Andrew Tyler, Leslie Smith, and Paul Dale. Development of a neural network approach to characterise  $^{226}\text{Ra}$  contamination at legacy sites using gamma-ray spectra taken from boreholes. *Journal of Environmental Radioactivity*, 140:130–140, 2015. ISSN 18791700. doi: 10.1016/j.jenvrad.2014.11.011.
- [20] Koji Maeda, Shinji Sasaki, Misaki Kumai, Isamu Sato, Mitsuo Suto, Masahiko Ohsaka, Tetsuo Goto, Hitoshi Sakai, Takayuki Chigira, and Hirotohi Murata. Distribution of radioactive nuclides of boring core samples extracted from concrete structures of reactor buildings in the Fukushima Daiichi Nuclear Power Plant. *Journal of Nuclear Science and Technology*, 51(7-8):1006–1023, 2014. ISSN 00223131. doi: 10.1080/00223131.2014.915769.
- [21] O Gal, B Dessus, F Jean, F Lainé, and C Lévêque. Operation of the CAR-TOGAM portable gamma camera in a photon-counting mode. In *Nuclear Science Symposium (NSS) 2000*, volume 48, pages 1198–1204, 2001. doi: 10.1109/23.958750.

- [22] Frédérick Carrel, Roger Abou Khalil, Sébastien Colas, Daniel De Toro, Gilles Ferrand, Emmanuelle Gaillard, Mehdi Gmar, Daniel Hameau, Sylvie Jahan, Frédéric Lainé, Anne-sophie Lalleman, François Lemasle, Charly Mahé, Jean-eric Maurer, Nabil Mena, Stéphane Normand, Hervé Onillon, Nicolas Saurel, and Hervé Toubon. GAMPIX : a New Gamma Imaging System for Radiological Safety and Homeland Security Purposes. In *IEEE Nuclear Science Symposium and Medical Imaging Conference*, pages 4739–4744. IEEE, 2011. ISBN 9781467301190. doi: 10.1109/NSSMIC.2011.6154706.
- [23] K.a.a. Gamage, M.J. Joyce, and J.C. Adams. Combined digital imaging of mixed-field radioactivity with a single detector. *Nuclear Instruments and Methods in Physics Research Section A: Accelerators, Spectrometers, Detectors and Associated Equipment*, 635(1):74–77, 2011. ISSN 01689002. doi: 10.1016/j.nima.2011.01.033.
- [24] Christopher G. Wahl, Willy R. Kaye, Weiyi Wang, Feng Zhang, Jason M. Jaworski, Alexis King, Y. Andy Boucher, and Zhong He. The Polaris-H imaging spectrometer. *Nuclear Instruments and Methods in Physics Research Section A: Accelerators, Spectrometers, Detectors and Associated Equipment*, 784:377–381, 2015. ISSN 01689002. doi: 10.1016/j.nima.2014.12.110.
- [25] Doug Reilly. The Origin of Gamma Rays. In Doug Reilly, Norbert Ensslin, Hastings Jr. Smith, and Kreiner Sarah, editors, *Passive Nondestructive Assay of Nuclear Materials*, chapter 1, pages 1–25. Los Alamos National Laboratory, NM, USA, 1991. ISBN 0-16-032724.

- [26] Glen Knoll. Radiation Interactions. In *Radiation Detection and Measurement*, chapter 2, pages 47–53. John Wiley and Sons Inc., NJ, USA, 4 edition, 2010.
- [27] Pierre Radvanyi and Jacques Villain. La découverte de la radioactivité. *Comptes Rendus Physique*, 18(9-10):544–550, 2017. ISSN 16310705. doi: 10.1016/j.crhy.2017.10.008.
- [28] G. Nelson and Doug Reilly. Gamma-Ray Interactions with Matter. In Doug Reilly, Norbert Ensslin, Hastings Jr. Smith, and Kreiner Sarah, editors, *Passive Nondestructive Assay of Nuclear Materials*, chapter 2, pages 27–42. Los Alamos National Laboratory, NM, USA, 1991. ISBN 0-16-032724.
- [29] Frederick Soddy and Alexander Russell. The Gamma-rays of Uranium and Radium. *Philosophical Magazine*, 18:620–649, 1909.
- [30] S. A.Syam Kumar and Nagarajan Vivekanandan. Patient specific quality assurance of RapidArc pre treatment plans using semiflex 0.125 cc ionization chamber. *Radiation Physics and Chemistry*, 130(October 2016):426–430, 2017. ISSN 18790895. doi: 10.1016/j.radphyschem.2016.10.001.
- [31] L. Gaudefroy, T. Roger, J. Pancin, C. Spitaels, J. Aupiais, and J. Mottier. A twin Frisch-grid ionization chamber as a selective detector for the delayed gamma-spectroscopy of fission fragments. *Nuclear Instruments and Methods in Physics Research, Section A: Accelerators, Spectrometers, Detectors and Associated Equipment*, 855(December 2016):133–139, 2017. ISSN 01689002. doi: 10.1016/j.nima.2017.02.071.

- [32] Hastings Jr. Smith and Marcia Lucas. Gamma-Ray Detectors. In Doug Reilly, Norbert Ensslin, Hastings Jr. Smith, and Kreiner Sarah, editors, *Passive Non-destructive Assay of Nuclear Materials*, chapter 3, pages 43–63. Los Alamos National Laboratory, NM, USA, 1991. ISBN 0-16-032724.
- [33] L E Adam, J S Karp, and R Freifelder. Energy-based scatter correction for 3-D PET scanners using NaI(Tl) detectors. *IEEE Trans Med Imaging*, 19(5): 513–521, 2000.
- [34] S.M. Ignatov, V.M. Chirkin, V.N. Potapov, O.P. Ivanov, V.E. Stepanov, and L.J. Meng. Environmental monitoring using large-volume CsI(Tl) scintillation counters. *2001 IEEE Nuclear Science Symposium Conference Record (Cat. No.01CH37310)*, 1:380–384, 2005. doi: 10.1109/nssmic.2001.1008481.
- [35] D.C. Stromswold, E.R. Siciliano, J.E. Schweppe, J.H. Ely, B.D. Milbrath, R.T. Kouzes, and B.D. Geelhood. Comparison of plastic and NaI(Tl) scintillators for vehicle portal monitor applications. *2003 IEEE Nuclear Science Symposium. Conference Record (IEEE Cat. No.03CH37515)*, 2:1065–1069 Vol.2, 2008. doi: 10.1109/nssmic.2003.1351876.
- [36] D. Yan, Z. Y. Sun, K. Yue, S. T. Wang, X. H. Zhang, Y. H. Yu, J. L. Chen, S. W. Tang, F. Fang, Y. Zhou, Y. Sun, Z. M. Wang, and Y. Z. Sun. Design and construction of a multi-layer CsI(Tl) telescope for high-energy reaction studies. *Nuclear Instruments and Methods in Physics Research, Section A: Accelerators*,

- Spectrometers, Detectors and Associated Equipment*, 843(December 2015):5–10, 2017. ISSN 01689002. doi: 10.1016/j.nima.2016.10.053.
- [37] Jin Wang, Yingying Zhang, Dongyan Liu, Bingwei Wu, Ying Zhang, and Husen Jiang. Automated spectra analysis of in situ radioactivity measurements in the marine environment using NaI(Tl) detector. *Applied Radiation and Isotopes*, 141(May):88–94, 2018. ISSN 18729800. doi: 10.1016/j.apradiso.2018.08.026.
- [38] R. Elftmann, S. Boden, J. C. Terasa, and R. F. Wimmer-Schweingruber. Temperature dependence of ionization quenching in BGO scintillators. *Nuclear Instruments and Methods in Physics Research, Section B: Beam Interactions with Materials and Atoms*, 451(May):93–98, 2019. ISSN 0168583X. doi: 10.1016/j.nimb.2019.05.038.
- [39] R. Billnert, S. Oberstedt, E. Andreotti, M. Hult, G. Marissens, and A. Oberstedt. New information on the characteristics of 1 in.×1 in. cerium bromide scintillation detectors. *Nuclear Instruments and Methods in Physics Research, Section A: Accelerators, Spectrometers, Detectors and Associated Equipment*, 647(1):94–99, 2011. ISSN 01689002. doi: 10.1016/j.nima.2011.05.034.
- [40] B. Belhorma, M.Y. Messous, A. Elanique, A. Benahmed, and I. Mouhti. Validation of a NaI(Tl) and LaBr<sub>3</sub>(Ce) detector’s models via measurements and Monte Carlo simulations. *Journal of Radiation Research and Applied Sciences*, 11(4):335–339, 2018. ISSN 16878507. doi: 10.1016/j.jrras.2018.06.003.
- [41] J. Nattress and I. Jovanovic. Response and calibration of organic scintillators

- for gamma-ray spectroscopy up to 15-MeV range. *Nuclear Instruments and Methods in Physics Research, Section A: Accelerators, Spectrometers, Detectors and Associated Equipment*, 871(May):1–7, 2017. ISSN 01689002. doi: 10.1016/j.nima.2017.07.024.
- [42] Takayuki Yanagida, Kenichi Watanabe, and Yutaka Fujimoto. Comparative study of neutron and gamma-ray pulse shape discrimination of anthracene, stilbene, and p-terphenyl. *Nuclear Instruments and Methods in Physics Research, Section A: Accelerators, Spectrometers, Detectors and Associated Equipment*, 784:111–114, 2015. ISSN 01689002. doi: 10.1016/j.nima.2014.12.031.
- [43] Matthieu Hamel, Malik Soumaré, Hana Burešová, and Guillaume H.V. Bertrand. Tuning the decay time of plastic scintillators. *Dyes and Pigments*, 165 (January):112–116, 2019. ISSN 18733743. doi: 10.1016/j.dyepig.2019.02.007.
- [44] K. A.A. Gamage, M. J. Joyce, and G. C. Taylor. A digital approach to neutron- $\gamma$  imaging with a narrow tungsten collimator aperture and a fast organic liquid scintillator detector. *Applied Radiation and Isotopes*, 70(7):1223–1227, 2012. ISSN 09698043. doi: 10.1016/j.apradiso.2012.01.021.
- [45] Jack Parker. General Topics in Passive Gamma-Ray Assay. In Doug Reilly, Norbert Ensslin, Hastings Jr. Smith, and Kreiner Sarah, editors, *Passive Non-destructive Assay of Nuclear Materials*, chapter 5, pages 95–158. Los Alamos National Laboratory, NM, USA, 1991. ISBN 0-16-032724.
- [46] Justin Knowles, Steven Skutnik, David Glasgow, and Roger Kapsimalis. A

- generalized method for characterization of  $^{235}\text{U}$  and  $^{239}\text{Pu}$  content using short-lived fission product gamma spectroscopy. *Nuclear Instruments and Methods in Physics Research, Section A: Accelerators, Spectrometers, Detectors and Associated Equipment*, 833:38–44, 2016. ISSN 01689002. doi: 10.1016/j.nima.2016.06.112.
- [47] Hee Dong Choi and Junhyuck Kim. Basic characterization of uranium by high-resolution gamma spectroscopy. *Nuclear Engineering and Technology*, 50(6): 929–936, 2018. ISSN 2234358X. doi: 10.1016/j.net.2018.04.008.
- [48] H. Lemaire, R. Abou Khalil, K. Amgarou, J.-C. Angélique, F. Bonnet, D. De Toro, F. Carrel, O. Giarmana, M. Gmar, N. Mena, Y. Menesguen, S. Normand, A. Patoz, V. Schoepff, P. Talent, and T. Timi. Implementation of an imaging spectrometer for localization and identification of radioactive sources. *Nuclear Instruments and Methods in Physics Research Section A: Accelerators, Spectrometers, Detectors and Associated Equipment*, 763:97–103, 2014. ISSN 01689002. doi: 10.1016/j.nima.2014.05.118.
- [49] S. Dubos, H. Lemaire, S. Schanne, O. Limousin, F. Carrel, V. Schoepff, and C. Blondel. ORIGAMIX, a CdTe-based spectro-imager development for nuclear applications. *Nuclear Instruments and Methods in Physics Research Section A: Accelerators, Spectrometers, Detectors and Associated Equipment*, 787:302–307, 2015. ISSN 01689002. doi: 10.1016/j.nima.2014.12.111.
- [50] Jack Parker. Instrumentation for Gamma-Ray Spectroscopy. In Doug Reilly,

- Norbert Ensslin, Hastings Jr. Smith, and Kreiner Sarah, editors, *Passive Non-destructive Assay of Nuclear Materials*, chapter 4, pages 65–94. Los Alamos National Laboratory, NM, USA, 1991. ISBN 0-16-032724.
- [51] Ilgis Ibragimov and Elena Ibragimova. High performance ground penetrating radar with up to 1 KM range on coal-mining area. *2011 6th International Workshop on Advanced Ground Penetrating Radar, IWAGPR 2011*, 2011. doi: 10.1109/IWAGPR.2011.5963843.
- [52] Mohammad Reza Mahmoudzadeh Ardekani. Off- and on-ground GPR techniques for field-scale soil moisture mapping. *Geoderma*, 200-201(1):55–66, jun 2013. ISSN 00167061. doi: 10.1016/j.geoderma.2013.02.010.
- [53] Mar??a A. Gonzalez-Huici, Ilaria Catapano, and Francesco Soldovieri. A comparative study of GPR reconstruction approaches for landmine detection. *IEEE Journal of Selected Topics in Applied Earth Observations and Remote Sensing*, 7(12):4869–4878, 2014. ISSN 21511535. doi: 10.1109/JSTARS.2014.2321276.
- [54] S.F. Senin and R. Hamid. Ground penetrating radar wave attenuation models for estimation of moisture and chloride content in concrete slab. *Construction and Building Materials*, 106:659–669, 2016. ISSN 09500618. doi: 10.1016/j.conbuildmat.2015.12.156.
- [55] Mohamed S. El-Mahallawy and Mazlan Hashim. Material classification of underground utilities from GPR images using DCT-based SVM approach.

- IEEE Geoscience and Remote Sensing Letters*, 10(6):1542–1546, 2013. ISSN 1545598X. doi: 10.1109/LGRS.2013.2261796.
- [56] A P. Annan. Electromagnetic Principles of Ground Penetrating Radar. In Harry M Jol, editor, *Ground Penetrating Radar Theory and Applications*, chapter 1, page 18. Elsevier, Oxford, UK, 1 edition, 2009.
- [57] Steven Koppenjan. Ground Penetrating Radar Systems and Design. In Harry Jol, editor, *Ground Penetrating Radar Theory and Applications*, chapter 3, pages 73–95. Elsevier, Oxford, UK, first edition, 2009.
- [58] David J. Daniels. Antennas. In David J. Daniels, editor, *Ground Penetrating Radar*, chapter 5, page 132. IEEE, London, UK, 2 edition, 2004. ISBN 0863413609.
- [59] Constatine Balanis. *Antenna Theory Analysis and Design*. John Wiley and Sons Inc., 4 edition, 2016. ISBN 978-1-118-642060-1.
- [60] Iraklis Giannakis, Antonios Giannopoulos, and Craig Warren. Realistic FDTD GPR Antenna Models Optimized Using a Novel Linear/Nonlinear Full-Waveform Inversion. *IEEE Transactions on Geoscience and Remote Sensing*, 57(3):1768–1778, 2019. ISSN 01962892. doi: 10.1109/TGRS.2018.2869027.
- [61] I.K. Ukaegbu and K.A.A. Gamage. Parametric Analysis and Bandwidth Optimisation of Hybrid Linear-exponential Tapered Slot Vivaldi Antennas. In *Loughborough Antennas & Propagation Conference (LAPC 2017)*. Institu-

- tion of Engineering and Technology, 2017. ISBN 978-1-78561-699-0. doi: 10.1049/cp.2017.0279.
- [62] Amr Ahmed, Yu Zhang, Dylan Burns, Dryver Huston, and Tian Xia. Design of UWB antenna for air-coupled impulse ground-penetrating radar. *IEEE Geoscience and Remote Sensing Letters*, 13(1):92–96, 2016. doi: 10.1109/LGRS.2015.2498404.
- [63] David M. Pozar. *Microwave Engineering*. John Wiley and Sons Inc., NJ, USA, 4 edition, 2012. ISBN 978-0-470-63155-3.
- [64] Kathryn C. Elkins, Valeria M. Moncayo, Hyunmi Kim, and Larry D. Olson. Utility of gray-matter segmentation of ictal-Interictal perfusion SPECT and interictal 18F-FDG-PET in medically refractory epilepsy. *Epilepsy Research*, 130:93–100, 2017. ISSN 09201211. doi: 10.1016/j.eplepsyres.2017.01.009.
- [65] E. T H Clifford, J. E. McFee, H. Ing, H. R. Andrews, D. Tennant, E. Harper, and A. A. Faust. A militarily fielded thermal neutron activation sensor for landmine detection. *Nuclear Instruments and Methods in Physics Research, Section A: Accelerators, Spectrometers, Detectors and Associated Equipment*, 579(1):418–425, 2007. ISSN 01689002. doi: 10.1016/j.nima.2007.04.091.
- [66] Timothy J. Aucott, Mark S. Bandstra, Victor Negut, Daniel H. Chivers, Reynold J. Cooper, and Kai Vetter. Routine surveys for Gamma-Ray background characterization. *IEEE Transactions on Nuclear Science*, 60(2):1147–1150, 2013. ISSN 00189499. doi: 10.1109/TNS.2013.2251355.

- [67] Alex Pappachen James and Belur V. Dasarathy. Medical image fusion: A survey of the state of the art. *Information Fusion*, 19(1):4–19, 2014. ISSN 15662535. doi: 10.1016/j.inffus.2013.12.002.
- [68] M Gmar, O Gal, C Le Goaller, O P Ivanov, V N Potapov, V E Stepanov, F Laine, and F Lamadie. Development of coded-aperture imaging with a compact gamma camera. *IEEE Transactions on Nuclear Science*, 51(4):1052–1056, 2003. ISSN 00189499. doi: 10.1109/TNS.2004.832608.
- [69] Olivier Gal, Mehdi Gmar, Oleg P. Ivanov, Frédéric Lainé, Fabrice Lamadie, Christophe Le Goaller, Charly Mahé, Erwan Manach, and Vyacheslav E. Stepanov. Development of a portable gamma camera with coded aperture. *Nuclear Instruments and Methods in Physics Research Section A: Accelerators, Spectrometers, Detectors and Associated Equipment*, 563(1):233–237, 2006. ISSN 01689002. doi: 10.1016/j.nima.2006.01.119.
- [70] K.a. Hughes and J.a. Lightfoot. RadScan 600-a portable instrument for the remote imaging of gamma contamination: its design and use in aiding decommissioning strategy. In *IEEE Nuclear Science Symposium. Conference Record*, pages 930–933, California, USA, 1997. IEEE. ISBN 0-7803-3534-1. doi: 10.1109/NSSMIC.1996.591500.
- [71] Michael Ecker and Richard Vincent. Light Detection and Ranging ( LiDAR ) Technology Evaluation. Technical report, Missouri Department of Transportation, Missouri, USA, 2010.

- [72] V Sequeira and J G M Goncalves. 3D Verification of Plant Design. In *Proc. 25th ESARDA Symposium on Safeguards and Nuclear Material Management*, Stockholm, Sweden, 2003. IAEA.
- [73] L Mihailescu, K Vetter, W Ruhter, D Chivers, C Coates, S Smith, J Hines, A C R Caiado, V Sequeira, M Fiocco, and J G M Goncalves. Combined Measurements with Three-dimensional Design Information Verification System and Gamma Ray Imaging-A Collaborative Effort Between Oak Ridge National Laboratory, The Joint Research Center at ISPRA. In *47th INMM Annual Meeting*, Tennessee, USA, 2006. Insitute of Nuclear Materials Management.
- [74] Ana C. Raffo-Caiado, Klaus-Peter Ziock, Jason P Hayward, Stephen Smith, Alexander Solodov, Lucian Mihailescu, Kai Vetter, Arden Dougan, Morgan Burks, Joao Goncallves, Vitor Sequeira, Orpet P Peixoto, Silvio Almeida, Erwin Galdoz, and Geraldo Renha. Investigation of Combined Measurements with Three-Dimensional Design Information Verification System and Gamma-Ray ... In *50th INMM Annual Meeting*, pages 12–16, Arizona, USA, 2009. Insitute of Nuclear Materials Management.
- [75] Chris Boehnen, Vincent Paquit, Klaus Ziock, Tyler Guzzardo, Michael Whitaker, and Ana Raffo-Caiado. Field trial of a highly portable coded aperture gamma ray and 3D imaging system. In *2011 Future of Instrumentation International Workshop (FIIW) Proceedings*, pages 75–78, Tennessee, USA, 2011. IEEE. ISBN 978-1-4673-5836-1. doi: 10.1109/FIIW.2011.6476819.

- [76] David Hall and James Llinas. An introduction to multisensor data fusion. *Proceedings of the IEEE*, 85(1):6–23, 2002. ISSN 00189219. doi: 10.1109/5.554205.
- [77] H. F. Durrant-Whyte. Sensor Models and Multisensor Integration. *The International Journal of Robotics Research*, 7(6):97–113, 1988. ISSN 0278-3649. doi: 10.1177/027836498800700608.
- [78] R Luo and M Kay. *Data Fusion and Sensor Integration*. Academic Press, Boston, USA, 1992.
- [79] Essa Basaeed, Harish Bhaskar, and Mohammed Al-Mualla. Beyond pan-sharpening: Pixel-level fusion in remote sensing applications. In *International Conference on Innovations in Information Technology, IIT*, pages 139–144, Abu Dhabi, UAE, 2012. IEEE. ISBN 9781467311014. doi: 10.1109/INNOVATIONS.2012.6207718.
- [80] Phillip Riley, Andreas Enqvist, and Sanjeev J. Koppal. Low-Cost Depth and Radiological Sensor Fusion to Detect Moving Sources. In *2015 International Conference on 3D Vision*, pages 198–205, Lyon, France, 2015. IEEE. ISBN 9781467383325. doi: 10.1109/3DV.2015.30.
- [81] K. P. Ziock, A. Cheriyyadat, L. Fabris, J. Goddard, D. Hornback, T. Karnowski, R. Kerekes, and J. Newby. Autonomous radiation monitoring of small vessels. *Nuclear Instruments and Methods in Physics Research, Section A: Accelerators, Spectrometers, Detectors and Associated Equipment*, 652(1):10–15, 2011. ISSN 01689002. doi: 10.1016/j.nima.2011.01.176.

- [82] K. P. Ziock, E. C. Bradley, A. Cheriyyadat, M. Cunningham, L. Fabris, C. L. Fitzgerald, J. S. Goddard, D. E. Hornback, R. A. Kerekes, T. P. Karnowski, W. T. Marchant, and J. Newby. Performance of the roadside tracker portal-less portal monitor. *IEEE Transactions on Nuclear Science*, 60(3):2237–2246, 2013. ISSN 00189499. doi: 10.1109/TNS.2013.2262472.
- [83] Dashan Gao, Yi Yao, Feng Pan, Ting Yu, Bing Yu, Li Guan, Walter Dixon, Brian Yanoff, Tai Peng Tian, and Nils Krahnstoeber. Computer vision aided target linked radiation imaging. In *Proceedings of the IEEE Computer Society Conference on Computer Vision and Pattern Recognition*, pages 1162–1169, Rhode Island, USA, 2012. IEEE. ISBN 9781467312264. doi: 10.1109/CVPR.2012.6247797.
- [84] Lucian Mihailescu, Kai Vetter, and Daniel Chivers. Standoff 3D gamma-ray imaging. *IEEE Transactions on Nuclear Science*, 56(2):479–486, 2009. ISSN 00189499. doi: 10.1109/TNS.2009.2015304.
- [85] Zhiling Long, Wei Wei, Anish Turlapaty, Qian Du, and Nicolas H. Younan. Fusion of radiation and electromagnetic induction data for buried radioactive target detection and characterization. *IEEE Transactions on Nuclear Science*, 60(2):1126–1133, 2013. ISSN 00189499. doi: 10.1109/TNS.2013.2247062.
- [86] Ashok Sundaresan, Pramod K. Varshney, and Nageswara S V Rao. Distributed detection of a nuclear radioactive source using fusion of correlated decisions. In

- 10th International Conference on Information Fusion FUSION 2007*, Quebec, Canada, 2007. IEEE. ISBN 0662478304. doi: 10.1109/ICIF.2007.4408143.
- [87] Jren-Chit Chin, David K.Y. Yau, Nageswara S.V. Rao, Yong Yang, Chris Y.T. Ma, and Mallikarjun Shankar. Accurate localization of low-level radioactive source under noise and measurement errors. In *Proceedings of the 6th ACM conference on Embedded network sensor systems*, NC, USA, 2008. ACM. ISBN 9781595939906. doi: 10.1145/1460412.1460431.
- [88] Nageswara S V Rao, Satyabrata Sen, Nicholas J. Prins, Daniel A. Cooper, Robert J. Ledoux, James B. Costales, Krzysztof Kamieniecki, Steven E. Korbly, Jeffrey K. Thompson, James Batcheler, Richard R. Brooks, and Chase Q. Wu. Network algorithms for detection of radiation sources. *Nuclear Instruments and Methods in Physics Research, Section A: Accelerators, Spectrometers, Detectors and Associated Equipment*, 784:326–331, 2015. ISSN 01689002. doi: 10.1016/j.nima.2015.01.037.
- [89] Daniel Moreno and Gabriel Taubin. Simple, accurate, and robust projector-camera calibration. In *2012 Second International Conference on 3D Imaging, Modeling, Processing, Visualization and Transmission (3DIMPVT)*,, pages 464–471, Zurich, Switzerland, 2012. IEEE. ISBN 9780769548739. doi: 10.1109/3DIMPVT.2012.77.
- [90] Klaus P. Ziock, Lorenzo Fabris, Dennis Carr, Jeff Collins, Mark Cunningham, Frezghi Habte, Tom Karnowski, and William Marchant. A fieldable-prototype,

- large-area, gamma-ray imager for orphan source search. *IEEE Transactions on Nuclear Science*, 55(6):3643–3653, 2008. ISSN 00189499. doi: 10.1109/TNS.2008.2006753.
- [91] Bruce D Lucas and Takeo Kanade. An iterative image registration technique with an application to stereo vision. In *International Joint Conference on Artificial Intelligence*, pages 674–679, Vancouver, 1981. ISBN 0001-0782. doi: Doi10.1145/358669.358692.
- [92] K. P. Ziock, C. B. Boehnen, J. M. Ernst, L. Fabris, J. P. Hayward, T. P. Karnowski, V. C. Paquit, D. R. Patlolla, and D. G. Trombino. Motion correction for passive radiation imaging of small vessels in ship-to-ship inspections. *Nuclear Instruments and Methods in Physics Research, Section A: Accelerators, Spectrometers, Detectors and Associated Equipment*, 805:116–126, 2016. ISSN 01689002. doi: 10.1016/j.nima.2015.08.040.
- [93] S. J. Wilderman, J. A. Fessler, N. H. Clinthorne, J. W. LeBlanc, and W. L. Rogers. Improved modeling of system response in list mode EM reconstruction of Compton scatter camera images. *IEEE Transactions on Nuclear Science*, 48(1 I):111–116, 2001. ISSN 00189499. doi: 10.1109/23.910840.
- [94] Kai Vetter. Multi-sensor radiation detection, imaging, and fusion. *Nuclear Instruments and Methods in Physics Research Section A: Accelerators, Spectrometers, Detectors and Associated Equipment*, 805:127–134, jan 2016. ISSN 01689002. doi: 10.1016/j.nima.2015.08.078.

- [95] K P Ziock, J W Collins, L Fabris, S Gallagher, B K P Horn, R C Lanza, and N W Madden. Source-Search Sensitivity of a Large-Area , Coded-Aperture, Gamma-ray Imager. *IEEE Transactions on Nuclear Science*, 53(3):1614–1621, 2006. doi: 10.1109/TNS.2006.875285.
- [96] Mark S. Bandstra, Timothy J. Aucott, Erik Brubaker, Daniel H. Chivers, Reynold J. Cooper, Joseph C. Curtis, John R. Davis, Tenzing H. Joshi, John Kua, Ross Meyer, Victor Negut, Michael Quinlan, Brian J. Quiter, Shreyas Srinivasan, Avidesh Zakhor, Richard Zhang, and Kai Vetter. RadMAP: The Radiological Multi-sensor Analysis Platform. *Nuclear Instruments and Methods in Physics Research, Section A: Accelerators, Spectrometers, Detectors and Associated Equipment*, 840(May):59–68, 2016. ISSN 01689002. doi: 10.1016/j.nima.2016.09.040.
- [97] Timothy J. Aucott, Mark S. Bandstra, Victor Negut, Joseph C. Curtis, Daniel H. Chivers, and Kai Vetter. Effects of Background on Gamma-Ray Detection for Mobile Spectroscopy and Imaging Systems. *IEEE Transactions on Nuclear Science*, 61(2):985–991, 2014. doi: 10.1109/TNS.2014.2306998.
- [98] Qian Du, Wei Wei, Daniel May, and Nicolas H. Younan. Noise-adjusted principal component analysis for buried radioactive target detection and classification. *IEEE Transactions on Nuclear Science*, 57(6 PART 2):3760–3767, 2010. ISSN 00189499. doi: 10.1109/TNS.2010.2084105.
- [99] He Yang, Qian Du, and Ben Ma. Decision fusion on supervised and unsupervised

- classifiers for hyperspectral imagery. *IEEE Geoscience and Remote Sensing Letters*, 7(4):875–879, 2010. ISSN 1545598X. doi: 10.1109/LGRS.2010.2054063.
- [100] Ashwini Galande and Ratna Patil. The Art of Medical Image Fusion: A Survey. In *International Conference on Advances in Computing, Communications and Informatics (ICACCI)*, Mysore, India, 2013. IEEE. doi: 10.1109/ICACCI.2013.6637205.
- [101] Mostafa Abdel-Aleem, Claude C. Chibelushi, and Mansour Moniri. Multisensor data fusion for the simultaneous location and condition assessment of underground water pipelines. In *2011 International Conference on Networking, Sensing and Control, ICNSC 2011*, pages 416–421, Delft, The Netherlands, 2011. IEEE. ISBN 9781424495702. doi: 10.1109/ICNSC.2011.5874937.
- [102] David J. Daniels. Properties of Materials. In David J. Daniels, editor, *Ground Penetrating Radar*, chapter 4, pages 73–128. Institution of Electrical Engineers, London, UK, 2 edition, 2004. ISBN 0863413609.
- [103] Christopher D F Rogers. Support Smart and Liveable Cities. In *8th International Workshop on Advanced Ground Penetrating Radar (IWAGPR)*,, pages 1–4, Florence, Italy, 2015. IEEE. ISBN 9781479964956.
- [104] Nicole Metje, Bilal Ahmad, and Stephen Micheal Crossland. Causes, impacts and costs of strikes on buried utility assets. *Institute of Civil Engineers:Municipal Engineer*, 168(3):165–174, 2015. ISSN 0965-0903. doi: 10.1680/muen.14.00035.

- [105] J. P. Mooney, J. D. Ciampa, G. N. Young, A. R. Kressner, and J. Carbonara. GPR mapping to avoid utility conflicts prior to construction of the M-29 transmission line. In *2010 IEEE PES Transmission and Distribution Conference and Exposition: Smart Solutions for a Changing World*, pages 1–8, Louisiana, USA, 2010. IEEE. ISBN 9781424465477. doi: 10.1109/TDC.2010.5484564.
- [106] David Ayala-Cabrera, Manuel Herrera, Joaquín Izquierdo, Silvia J. Ocaña-Levario, and Rafael Pérez-García. GPR-based water leak models in water distribution systems. *Sensors (Switzerland)*, 13(12):15912–15936, 2013. ISSN 14248220. doi: 10.3390/s131215912.
- [107] S. Shihab and W. Al-Nuaimy. Radius estimation for cylindrical objects detected by ground penetrating radar. *Subsurface Sensing Technologies and Applications*, 6(2):151–166, 2005. ISSN 15660184. doi: 10.1007/s11220-005-0004-1.
- [108] Lihong Qiao, Yao Qin, Xiaozhen Ren, and Qifu Wang. Identification of Buried Objects in GPR Using Amplitude Modulated Signals Extracted from Multiresolution Monogenic Signal Analysis. *Sensors*, 15(12):30340–30350, 2015. ISSN 1424-8220. doi: 10.3390/s151229801.
- [109] Laurence Mertens, Raffaele Persico, Loredana Matera, and Sebastien Lambot. Automated Detection of Reflection Hyperbolas in Complex GPR Images With No A Priori Knowledge on the Medium. *IEEE Transactions on Geoscience and Remote Sensing*, 54(1):580–596, jan 2016. ISSN 0196-2892. doi: 10.1109/TGRS.2015.2462727.

- [110] Mark A Richards, James A. Scheer, and William A Holm. Matched Filter Imaging. In *Principles of Modern Radar: Volume i - Basic Principles*, chapter 21, pages 871– 873. Scitech Publishing Inc., NC, USA, 2010. ISBN 978-1-891121-52-4.
- [111] Eeva Huuskonen-Snicker, Valeri A. Mikhnev, and Martta Kaisa Olkkonen. Discrimination of buried objects in impulse GPR using phase retrieval technique. *IEEE Transactions on Geoscience and Remote Sensing*, 53(2):1001–1007, 2015. ISSN 01962892. doi: 10.1109/TGRS.2014.2331427.
- [112] Parneet Kaur, Kristin J. Dana, Francisco A. Romero, and Nenad Gucunski. Automated GPR Rebar Analysis for Robotic Bridge Deck Evaluation. *IEEE Transactions on Cybernetics*, 2015. ISSN 2168-2267. doi: 10.1109/TCYB.2015.2474747.
- [113] Ch Trela, Th Kind, M Schubert, M Gunther, Unter Den Eichen, and Christiane Trelabamde. Detection of Weak Scatterers in Reinforced Concrete Structures. In *15th International Conference on Ground Penetrating Radar (GPR)*, Brussels, Belgium, 2014. IEEE. ISBN 9781479967896.
- [114] Denise B. Pelowitz. *MCNPX User’s Manual: Version 2.7.0*. Los Alamos National Laboratory, New Mexico, USA, 2011.
- [115] Craig Warren, Antonios Giannopoulos, and Iraklis Giannakis. gprMax: Open source software to simulate electromagnetic wave propagation for Ground Pen-

- etrating Radar. *Computer Physics Communications*, 209:163–170, 2016. ISSN 00104655. doi: 10.1016/j.cpc.2016.08.020.
- [116] Peter G. Martin, James Moore, John S. Fardoulis, Oliver D. Payton, and Thomas B. Scott. Radiological assessment on interest areas on the sellafield nuclear site via unmanned aerial vehicle. *Remote Sensing*, 8(11):1–10, 2016. ISSN 20724292. doi: 10.3390/rs8110913.
- [117] International Atomic Energy Agency. Decommissioning of Facilities, 2014.
- [118] Jerry Towler, Bryan Krawiec, and Kevin Kochersberger. Terrain and Radiation Mapping in Post-Disaster Environments Using an Autonomous Helicopter. *Remote Sensing*, 4(7):1995–2015, 2012. ISSN 20724292. doi: 10.3390/rs4071995.
- [119] R. Lal, L.K. Fifield, S.G. Tims, and R.J. Wasson.  $^{239}\text{Pu}$  fallout across continental Australia: Implications on  $^{239}\text{Pu}$  use as a soil tracer. *Journal of Environmental Radioactivity*, 178-179:394–403, 2017. ISSN 0265931X. doi: 10.1016/j.jenvrad.2017.08.009.
- [120] B. Alan Shippen and M. J. Joyce. Extension of the linear depth attenuation method for the radioactivity depth analysis tool(RADPAT). *IEEE Transactions on Nuclear Science*, 58(3 PART 3):1145–1150, 2011. ISSN 00189499. doi: 10.1109/TNS.2011.2115253.
- [121] Jamie C. Adams, Matthew Mellor, and Malcolm J. Joyce. Depth determination of buried caesium-137 and cobalt-60 sources using scatter peak data.

- IEEE Transactions on Nuclear Science*, 57(5 PART 2):2752–2757, 2010. ISSN 00189499. doi: 10.1109/TNS.2009.2038480.
- [122] Jamie C. Adams, Matthew Mellor, and Malcolm J. Joyce. Determination of the depth of localized radioactive contamination by  $^{137}\text{Cs}$  and  $^{60}\text{Co}$  in sand with principal component analysis. *Environmental Science and Technology*, 45(19):8262–8267, 2011. ISSN 0013936X. doi: 10.1021/es201619r.
- [123] Jamie C Adams, Malcolm J Joyce, and Matthew Mellor. The advancement of a technique using principal component analysis for the non-intrusive depth profiling of radioactive contamination. *Nuclear Science, IEEE Transactions on*, 59(4):1448–1452, 2012.
- [124] Jamie C. Adams, Malcolm J. Joyce, and Matthew Mellor. Depth profiling  $^{137}\text{Cs}$  and  $^{60}\text{Co}$  non-intrusively for a suite of industrial shielding materials and at depths beyond 50mm. *Applied Radiation and Isotopes*, 70(7):1150–1153, 2012. ISSN 09698043. doi: 10.1016/j.apradiso.2011.11.033.
- [125] R.J. McConn, C. J Gesh, R.T Pagh, R. A Rucker, and R.G Williams. Compendium of Material Composition Data for Radiation Transport Modelling. Technical report, Pacific Northwest National Laboratory, Washington, US, 2011.
- [126] Eljen Technology. Neutron / Gamma Psd Liquid Scintillator Ej-301, Ej-309, 2016.

- [127] National Institute of Standards and Technology. X-Ray Mass Attenuation Coefficients, 2004.
- [128] R. T. Kouzes, J. H. Ely, B. D. Milbrath, J. E. Schweppe, E. R. Siciliano, and D. C. Stromswold. Spectroscopic and non-spectroscopic radiation portal applications to border security. *IEEE Nuclear Science Symposium Conference Record*, 1:321–325, 2005. ISSN 10957863. doi: 10.1109/NSSMIC.2005.1596262.
- [129] Ikechukwu K Ukaegbu and Kelum A A Gamage. Ground Penetrating Radar as a Contextual Sensor for Multi-Sensor Radiological Characterisation. *Sensors*, 17(4), 2017.
- [130] Ikechukwu Ukaegbu and Kelum Gamage. A Novel Method for Remote Depth Estimation of Buried Radioactive Contamination. *Sensors*, 18(2):1–13, 2018. ISSN 1424-8220. doi: 10.3390/s18020507.
- [131] Stefano del Sordo, Leonardo Abbene, Ezio Caroli, Anna Maria Mancini, Andrea Zappettini, and Pietro Ubertini. Progress in the development of CdTe and CdZnTe semiconductor radiation detectors for astrophysical and medical applications. *Sensors*, 9(5):3491–3526, 2009. ISSN 14248220. doi: 10.3390/s90503491.
- [132] David Goodman, Michael Streicher, Yuefeng Zhu, Steven Brown, and Zhong He. 1-D Fast Neutron Source Localization Using Digital Pixelated 3-D Position-Sensitive CdZnTe Detectors. *IEEE Transactions on Nuclear Science*, 64(9): 2531–2535, 2017. ISSN 00189499. doi: 10.1109/TNS.2017.2729942.

- [133] a. Georgiev and W. Gast. Digital pulse processing in high-resolution, high-throughput, gamma-ray spectroscopy. *IEEE Transactions on Nuclear Science*, 40(4):770–779, 1993. ISSN 1558-1578. doi: 10.1109/23.256659.
- [134] M. Kavatsyuk, D. Bremer, V. Dormenev, P. Drexler, T. Eissner, W. Erni, E. Guliyev, T. Hennino, B. Krusche, B. Lewandowski, H. Löhner, M. Moritz, R. W. Novotny, K. Peters, J. Pouthas, P. Rosier, M. Steinacher, G. Tambave, and A. Wilms. Performance of the prototype of the Electromagnetic Calorimeter for PANDA. *Nuclear Instruments and Methods in Physics Research, Section A: Accelerators, Spectrometers, Detectors and Associated Equipment*, 648(1):77–91, 2011. ISSN 01689002. doi: 10.1016/j.nima.2011.06.044.
- [135] P. Mortreau and R. Berndt. Characterisation of cadmium zinc telluride detector spectra – application to the analysis of spent fuel spectra. *Nuclear Instruments and Methods in Physics Research Section A: Accelerators, Spectrometers, Detectors and Associated Equipment*, 458(1-2):183–188, feb 2001. ISSN 01689002. doi: 10.1016/S0168-9002(00)00862-7.
- [136] Adam Varley, Andrew Tyler, Mark Dowdall, Yuri Bondar, and Viachaslau Zabrotski. An in situ method for the high resolution mapping of  $^{137}\text{Cs}$  and estimation of vertical depth penetration in a highly contaminated environment. *Science of the Total Environment*, 605-606:957–966, 2017. ISSN 18791026. doi: 10.1016/j.scitotenv.2017.06.067.
- [137] Kh Haddad, M. S. Al-Masri, and A. W. Doubal. Determination of  $^{226}\text{Ra}$

- contamination depth in soil using the multiple photopeaks method. *Journal of Environmental Radioactivity*, 128:33–37, 2014. ISSN 18791700. doi: 10.1016/j.jenvrad.2013.10.025.
- [138] Y. Iwamoto, J. Kataoka, A. Kishimoto, T. Nishiyama, T. Taya, H. Okochi, H. Ogata, and S. Yamamoto. Novel methods for estimating 3D distributions of radioactive isotopes in materials. *Nuclear Instruments and Methods in Physics Research, Section A: Accelerators, Spectrometers, Detectors and Associated Equipment*, 831:295–300, 2016. ISSN 01689002. doi: 10.1016/j.nima.2016.03.098.
- [139] Adam Varley, Andrew Tyler, Yuri Bondar, Ali Hosseini, Viachaslau Zabrotski, and Mark Dowdall. Reconstructing the deposition environment and long-term fate of Chernobyl<sup>137</sup>Cs at the floodplain scale through mobile gamma spectrometry. *Environmental Pollution*, 240:191–199, 2018. ISSN 18736424. doi: 10.1016/j.envpol.2018.04.112.
- [140] Steven Clifford Dewey, Zachary David Whetstone, and Kimberlee Jane Kearfott. A method for determining the analytical form of a radionuclide depth distribution using multiple gamma spectrometry measurements. *Journal of Environmental Radioactivity*, 102(6):581–588, 2011. ISSN 0265931X. doi: 10.1016/j.jenvrad.2011.03.006.
- [141] Z. D. Whetstone, S. C. Dewey, and K. J. Kearfott. Simulation of a method for determining one-dimensional<sup>137</sup>Cs distribution using multiple gamma spec-

- troscopic measurements with an adjustable cylindrical collimator and center shield. *Applied Radiation and Isotopes*, 69(5):790–802, 2011. ISSN 09698043. doi: 10.1016/j.apradiso.2011.01.019.
- [142] Adam Varley, Andrew Tyler, Leslie Smith, Paul Dale, and Mike Davies. Remediating radium contaminated legacy sites: Advances made through machine learning in routine monitoring of "hot" particles. *Science of the Total Environment*, 521-522:270–279, 2015. ISSN 18791026. doi: 10.1016/j.scitotenv.2015.03.131.
- [143] Adam Varley, Andrew Tyler, Leslie Smith, Paul Dale, and Mike Davies. Mapping the spatial distribution and activity of  $^{226}\text{Ra}$  at legacy sites through Machine Learning interpretation of gamma-ray spectrometry data. *Science of the Total Environment*, 545-546:654–661, 2016. ISSN 18791026. doi: 10.1016/j.scitotenv.2015.10.112.
- [144] Ahmed Abed Gatea Al-Shammary, Abbas Z. Kouzani, Akif Kaynak, Sui Yang Khoo, Michael Norton, and Will Gates. Soil Bulk Density Estimation Methods: A Review. *Pedosphere*, 28(4):581–596, 2018. ISSN 10020160. doi: 10.1016/S1002-0160(18)60034-7.
- [145] Anh Phuong Tran, Frederic Andre, and Sebastien Lambot. Validation of near-field ground-penetrating radar modeling using full-wave inversion for soil moisture estimation. *IEEE Transactions on Geoscience and Remote Sensing*, 52(9): 5483–5497, 2014. ISSN 01962892. doi: 10.1109/TGRS.2013.2289952.
- [146] Jonathan Algeo, Remke L. Van Dam, and Lee Slater. Early-Time GPR: A

- Method to Monitor Spatial Variations in Soil Water Content during Irrigation in Clay Soils. *Vadose Zone Journal*, 15(11):0, 2016. ISSN 1539-1663. doi: 10.2136/vzj2016.03.0026.
- [147] Christian N. Koyama, Hai Liu, Kazunori Takahashi, Masanobu Shimada, Manabu Watanabe, Tseedulam Khuut, and Motoyuki Sato. In-situ measurement of soil permittivity at various depths for the calibration and validation of low-frequency SAR soil moisture models by using GPR. *Remote Sensing*, 9(6):1–14, 2017. ISSN 20724292. doi: 10.3390/rs9060580.
- [148] Omer Shamir, Naftaly Goldshleger, Uri Basson, and Moshe Reshef. Laboratory Measurements of Subsurface Spatial Moisture Content by Ground-Penetrating Radar (GPR) Diffraction and Reflection Imaging of Agricultural Soils. *Remote Sensing*, 10(10):1667, 2018. ISSN 2072-4292. doi: 10.3390/rs10101667.
- [149] I. L. Al-Qadi and S. Lahouar. Measuring layer thicknesses with GPR - Theory to practice. *Construction and Building Materials*, 19(10):763–772, 2005. ISSN 09500618. doi: 10.1016/j.conbuildmat.2005.06.005.
- [150] Andrea Benedetto, Fabio Tosti, Bianca Ortuani, Mauro Giudici, and Mauro Mele. Soil moisture mapping using GPR for pavement applications. In *7th International Workshop on Advanced Ground Penetrating Radar*, pages 1–5, Nantes, France, jul 2013. IEEE. ISBN 978-1-4799-0940-7. doi: 10.1109/IWAGPR.2013.6601550.
- [151] Andreas Loizos and Christina Plati. Accuracy of pavement thicknesses estima-

- tion using different ground penetrating radar analysis approaches. *NDT and E International*, 40(2):147–157, 2007. ISSN 09638695. doi: 10.1016/j.ndteint.2006.09.001.
- [152] Zhen Leng, Imad L. Al-Qadi, and Samer Lahouar. Development and validation for in situ asphalt mixture density prediction models. *NDT and E International*, 44(4):369–375, 2011. ISSN 09638695. doi: 10.1016/j.ndteint.2011.03.002.
- [153] Pengcheng Shangguan, Imad L. Al-Qadi, and Samer Lahouar. Pattern recognition algorithms for density estimation of asphalt pavement during compaction: A simulation study. *Journal of Applied Geophysics*, 107:8–15, 2014. ISSN 09269851. doi: 10.1016/j.jappgeo.2014.05.001.
- [154] Alessandro Brovelli and Giorgio Cassiani. Effective permittivity of porous media: A critical analysis of the complex refractive index model. *Geophysical Prospecting*, 56(5):715–727, 2008. ISSN 13652478. doi: 10.1111/j.1365-2478.2008.00724.x.
- [155] Ari H. Sihvola. Self-Consistency Aspects of Dielectric Mixing Theories. *IEEE Transactions on Geoscience and Remote Sensing*, 27(4):403–415, 1989. ISSN 15580644. doi: 10.1109/36.29560.
- [156] J. Robert Birchak, C. Gerald Gardner, Jackie E. Hipp, and Joe M. Victor. High Dielectric Constant Microwave Probes for Sensing Soil Moisture. *Proceedings of the IEEE*, 62(1):93–98, 1974. ISSN 15582256. doi: 10.1109/PROC.1974.9388.
- [157] Kurt Roth, Rainer Schulin, Hannes F L Hler, and Werner Attinger. Calibra-

- tion of Time Domain Reflectometry for Water Content Measurement. *Water Resources*, 26(10):2267–2273, 1990.
- [158] C. M.K. Gardner, T. J. Dean, and J. D. Cooper. Soil water content measurement with a high-frequency capacitance sensor. *Journal of Agricultural and Engineering Research*, 71(4):395–403, 1998. ISSN 00218634. doi: 10.1006/jaer.1998.0338.
- [159] Myron C. Dobson, Fawwaz T. Ulaby, Martti T. Hallikainen, and Mohamed A. El-Rayes. Microwave Dielectric Behavior of Wet Soil-Part II: Dielectric Mixing Models. *IEEE Transactions on Geoscience and Remote Sensing*, GE-23(1):35–46, 1985. ISSN 15580644. doi: 10.1109/TGRS.1985.289498.
- [160] Neil R. Peplinski, Fawwaz T. Ulaby, and Myron C. Dobson. Dielectric Properties of Soils in the 0.3–1.3-GHz Range. *IEEE Transactions on Geoscience and Remote Sensing*, 33(3):803–807, 1995. ISSN 15580644. doi: 10.1109/36.387598.
- [161] Lord Rayleigh. LVI. On the influence of obstacles arranged in rectangular order upon the properties of a medium. *The London, Edinburgh, and Dublin Philosophical Magazine and Journal of Science*, 34(211):481–502, dec 1892. ISSN 1941-5982. doi: 10.1080/14786449208620364.
- [162] C. J. F. Bottcher and P. Borderwijk. *Theory of Electric Polarization I1*. Elsevier B.V., Amsterdam, 1978.
- [163] Fabio Tosti, Luca Bianchini Ciampoli, Alessandro Calvi, Amir M. Alani, and Andrea Benedetto. An investigation into the railway ballast dielectric properties using different GPR antennas and frequency systems. *NDT and E International*,

- 93(October 2017):131–140, 2018. ISSN 09638695. doi: 10.1016/j.ndteint.2017.10.003.
- [164] P. Schjønning, R.A. McBride, T. Keller, and P.B. Obour. Predicting soil particle density from clay and soil organic matter contents. *Geoderma*, 286:83–87, 2017. ISSN 00167061. doi: 10.1016/j.geoderma.2016.10.020.
- [165] Ikechukwu Ukaegbu and Kelum Gamage. A Model for Remote Depth Estimation of Buried Radioactive Wastes Using CdZnTe Detector. *Sensors*, 18(5):1612, may 2018. ISSN 1424-8220. doi: 10.3390/s18051612.
- [166] Christian Mätzler. Microwave Permittivity of Dry Sand. *IEEE Transactions on Geoscience and Remote Sensing*, 36(1):317–319, 1998. ISSN 01962892. doi: 10.1109/36.655342.
- [167] W Burkart A Bleise, PR Danesi. Properties, use and health effects of depleted uranium. *Journal of environmental radioactivity*, 64:93–112, 2003.
- [168] Roland R. Benke and Kimberlee J. Kearfott. An improved in situ method for determining depth distributions of gamma-ray emitting radionuclides. *Nuclear Instruments and Methods in Physics Research, Section A: Accelerators, Spectrometers, Detectors and Associated Equipment*, 463(1-2):393–412, 2001. ISSN 01689002. doi: 10.1016/S0168-9002(01)00449-1.
- [169] S. C. Dewey, Z. D. Whetstone, and K. J. Kearfott. A numerical method for the calibration of in situ gamma ray spectroscopy systems. *Health Physics*, 98(5):657–671, 2010. ISSN 00179078. doi: 10.1097/HP.0b013e3181ca8ba8.

- [170] Ikechukwu K. Ukaegbu, Kelum A.A. Gamage, and Michael D. Aspinall. Noninvasive depth estimation of buried radioactive wastes using ground penetrating radar and a gamma ray detector. *Remote Sensing*, 11(2):7–14, 2019. ISSN 20724292. doi: 10.3390/rs11020141.
- [171] L. Klein and C. Swift. An improved model for the dielectric constant of sea water at microwave frequencies. *IEEE Transactions on Antennas and Propagation*, 25(1):104–111, jan 1977. ISSN 0096-1973. doi: 10.1109/TAP.1977.1141539.
- [172] A. Stogryn. The Brightness Temperature of a Vertically Structured Medium. *Radio Science*, 5(12):1397–1406, dec 1970. ISSN 00486604. doi: 10.1029/RS005i012p01397.
- [173] Craig Warren and Antonios Giannopoulos. Creating finite-difference time-domain models of commercial ground-penetrating radar antennas using Taguchi’s optimization method. *Geophysics*, 76(2):G37–G47, 2011. ISSN 0016-8033. doi: 10.1190/1.3548506.
- [174] Corey Keith, Hugh Selby, Amy Lee, Morgan White, Bryan Bandong, Kevin Roberts, and Jennifer Church. Activation product interpretation of structural material for fast critical assemblies. *Annals of Nuclear Energy*, 119:98–105, 2018. ISSN 18732100. doi: 10.1016/j.anucene.2018.04.028.
- [175] K. A. A. Gamage, M. J. Joyce, and G. C. Taylor. A comparison of collimator geometries for imaging mixed radiation fields with fast liquid organic scintillators. In *2011 2nd International Conference on Advancements in Nuclear Instrumen-*

- tation, Measurement Methods and their Applications*, pages 1–5, June 2011. doi: 10.1109/ANIMMA.2011.6172943.
- [176] M A Hilhorst. A Pore Water Conductivity Sensor. *Soil Science Society of America Journal*, 64:1922–1925, 2000. doi: 10.2136/sssaj2000.6461922x.
- [177] Andrea Ciampalini, Frédéric André, Francesca Garfagnoli, Gilles Grandjean, Sébastien Lambot, Leandro Chiarantini, and Sandro Moretti. Improved estimation of soil clay content by the fusion of remote hyperspectral and proximal geophysical sensing. *Journal of Applied Geophysics*, 116:135–145, 2015. ISSN 09269851. doi: 10.1016/j.jappgeo.2015.03.009.
- [178] Esther Babcock and John H Bradford. Reflection waveform inversion of ground-penetrating radar data for characterizing thin and ultrathin layers of nonaqueous phase liquid contaminants in stratified media. *Geophysics*, 80(2), 2015. doi: Doi10.1190/Geo2014-0037.1.